Liquid Metal Flows Driven by Gas Bubbles in a Static Magnetic Field

Der Fakultät Maschinenwesen
der
Technischen Universität Dresden

zur
Erlangung des Grades
Doktoringenieur (Dr.-Ing.)
vorgelegte Dissertation

M. Eng. Chaojie Zhang
geb. am 14. Juli 1976

Tag der Einreichung: 09. April 2009

Preface

This dissertation investigates liquid metal flows driven by rising gas bubbles in a static magnetic field, the direction of which is either vertical or horizontal, respectively. Using ultrasound Doppler velocimetry (UDV), we measure the velocities of the gas and liquid phases in model experiments based on the melt GaInSn. The results disclose different magnetic damping influences on the flow depending on the direction of the magnetic field.

Chapter 1 consists of three parts: a short introduction to the research background; a brief review on the fundamentals of magnetohydrodynamics (MHD) that are relevant for the current work; as well as some descriptions of the model experiments using low-temperature melt in the laboratory.

Chapter 2 reviews ultrasound Doppler methods for the measurements of fluid flow. We focus on an ultrasound device DOP2000, whose capability is tested especially for the measurements of bubble-driven flows.

Chapter 3 is concerned with the flow of a single bubble rising in a bulk of stagnant melt, which is exposed to a vertical or a horizontal field. We measure the velocity of the bubble as well as the bubble-induced liquid motion, and compare the influence of the magnetic damping as the field direction is changed.

Chapter 4 is focused on liquid metal flows driven by a bubble plume inside an insulating vessel. We obtain velocity fields of the liquid phase, as well as the distributions of void fraction, of the flow in a vertical and a horizontal magnetic field, respectively. The results are compared and discussed.

Chapter 5 summarizes the current work and presents the main conclusions based on the current results. The relevance of the current research work to the real industrial applications is discussed.

Contents

Chapter 1

Introduction

This chapter presents a brief review of the research background, some related MHD fundamentals concerning a static magnetic field, and the approaches to conduct model experiments in laboratory using low-temperature melt. Specifically, we focus on the influence of a static magnetic field on several two-phase flows encountered in metallurgical engineering. It is important to comprehend the flow phenomena and their physical mechanisms before we can control such flows reliably and effectively in real applications. Next, we briefly look through some fundamentals of magnetohydrodynamics, which will serve as the basis for the understanding in the present work. Finally, the necessities and advantages of laboratory model experiments are discussed. The use of low-temperature melt simplifies experiments greatly and makes it much easier to observe the influence of a magnetic field on the flow.

1.1 Research background

Two-phase flows consisting of gas and liquid metals are usually encountered in metallurgical engineering. In a steel-making process, for instance, two-phase flows are indispensable in several stages, see for example Thomas (2003a,b) and the references therein for a comprehensive review.

As a refining technique, inert gas bubbles are usually injected into a bulk of molten melt inside a ladle. The rising bubbles drive the surrounding fluid into motion and so enhance the mixing inside the melt. As a result, the melt can be refined because of a more homogeneous distribution of the physical and chemical properties. The details of the dispersed bubble motion, the distribution of the void fraction, as well as the velocity field of the liquid phase are important information for the optimization of the refining process.

Examples of two-phase flows can be found in other stages of the steel-making process too. In a continuous casting process, for instance, fresh melt is introduced into a bottomless mould through a submerged entry nozzle (SEN). Usually, inert gas is added to the melt in order to avoid the clogging of the nozzle. As a result, a two-phase jet flow is formed inside the mould. The flow pattern is important for the casting process, because the strong shear stress

in the flow can easily destroy the solidified strand close to the mould wall. This becomes especially dangerous at high casting speeds. Therefore, a reliable flow control is needed in order to avoid such phenomena.

Electromagnetic fields are attractive tools to control liquid metal flows at high temperatures, because the induced Lorentz force acts on the fluid in a contactless way. Various fields generated by alternating current (AC) or direct current (DC) can be applied; see reviews given by Sneyd (1993), Moreau (1990), Davidson (2001) and Toh et al. (2006). It is well-known that a rotating magnetic field (RMF) or a traveling magnetic field (TMF) can be used as an electromagnetic stirrer to enhance the mixing in the melts. In comparison, a DC magnetic field often works as an "electromagnetic brake", which usually suppresses fluid motion. Many investigations are devoted to the application of an electromagnetic field in a continuous casting process, see Taniguchi (2006). Several numerical simulations were conducted to predict the flow in the mold region under the influence of external magnetic fields; see for example Okazawa et al. (2001), Toh et al. (2001), Takatani (2003), Kubo et al. (2004), Lavers et al. (2006) and Cukierski & Thomas (2008). Owing to the complexity of the problem, careful validations with experimental results are necessary.

The influence of a static magnetic field on bubble-driven flows is rarely investigated in literature. During the past, the investigations on MHD two-phase flows are mainly concerned with the applications in nuclear engineering, such as bubbly pipe flows in a closed loop driven by external pumps. In such flows, gas bubbles are added to the liquid metal for various purposes: to modify the pressure drop, the turbulent fluctuations, the properties of heat transfer and so on. External magnetic fields can be used to control the motion of the both phases; see for example Michiyoshi et al. (1977), Saito et al. (1978a,b), Lykoudis (1984), Serizawa et al. (1990) and Eckert et al. (2000a,b). Some of the earlier investigations are relevant to the current work, despite the different backgrounds. However, it can be noticed that the community needs systematic experimental investigations concerning the topic.

1.2 Some fundamentals of magnetohydrodynamics

This section gives a brief review of some fundamentals of magnetohydrodynamics, which is related to a static magnetic field and the flows in model experiments in laboratory. More comprehensive and detailed descriptions can be found, for example, in Moreau (1990) and Davidson (2001).

For most of the industrial and laboratory cases, the hydrodynamic Reynolds number Re

is large and the magnetic Reynolds number R_m is small:

$$Re = ul/\nu \gg 1 \tag{1.1}$$

$$R_m = \mu\sigma_e ul \ll 1 \tag{1.2}$$

where u and l represent the characteristic velocity and length scale of the flow, and ν, μ, σ_e are the material kinematic viscosity, magnetic permeability and electrical conductivity respectively. For instance, liquid steel has the following physical properties: $\mu = 1.25 \times 10^{-6}$ kg/(m·s), $\sigma_e = 0.7 \times 10^6$ $(\Omega\cdot\text{m})^{-1}$, $\nu = 10^{-6}$ m^2/s; if we take $u = 0.1$ m/s and $l = 0.1$ m, there are $Re \sim 10^4$ and $R_m \sim 0.01$. The small R_m indicates that the perturbation to the imposed magnetic field due to the induced magnetic field is negligible. Therefore, the problem is simplified by the fact that only the influence of the magnetic field on the flow needs to be considered.

For liquid motion with velocity $\mathbf{u}$ in a static magnetic field $\mathbf{B}$, the induced electric current $\mathbf{J}$ is governed by the Ohm's law

$$\mathbf{J} = \sigma_e(\mathbf{E} + \mathbf{u} \times \mathbf{B}) \tag{1.3}$$

Under the small R_m condition, $\mathbf{E}$ is irrotational and can be written as an electrostatic potential in the form of $-\nabla\phi$.

The induced electric current satisfies the electric charge conservation rule

$$\nabla \cdot \mathbf{J} = 0 \tag{1.4}$$

Therefore, the scalar potential ϕ is defined by the following Poisson equation

$$\nabla^2\phi = \nabla \cdot (\mathbf{u} \times \mathbf{B}) \tag{1.5}$$

The induced Lorentz force on the fluid is

$$\mathbf{F} = \mathbf{J} \times \mathbf{B} \tag{1.6}$$

For incompressible flows such as liquid metals, the mass-conservation equation takes a simple form

$$\nabla \cdot \mathbf{u} = 0 \tag{1.7}$$

The electromagnetic force in equation (1.6) enters the Navier-Stokes equation as an additional body force

$$\frac{\partial \mathbf{u}}{\partial t} + (\mathbf{u} \cdot \nabla)\mathbf{u} = -\frac{1}{\rho}\nabla p + \nu\nabla^2\mathbf{u} + \frac{1}{\rho}\mathbf{F} \tag{1.8}$$

which governs the fluid motion together with corresponding boundary conditions.

In addition to Re and R_m, two more dimensionless parameters are relevant; namely, the Hartmann number Ha and the interaction number N

$$Ha = Bl(\sigma_e/\rho\nu)^{1/2} \tag{1.9}$$

$$N = \sigma_e B^2 l/\rho u \tag{1.10}$$

where B is the magnetic induction of the field under consideration. Ha indicates the ratio of the Lorentz force to viscous shear forces, and N indicates the ratio of Lorentz force to inertia force. Additionally, there is the following relationship among the Hartmann number, the interaction number and the Reynolds number

$$Ha = (NRe)^{1/2} \tag{1.11}$$

The flow in a static magnetic field has been investigated extensively in the literature, see for example Shercliff (1965), Robbert (1967), Sommeria & Moreau (1982), Moreau (1990), Davidson (1995, 2001), Müller & Bühler (2001) and Knaepen & Moreau (2008). Here, we show only several conclusions that are relevant for the discussions concerning the current work.

Consider a flow with velocity $\mathbf{u}$ in a homogeneous DC magnetic field $\mathbf{B}$ that is in z direction. Taking the curl of equation (1.3), the induced current due to the fluid motion is governed by

$$\nabla \times \mathbf{J} = \sigma_e(\mathbf{B}\cdot\nabla)\mathbf{u} = \sigma_e B\frac{\partial \mathbf{u}}{\partial z} \tag{1.12}$$

because the terms containing $\nabla\cdot\mathbf{u}$, $\nabla\cdot\mathbf{B}$ and $(\mathbf{u}\cdot\nabla)\mathbf{B}$ all vanish. The above equation shows that $\mathbf{J}$ reduces to zero when the flow is uniform along the field lines; in other words, the magnetic field cannot influence the flow when the velocity field $\mathbf{u}$ becomes two-dimensional and does not depend on z. It is worth to point out that specific boundary conditions are needed to make this conclusion valid; namely, the current is supposed to close itself only inside the liquid. This is the case, for instance, when the fluid domain is infinite or bounded by insulating walls.

Sommeria & Moreau (1982) proposed an interpretation concerning the effect of the Lorentz force, which can be expressed as (more details can be found in appendices)

$$\frac{1}{\rho}\mathbf{F} = -\frac{\sigma_e B^2}{\rho}\triangle^{-1}\frac{\partial^2 \mathbf{u}}{\partial z^2} \tag{1.13}$$

where $\triangle^{-1}$ symbolically denotes the inverse of the Laplacian operator. For flow structures that are sufficiently elongated in the direction of $\mathbf{B}$, one can assume $\partial/\partial z \ll \partial/\partial x, \partial/\partial y$. Therefore, equation (1.13) can be rewritten as

$$\frac{1}{\rho}\mathbf{F} = -\frac{\sigma_e B^2}{\rho}\triangle_\perp^{-1}\frac{\partial^2 \mathbf{u}}{\partial z^2} \approx -\frac{\sigma_e B^2 l_\perp^2}{\rho}\frac{\partial^2 \mathbf{u}}{\partial z^2} \tag{1.14}$$

where the subscript $\perp$ denotes the direction perpendicular to $\mathbf{B}$. The above equation indicates that, in equation (1.8), the Lorentz force appears as a diffusion term which tends to uniform the flow in the direction of $\mathbf{B}$.

Davidson (1995, 2001) provided another explanation based on the consideration of momentum conservation. He pointed out that, on one hand, the Lorentz force changes neither the net linear momentum nor the component of angular momentum parallel to $\mathbf{B}$ in the fluid, as evidenced in the following way

$$\int_V \mathbf{F}\, dV = -\mathbf{B} \times \int_V \mathbf{J}\, dV = 0 \tag{1.15}$$

$$\int_V \mathbf{B} \cdot (\mathbf{x} \times \mathbf{F})\, dV = -\frac{B^2}{2\rho} \int_V \nabla \cdot [\mathbf{x}_\perp^2 \cdot \mathbf{J}]\, dV = 0 \tag{1.16}$$

As the electric current closes itself inside the liquid, equation (1.16) ensures that at least one component of the angular momentum of the flow cannot be destroyed by the Lorentz force; namely, the flow cannot be completely annihilated by the Lorentz force alone (It is worth to emphasize again that specific boundary conditions are needed for the conclusion. The flow domain should be infinite or bounded by insulating walls, as mentioned earlier. There should exist no external path, such as electric-conducting walls, through which the electric current can close itself). On the other hand, the Lorentz force indeed decreases the kinetic energy in the flow, as shown below

$$\frac{1}{\rho} \int_V \mathbf{F} \cdot \mathbf{u}\, dV = -(\rho\sigma_e)^{-1} \int_V \mathbf{J}^2\, dV \tag{1.17}$$

To avoid a complete annihilation of the flow, the Lorentz force must change the flow in such a way that the Joule dissipation should decrease faster than the decrease of the kinetic energy. The key point lies in equation (1.12), which shows that the induced current $\mathbf{J}$, hence the Joule dissipation, can be reduced to zero if the flow becomes uniform along the field lines. In other words, under the influence of the Lorentz force, the flow tends to become two-dimensional. The process can be achieved by spreading the flow momentum along the field lines, which decreases the velocity gradients in the direction of $\mathbf{B}$.

Davidson (2001) also discussed the influence of a static magnetic field on vortices. Consider a vortex with its axis parallel to the field lines in an infinite domain, the induced current $\mathbf{J}$ in the flow can be represented by equation (1.12). Namely, the damping effect depends on the velocity gradient projected on the field lines. The magnetic field cannot influence the velocity of the flow if the vortex is two-dimensional and uniform along the field lines. In comparison, the influence of the magnetic field on a vortex with its axis perpendicular to the field lines can be explained in the following way. We write equation (1.6) as

$$\frac{1}{\rho}\mathbf{F} = -\frac{\sigma_e}{\rho}(\nabla\phi \times \mathbf{B}) + \frac{\sigma_e}{\rho}(\mathbf{B} \cdot \mathbf{u})\mathbf{B} - \frac{\sigma_e}{\rho}(\mathbf{B} \cdot \mathbf{B})\mathbf{u} \tag{1.18}$$

The first term on the right hand side of equation (1.18) contains $\nabla\phi$. From equation (1.5), ϕ can be expressed as

$$\phi = \nabla^{-2}(\mathbf{B} \cdot \omega) \tag{1.19}$$

where ω is the vorticity defined as $\omega = \nabla \times \mathbf{u}$. For a two-dimensional vortex with its axis perpendicular to the field lines, the first term and the second term in equation (1.18) both vanish. Therefore, equation (1.18) simplifies to

$$\frac{1}{\rho}\mathbf{F} = -\frac{\sigma_e B^2}{\rho}\mathbf{u}_\perp \tag{1.20}$$

which shows that the electromagnetic force simply retards the fluid motion in the perpendicular plane.

1.3 Model experiments using low-temperature melts

Liquid metal flows are usually hard to be measured in real industrial processes because of their high temperatures. In contrast, it is easier to measure the motion of low-temperature melts in a model experiment in laboratory. Such an experiment can be conducted on a smaller scale and at room temperature, which can greatly simplify the investigation. The results can improve our understanding concerning the flow phenomena and serve as references for the validation of numerical simulations, see for example a review by Mazumdar & Evans (2004).

In the present work, we use the eutectic alloy GaInSn. The melting point of the alloy is low (around 5 °C), therefore, it is in liquid state at room temperature. The physical properties of the melt are: surface tension $\sigma = 3.2 \times 10^6$ S/m, density $\rho = 6.36 \times 10^3$ kg/m^3, kinematic viscosity $\nu = 3.4 \times 10^{-7}$ m^2/s and electric conductivity $\sigma_e = 3.2 \times 10^6$ $(\Omega\text{m})^{-1}$. Chemically, it is less aggressive and can be stored conveniently in the containers of plexiglass or plastic materials.

Owing to the opaqueness, optical methods such as Laser Doppler Anemometry (LDA) and Particle Image Velocimetry (PIV) cannot be directly used here. Several intrusive methods, such as hot film anemometry and potential probes, usually encounter several difficulties. Recently, ultrasound Doppler method has demonstrated its capacity in the measurements of liquid metal flows, see for example a recent review by Eckert et al. (2007). Such a method relies on ultrasound signals and does not require the transparency of the liquid. The ultrasound sensor can be arranged outside of a vessel and avoid additional disturbances to the flow. Currently, there are commercial ultrasound devices which deliver velocity profiles along the ultrasound beam in real time. The measuring volumes can be considered as cylindrical slices which distribute coaxially along the ultrasound beam. The spatial resolution can be

a few millimeters in the lateral direction and around half millimeter in the longitudinal direction. The temporal resolution, namely the scan rate of the consecutive profiles, can reach several tens of Hertz (Hz).

Many model experiments were carried out using ultrasound Doppler method recently. Commercial ultrasound sensors can be readily used when the temperature of the melt is below 150 °C approximately. For example, flows of GaInSn driven by rotating magnetic field (RMF), traveling magnetic field (TMF) or combined RMF and TMF were investigated in, for example, Cramer et al. (2004), Lantzsch et al. (2007), Cramer et al. (2007) and Grants et al. (2008). The influence of a time-modulated RMF on the solidification process can be found in Eckert et al. (2007) and Willers et al. (2008). For two-phase flows, the ultrasound Doppler method is able to deliver the velocities of the liquid phase and the gas phase simultaneously. More discussions concerning the application of the ultrasound technique in two-phase flows will be presented in the next chapter.

In summary, laboratory model experiments of low-temperature melts can improve our understandings concerning the flow phenomena encountered in metallurgical engineering, especially concerning the influence of an external magnetic field on the flow. This approach simplifies the experiments and improves working conditions. A significant advantage is that we can apply readily the ultrasound Doppler method, which enables us to "look" inside a bulk of opaque liquid. In the next chapter, the measuring technique based on the ultrasound Doppler effect will be explained in more details, including discussions concerning the application in two-phase flow measurements.

Chapter 2

Velocity measuring techniques for liquid metal flows

This chapter describes velocity measuring techniques for flows of liquid metals. At the beginning, we briefly review several well-established measuring techniques mentioned in the literature, including both invasive and non-invasive methods. Then, we focus on the ultrasound Doppler method. It is known that two types of ultrasound Doppler velocimetries (UDV), based on continuous wave or pulse wave ultrasound, are available for velocity measurements. In comparison to the method based on continuous waves, the use of pulse waves can be considered as an extended version with several advantages. In the current work, a commercial device based on pulse waves, DOP2000, is chosen for velocity measurements. Earlier research activities are reviewed concerning the UDV applications in transparent liquids as well as in liquid metals. After that, we test the capability of DOP2000 for the measurement of two-phase flows. Several measurements are conducted step by step: the terminal velocities of a sphere settling down or a bubble rising up in a stagnant liquid, as well as the velocities of both phases in a flow driven by a bubble chain. The measured values are compared with literature data or those acquired by LDA in parallel. For bubble-driven flows, we use a threshold method to extract the liquid velocity from the mixed velocity signals of both phases.

2.1 A literature review

Analysis and control of fluid flows often require measurements of velocity fields. This need is not diminished by the advances in numerical simulations; rather, it is enhanced in many ways, see Goldstein (1996). A variety of well-developed techniques such as Hot-Wire Anemometry (HWA), Laser Doppler Velocimetry (LDV) and Particle Image Velocimetry (PIV) are available for conventional liquids such as water or gas. Detailed discussions of them and other methods can be found, for instance, in Bradshaw (1971), Durst et al. (1981), Gad-El-Hak

(1989), Bruun (1995), Albrecht (2003), Breuer (2005), Tavoularis (2005), Raffel (2007) and Tropea et al. (2007).

In contrast, the development is slow concerning the measuring techniques for liquid metal flows. Besides the opaqueness, molten melts and semiconductors usually possess high temperatures and chemical aggressiveness. As a result, some of the conventional measuring techniques cannot be directly used here or they have to face a harsh working environment. In the following parts, we will focus on research activities concerning the velocity measurements in liquid metals. An earlier comprehensive description of the measuring techniques are given by Shercliff (1962), and a recent review on the same topic can be found in Eckert et al. (2007). In the following discussions we classify the various techniques into invasive and non-invasive ones.

2.1.1 Invasive methods

An invasive method means the insertion of a sensing unit into the medium under consideration. Based on the underlying physical mechanisms, such invasive probes can be classified, for instance, into force reaction, thermal and conductive sensors. In the following sections, we will briefly introduce these measuring techniques with application examples.

Force reaction probes

Such a probe detects the force exerted on the sensor due to the flowing medium. Szekely et al. (1977) constructed a force reaction probe to measure melt velocities driven by a traveling magnetic field in a container. Their probe consisted of a 19 mm-diameter disc of stainless steel and a hollow rod with a loaded spring in it. The disc is fastened to one end of the rod and immersed into the liquid to probe the fluid motion. The other end of the rod is connected to a linear voltage differential transformer. Owing to the spring, the electrical output of the transformer corresponds to the pressure force exerting on the disc. The detected pressure can be converted to the melt velocity through calibrations. The measured flow velocities in their experiments were lying in the range from 8 cm/s to 50 cm/s. Concerning the measurements of velocity fluctuations, they pointed out that the inertia of the measuring system does not provide a great deal of insight into the structure of the turbulent flow.

For flows with very low velocities, Griffiths & Nicol (1965) suggested a fibre flow-meter, the measuring principle of which is to detect the deflection of a very thin quartz fibre immersed in the flowing fluid. This technique was later extended by Zhilin et al. (1989) and Eckert et al. (2000c) to the measurements of liquid metal flows at velocities of several tens of

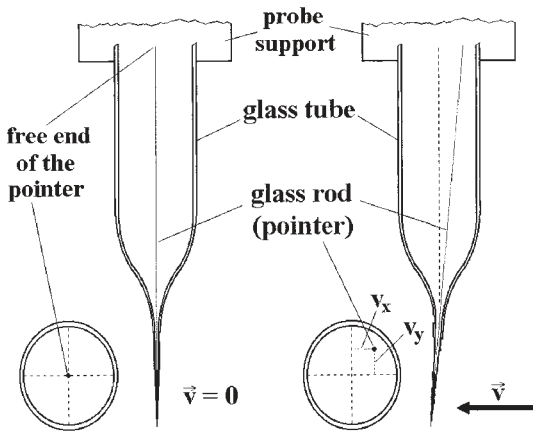

Figure 2.1: Working principle of the fiber sensor designed by Eckert et al. (2000c).

cm/s, see an example showing in Figure 2.1. These authors obtained local velocities of two components with a resolution around 1cm/s. Such fibre flow-meters are free from electronic noises and therefore can be used to measure, for instance, electro-vortical flows. Whereas they are also limited by several disadvantages: the sensors are fragile and hard to be fabricated, and additional calibrations are needed for measurements.

Thermal anemometers

Thermal annemometers, such as hot-wire or hot-film anemometers, are well-known instruments for flow measurements in water and gas. The sensor is usually a thin metallic element which is heated by electric current and exposed to the flow under investigation. Examples of a hot-wire and hot-film probe are shown in Figure 2.2. Owing to convective heat transfer, the temperature and hence the electrical resistance of the heated element is affected by the flow passing across it. Most of the sensors work on a constant-temperature mode, in which a feedback electronic circuit is used to heat the element and balance the cooling effect caused by the flow. To hold the element at a constant temperature at different flow conditions, the changes of the supplied electric current can be used to deduce the velocity of the flow. In practice, a hot wire is usually used for gases; it is made of platinum or tungsten with a typical diameter of 0.5-5 μm and a typical length of 0.1-1 mm. In comparison, a hot-film sensor consists of a very thin film of platinum (typically 1 μm) deposited on a quartz substrate. The substrate usually takes the form of a cylinder with a diameter of 25-100 μm, or sometimes a wedge or a cone. Hot films are usually used for liquids. Normally, such thermal anemometers have several distinct advantages: for instance, the spatial resolution and the response frequency are much higher; they can measure velocities of a wide range or of

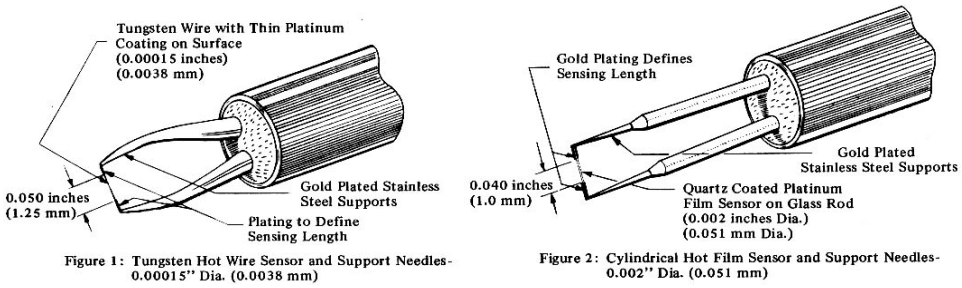

Figure 2.2: Examples of a hot-wire (left) and a hot-film probe (right).

multi-components. More detailed discussions concerning hot-wire and hot-film anemometers can be found in Comte-Bellot (1976), Perry (1982) and Bruun (1995).

Hot films were also used to measure the flows of liquid metals, such as mercury, woods metal and gallium, see for example Sajben (1965), Malcolm (1969), Hill & Sleicher (1971), Hunt & Welty (1973), Lykoudis (1973), Robinson & Larsson (1973) Alemany et al. (1979), Malcolm & Verma (1981), Trakas et al. (1983), Weier (1993) and Xu et al. (2006). However, one needs to pay special attention to the following aspects when applying the probe in liquid metals, which are always characterized with low Prandtl numbers: $Pr = \nu/\alpha$, where ν is the kinematic viscosity and α is the thermal diffusivity. The Pr number indicates the relative thickness of the momentum and thermal boundary layers. Concerning the heat transfer, small Pr indicates that the heat diffuses very quickly in comparison to velocity. Therefore, the thickness of thermal boundary layer surrounding a hot-film sensor can be much larger than the velocity boundary layer. As a result, the sensor becomes less sensitive to the flow direction. Besides, the frequency response of the sensor can be notably reduced due to the larger thermal zone too, since the time required for a thermal disturbance to diffuse through this becomes larger. In addiction, Malcolm (1969) also showed that the temperature drift in the liquid metal to be measured can result in remarkable errors of the measured velocity as well. At low velocities (a few cm/s), accurate results can only be obtained when the temperature drift is less than 0.1 °C. Based on these results, Moreau (1978) concluded that the hot film measurements must be conducted under the condition that the Péclet number built on the film diameter is clearly larger than unit. The Péclet number is defined as $Pé = U_\infty \cdot l_0/\alpha = Pr \cdot Re$, where U_∞ is the characteristic velocity of the incident flow, l_0 is the characteristic length scale.

Potential difference probes

A potential difference probe is able to detect the velocity of an electrically conducting fluid

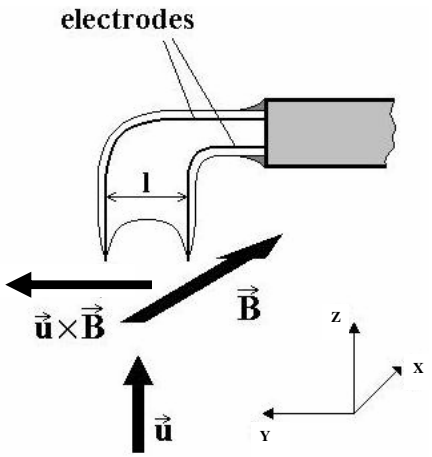

Figure 2.3: An illustration of the measuring principle of a potential difference probe.

by measuring the distribution of an electric field caused by the fluid motion in an external magnetic field. It has been widely used during the past, see Ricou & Vives (1982), Reed et al. (1986), Tsinober et al. (1987), Eckert (1998), Davoust et al. (1999), Eckert et al. (2001), Gelfgat & Gelfgat (2004), Cramer et al. (2006), Andreev et al. (2007) Bühler et al. (2008). As an example, Figure 2.3 illustrates a configuration of such probes. Consider a pair of thin electrodes with a distance of l in y direction, and they are exposed to a flow with velocity $\mathbf{u}$ in z direction as well as a static magnetic field $\mathbf{B}$ in x direction. If the total current $\mathbf{J}$ is small enough comparable to the flow induced one, the Ohm's law in equation (1.3) becomes

$$\nabla\phi = \mathbf{u} \times \mathbf{B} \tag{2.1}$$

which can be further written as

$$u = \frac{\delta\phi}{l \cdot B} \tag{2.2}$$

where the $\delta\phi$ represents the potential drop between the two electrodes. The assumption that $\mathbf{J}$ is negligible can be fulfilled in many situations; for instance in MHD channel flows at high Hartmann numbers and a small wall conductance ratio, and for the flows in the vicinity of such a small probe containing a miniature permanent magnet. In practice, the distance l between the electrodes is usually based on a compromise. On one hand, l should be as small as possible in order to deliver a high spatial resolution; on the other hand, the magnitude of obtained signal depends directly on the distance, and l also should be large enough to guarantee measurable signals. Another inherent disadvantage of the method is that the fluid velocity can only be measured in the presence of an external magnetic field, which may inevitably affect the original flow. If, on the other hand, the magnetic field is

produced by a small permanent magnet in the probe tip, the size of the probe can hardly be reduced down to a small enough region.

2.1.2 Non-invasive methods

As mentioned in the previous section, invasive measuring techniques usually suffer several drawbacks, such as disturbances to the flow, limited velocity information at a local position and sometimes harsh working environment for the sensors. For such reasons, several non-invasive methods appear to be favorable alternatives. For instance, radiation techniques, flow tomography based on induced magnetic field and ultrasound Doppler method become important tools recently.

X-ray tomography is a typical example of radiation measuring techniques. For example, Kakimoto et al. (1988) visualized the flow structures in molten silicon using X-ray radiography. Tungsten particles with multi-layers were added into the molten silicon to serve as tracers. As X-rays penetrated through the melt, the positions of the tracers can be followed because the absorption coefficients of tungsten and silicon are different. In this way, the flow field information can be obtained based on the trajectories of the tracers. X-ray techniques can be used to detect a temperature field in a convective flow too, because the variations in temperature lead to the variations in the fluid density, which further lead to the variation in the X-ray absorption as a sample is exposed to it. However, in a metallic melt of a low Prandtl number, the density changes only weakly as a function of temperature; therefore, such measurements demand additional effort to achieve a sufficiently high accuracy, as demonstrated by Koster et al. (1996). Other applications of X-ray can be found in the visualization of the evolution of metallic foams or the kinetics and morphology of solid-liquid interfaces during solidification, see Brunke & Odenbach (2006), Mathiesen et al. (2006) and Boden et al. (2008). In general, the thickness of the fluid domain is limited in order to let the X-ray penetrate through. More discussions concerning radiation measuring techniques can be found in Hussein (2003).

For liquid metal flows, it is also possible to obtain the velocity information by imposing an external magnetic field on the fluid. In this way, a flow field will generate a distribution of induced currents inside the liquid, which then gives rise to an induced magnetic field that is present both inside and outside the liquid. The structure of the induced magnetic field contains the information of the flow. Normally, the applied field should be so weak that it does not alter the flow to be measured. This technique is also suitable for conditions where a stronger magnetic field is intentionally needed and already present. More technical details

concerning the reconstruction of the velocity field can be found in Stefani et al. (2004).

Another promising way to measure flow velocities is to use the ultrasound Doppler method, often called ultrasound Doppler velocimetry (UDV) or ultrasonic profile monitor (UVP). This technique was originally used in medical engineering, see Atkinson & Woodcock (1982), and then it also has been applied in fluids engineering, see for example Takeda (1986). The measuring principle is based on the pulse-echo technique, which will be explained below. This technique is able to deliver a velocity profile along the ultrasound beam in real time. In comparison to other non-invasive techniques, such as the X-ray or the measurements of induced magnetic field, the ultrasound Doppler method can be applied to measure a flow with great ease. It can be used under regular laboratory conditions without additional concerns of hazardous radiations. Besides, the ultrasound can penetrate into a larger distance inside the liquid and allow the flow measurement free from boundary confinement. In addition, this measuring technique is very robust against the electric noises and therefore is especially suitable for measurements inside an electromagnetic field.

There are also other ultrasound measuring techniques in the literature, such as a time-of-flight method, see for example Andruszkiewicz & Sommerlatt (2008), which is able to measure the velocity of a moving particle. In this chapter, however, we will purely focus on the ultrasound techniques that directly deliver liquid velocities.

2.2 Fundamentals of ultrasound & Doppler effect

As the name indicates, the ultrasound Doppler method uses ultrasound as the tool to probe inside a medium. Ultrasound is a kind of sound wave which propagates in the form of mechanical vibration and possesses a frequency above the audible range (20 kHz). In practice, it usually lies in the range from a few to tens of MHz. The lower limit is determined by the wavelength (the longer the wavelength, the poorer the spatial resolutions), whereas the upper limit is mainly constrained by the attenuation effects, because the attenuation of ultrasound increases steeply as the frequency increases.

The Doppler effect, named after the Austrian mathematician and physicist Christian Doppler, describes the changes in frequency of a wave being perceived by an observer, who moves relatively to the source of the wave. When the source and the observer move towards each other, the observed frequency is higher than the emitted frequency; when they move apart from each other, the observed frequency is lower. The Doppler frequency f_d can be written as (see appendices)

$$f_d = \frac{2u}{c}\, f_e \tag{2.3}$$

where c is the velocity of ultrasound in the medium, and f_e is the emitted ultrasound frequency. It states that the frequency of the back scattered echo from a target P, for example a tracer in fluid, which moves with a velocity u in the direction of an ultrasound source, will be shifted from the emitted frequency f_e by an amount of f_d. Since f_e and c are generally known, the measurement of the Doppler shift allows the calculation of the velocity u directly.

2.3 Ultrasound Doppler instruments

Extensive investigations were carried out concerning the application of the ultrasound Doppler method during the past, see for example Atkinson & Woodcock (1982) and Jensen (1996). Generally, an ultrasound transducer emits the ultrasound into the medium under investigation; at the same time, the same or another transducer can be used to receive the reflected echoes. Ultrasound Doppler devices can be broadly divided into two categories, depending on whether a continuous wave (CW) or pulsed wave is used. The CW instrument is the simpler one in comparison. The pulse wave instrument has been developed later on and is more complicated. It has several dominating advantages which will be mentioned in the following parts. In fact, a pulse-wave instrument can be considered as an extended version which still possesses several common features of a CW device. More discussions can be found in Atkinson & Woodcock (1982).

2.3.1 Continuous wave instrument

In a CW instrument, a master oscillator produces a continuous sinusoidal waveform (usually a few MHz), which is firstly amplified and then used to drive the transducer. The transducer is mainly composed of a piezoelectric converter which transforms the electric energy into mechanical vibration energy, namely, the ultrasound wave. The generated ultrasound is then transmitted into the fluid under investigation. In practice, it is advantageous to arrange another solely receiving transducer to acquire the reflected echoes, which come from the targets in the overlapped beam area. The weak returning signal is amplified by a receiving amplifier and sent to the demodulator, where the Doppler information of the target motion is extracted. Various methods can be applied concerning the demodulation part. The details of such signal processing can be found in Atkinson & Woodcock (1982).

A distinct limitation of the CW method is that the position of the measuring volume cannot be easily adjusted, because the position is confined to the overlapped region of the beams from the emitter and the receiver. In contrast, an instrument based on pulse waves has the capability of range discrimination that allows the modifications of the size and the

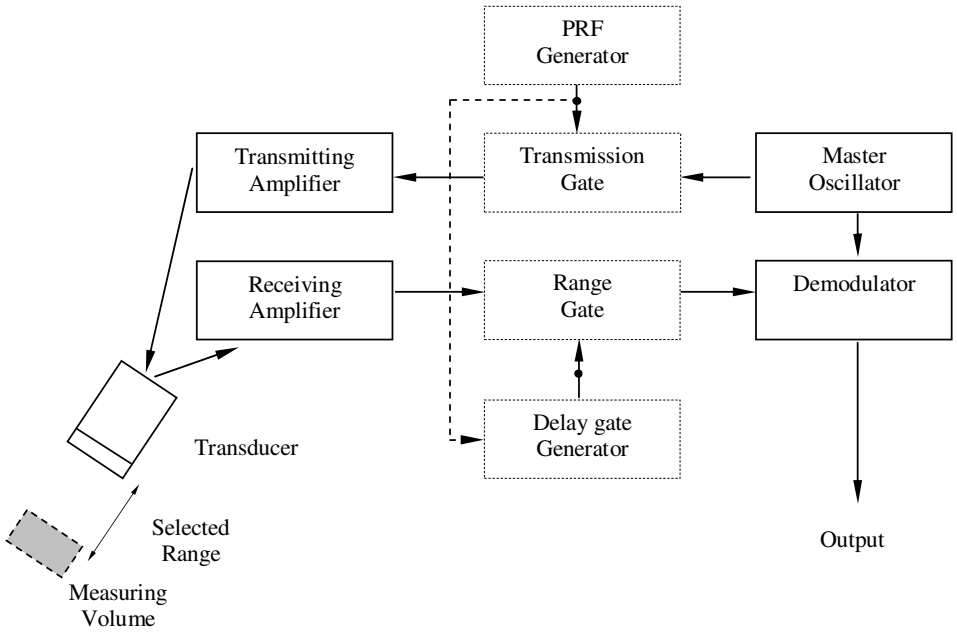

Figure 2.4: A diagram of hardware composition in a typical pulse-Doppler ultrasound instrument .

position of a measuring volume.

2.3.2 Pulse wave instrument

In a pulse wave instrument, the same transducer can serve as an emitter as well as a receiver (although other independent transducers may also work as receivers when necessary). The transducer emits only short pulses, each consisting of a few cycles (generally from 2 to 10 cycles). These pulses are emitted at a certain frequency, called the Pulse Repetition Frequency (PRF), which is generally within the range from hundreds of Hz to a few kilo-Hz. Between the emissions, echoes return to the transducer continuously, but not all of the echoes are analyzed. A receiver gate opens only at a controlled time instant for a specific time period so that only the echoes from the predetermined range on the ultrasound beam are acquired. This range is analogous to the overlapped beam region in the CW method.

A typical scheme of a pulse Doppler instrument is displayed in Figure 2.4 as suggested by Atkinson & Woodcock (1982). In the figure, the components in the solid-line blocks, including the master oscillator, transmitting amplifier, receiving amplifier and demodulator are the same as those in a CW instrument. Additional hardware used in a pulse Doppler instrument are shown in dashed blocks.

As the name indicates, the PRF generator ensures that the pulses are emitted at a fixed repetition frequency. The transmission gate only allows several cycles of ultrasound pulses to be transmitted at one time. A delay gate generator generates a time delay during which the transmitted pulses should travel to and come back from the selected range of interest; in other words, it controls the position of the measuring volume on the ultrasound beam. Finally, the range gate controls the echo sampling time, which directly corresponds to the axial size of the measuring volume. Additional delay gates and range gates can be added so that many measuring volumes can be processed in parallel. As a result, a profile of velocity can be recorded along the ultrasound beam. In practice, it is also possible to use a software program to fulfill the same function as the hardware gates. The necessary information for the velocity calculation can be obtained either by a spectrum analyzer that directly extracts the Doppler shift, or using correlation methods based on the signals in time domain.

2.3.3 UDV device: DOP2000

In this work, all flow measurements were carried out using a commercial UDV device, DOP2000 (model 2125, Signal-Processing SA). It is a pulse wave instrument with multi-gate functions controlled by software, which allows to adjust the position and the size of the measuring volume (in the beam direction) conveniently. The measuring volumes can be considered as a series of cylindrical disks aligned co-axially along the beam centerline. The lateral dimension of the measuring volume is determined by the diameter of the ultrasound beam, usually a few millimeters. The multi-gate technique enables the delivery of velocity profiles along the ultrasound beam. The obtained profiles correspond to the velocity component projected onto the beam. The "scan rate" of the profiles (in other words, the frequency of the consecutive profiles) can be adjusted by controlling the PRF values.

The structural layout of a pulse wave instrument has already been described before. In this section, we focus on the methods to obtain the velocity information using pulse waves. Detailed descriptions, especially for DOP2000, can be found in the user's manual (www.signal-processing.com). For the simplification of description, we consider only one particle here, which has a velocity component u projected on the ultrasound beam. Figure 2.5 shows that an ultrasound beam is emitted into a liquid medium together with a moving tracer inside a measuring volume. During one period of PRF, the particle moves a distance of ΔP (from P_2 to P_1), it is assumed to still stay in the same measuring volume. When the tracer has a distance of P_2 to the transducer, it takes a time of t_2 for the ultrasound to reach

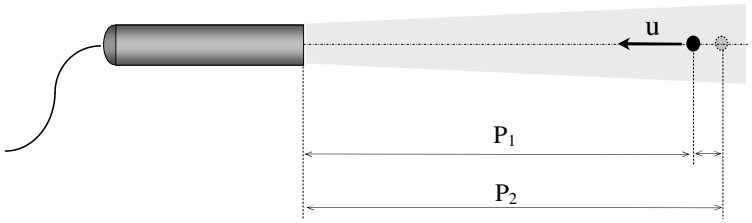

Figure 2.5: The working principle of time-of-flight in ultrasound Doppler velocimetry.

the tracer and come back (with a sound speed of c). The relationship is shown as

$$P_2 = \frac{c \cdot t_2}{2} \tag{2.4}$$

As the particle moves to P_1, a time period of t_1 is needed for that distance

$$P_1 = \frac{c \cdot t_1}{2} \tag{2.5}$$

Therefore, we have

$$u \cdot T_{PRF} = P_2 - P_1 = \frac{c}{2}\,(t_2 - t_1) \tag{2.6}$$

where the T_{PRF} is one time period of the PRF.

If we denote the time difference $t_2 - t_1$ as Δt, the particle velocity can be represented as

$$u = \frac{c}{2}\,\frac{\Delta t}{T_{PRF}} \tag{2.7}$$

Since c and T_{PRF} are both known quantities, the velocity u can be calculated immediately when Δt is known. In practice, however, the time difference Δt is always very short (in most cases it is less than a microsecond). It is advantageous to change the measurement of Δt into the measurement of the phase shift between the emitted and the received signals.

If φ represents the phase of an ultrasound wave and $\delta = (\varphi_2 - \varphi_1)$ represents the phase difference, then δ is related to the time difference as follows

$$\delta = \omega \cdot \Delta t = 2\pi f_e \cdot \Delta t \tag{2.8}$$

where ω is the angular frequency of the ultrasound. Generally, a correlation method can be used to extract the phase shift δ, based on the comparison between the emitted signals and the received echoes. In order to achieve statistically reliable results, a series of multiple pulses are emitted into the liquid and the resulted echo signals are analyzed together.

Actually, it can be noted that the DOP2000 does not really rely on the Doppler frequency to calculate the velocity; instead, it processes the signals in the time domain. It can be demonstrated that the two methods are closely related to each other (see appendices).

2.3.4 Operation parameters in DOP2000

After the description of the working principles of the device, this section focuses on the configurations of the operation parameters for flow measurements.

Emission frequency (f_e)

The emission frequency of a transducer is the fundamental parameter of a pulse Doppler device. It is determined by the matches between the master oscillator and the transducer's own resonant frequency. Generally, the frequency lies in the range from 1 to 10 MHz. As the ultrasound frequency decreases, the pulse duration becomes longer and the spatial resolution becomes poorer. However, as the frequency increases, the attenuation of the sound increases too, which limits the spatial distance that the ultrasound can reach.

Pulse repetition frequency (f_{PRF})

As mentioned above, a pulse wave device emits short bursts of ultrasound at a regular frequency f_{PRF}. Actually, it determines the maximum depth that can be reached (P_{max}) and the maximum velocity that can be measured (u_{max}). This can be explained as below. Since the ultrasound needs to take a round trip to reach the maximum depth, there is

$$P_{max} = \frac{c \cdot T_{PRF}}{2} = \frac{c}{2f_{PRF}} \tag{2.9}$$

On one hand, owing to the Nyquist theorem, the maximum detectable Doppler frequency shift is limited as

$$f_{d_{max}} = \frac{f_{PRF}}{2} \tag{2.10}$$

On the other hand, according to equation (2.3), we have

$$f_{d_{max}} = \frac{2f_e}{c}\, u_{max} \tag{2.11}$$

As a result, the maximum measurable velocity can be written as

$$u_{max} = \frac{c \cdot f_{PRF}}{4f_e} \tag{2.12}$$

Finally, from equation (2.9) and equation (2.12), the following constraint can be derived

$$P_{max} \cdot u_{max} = \frac{c^2}{8f_e} = const \tag{2.13}$$

which tells that there has to be a compromise between the maximum measurable depth and the maximum measurable velocity when the emission frequency of the transducer is decided. Since the sound speed is generally a fixed value in a liquid, the increase in the emitting frequency will decrease the product of the maximum depth and the maximum velocity that

can be measured. It can be noted that the *const* in equation (2.13) does not depend on f_{PRF}.

Measuring volume

A pulse wave device emits a train of short waves towards a target and then waits for echoes to return. The device samples only at a fixed time after the emission, therefore, only the signals reflected by the targets inside a specific region are obtained. Such a specific region can be considered as the measuring volume (or the sampling volume). The length of the emitted pulse directly determines the longitudinal dimension of the measuring volume. It is desirable to have pulses as short as possible, however, this is limited by the signal-to-noise ratio level. The DOP2000 can emit pulses containing 2, 4 or 8 cycles.

The lateral size of the measuring volume depends on the diameter of the ultrasound beam at that place, which is furthermore related to the diameter of the piezoelectric disk and the divergence angle of the ultrasound beam. For a transducer with a flat and round radiating surface, the simplified pressure field of the emitted ultrasound wave is shown in Figure 2.6. At the beginning, the beam lies in a cylindrical region until it extends to a distance of Z_0. Afterwards, the beam starts to diverge with an angle of θ. The region within Z_0 is named as "near field"or "Fresnel zone", and the distance Z_0 is

$$Z_0 = \frac{r^2}{\lambda} \tag{2.14}$$

where r is the radius of the transducer and $\lambda = c/f_e$ is the wavelength. The region beyond Z_0 is called "far field" or "Fraunhofer zone". The angle of divergence is

$$\theta = \arcsin\left(0.61\frac{\lambda}{r}\right) \tag{2.15}$$

In fact, an exact expression of the pressure field can be calculated using the Huygens' principle. The details can be found for instance in the book of Jensen (1996). Based on equations (2.14) and (2.15), a simple estimation can be made for an ultrasound wave in water ($c = 1480$ m/s). For the ultrasound beam generated by a 4 MHz transducer with a 5 mm diameter, there are $Z_0 = 16.7$ mm and $\theta = 5.2°$. Table 2.1 lists the sizes of measuring volume in water, 85% glycerin and GaInSn at a position of 100 mm in front of the transducer.

Number of emissions per profile (N_{epp})

The measurement of "Doppler frequency" (or phase shift) is based on the correlations that exist between different emissions. The correlation requires many ultrasound emissions. Each emission can be considered as a particular realization of a random process. The number of

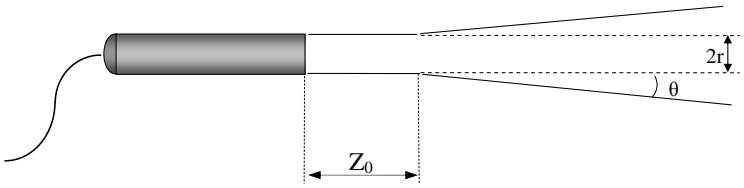

Figure 2.6: An idealized sketch showing the ultrasound beam divergence.

	water	85% glycerin	GaInSn
sound velocity (m/s)	1480	1904	2650
measuring volume size in longitudinal direction (mm) (burst of 4 cycles)	0.74	0.95	1.37
measuring volume size in lateral direction (mm) (100 mm in front of the sensor)	5.7	7.3	10.5

Table 2.1: The sizes of the measuring volume in water, glycerin and GaInSn, the ultrasound is generated by a 4MHz transducer with a 5mm diameter.

emissions per profile determines the time between profiles, $T_{profile}$, as

$$T_{profile} = T_{tran} + T_{PRF} \cdot (N_{epp} + N_{sd}) \tag{2.16}$$

where T_{tran} is the time period used for data transfer (around 1.5ms in DOP2000), and N_{sd} is a fixed number of emissions which is always included by the software ($N_{sd} = 16$ in DOP2000). In practice, the frequency of the consecutive velocity profiles delivered by DOP2000 can be varied from a few Hz to several tens of Hz.

2.4 UDV application in fluid mechanics

Besides the application in medical engineering, the UDV has also become a powerful tool for flow measurements in the investigation of fluid mechanics over the last 20 years. It is used for flow measurements in conventional transparent liquids such as water, as well as in opaque ones such as liquid metals. This section will give a review on previous works using this technique.

2.4.1 UDV for transparent liquid

One of the pioneering works concerning UDV for velocity profile measurements was presented by Takeda (1986). Two kinds of classical hydrodynamic problems are investigated in his experiments: a simple Poiseuille pipe flow and a Taylor vortex flow. Water is used as the working fluid for both experiments. For the Poiseuille flow, a transducer is arranged outside the pipe wall. The test section is immersed into a water bath, which provides a good acoustic coupling and minimizes the reflections of the ultrasound beam. The profiles of the measured mainstream velocity show a parabolic distribution (a characterization of laminar pipe flow) if $Re < 2145$, whereas the profiles change into a distribution of 1/7 power law (a characterization of turbulent pipe flow) if $Re \sim 6565$. The second experiment is concerned with the flow in a gap in a concentric double cylinder. The outer cylinder has a diameter of 11 cm and is fixed all the time, whereas the inner one has a diameter of 10 cm and is rotating. The transducer is arranged at the bottom of the cylinder and directed upwards. In this way, the distributions of the axial velocity along the height of the cylinder can be measured. The obtained profiles show clear reversals of velocity signs, corresponding to the well-known Taylor vortex structures.

Since the UDV delivers velocity profiles immediately, it can be used to measure large flow structures which are varying with time and space. The wakes behind a cylinder or a torus, respectively, were studied by Inoue et al. (1999) and Peschard et al. (1999). In their experiments, the spatial sizes and the temporal variations of the wakes are clearly visualized. The measured results are compared with those acquired by other measuring techniques, such as hot film anemometry and flow visualizations. A good agreement verifies the reliability of the results. Ern & Wesfreid (1999) and Takeda (1999) investigated the instabilities and the transitions of the flow between concentric rotating cylinders. They used Fast Fourier Transformation (FFT) and Proper Orthogonal Decomposition (POD) to analyze the time series of the measured velocity profiles.

2.4.2 UDV for liquid metal

Besides transparent liquids, the UDV is appropriate for flow measurements in opaque fluids, such as liquid metals. One of the earlier works was carried out by Takeda (1987), who measured flows of mercury in a T-branch. Afterwards, more experiments are conducted and several technical aspects are discussed, such as reflecting particles, acoustic couplings and the qualities of the acquired signals. Brito et al. (2001) investigated the rotating motion of liquid gallium (whose melting point is about 30 °C) in a copper cylinder, where a spinning top disk

drives the flow. They measured the primary component of the rotating flow using UDV. The transducers are coupled to the cylinder wall from outside. Since they used clean gallium in the experiment, an amount of ZrB_2 particles were added to the melt to serve as tracers. The ZrB_2 particles have a density of 6.17×10^3 kg/m^3, which is close to that of gallium (6.09×10^3 kg/m^3). They also notice that the melt can be quickly oxidized when exposed to air, and the oxide particles can serve as tracers in the measurements. However, too many oxide particles can effectively enhance the ultrasound attenuation and reduce the distance the ultrasound can reach. Takeda & Kikura (2002) measured the mercury flows contained in a hemispherical container of stainless steel in a loop in Riga. Multiple transducers are used to catch a two-dimensional flow field distribution. Unlike gallium, the pure mercury is a noble metal which cannot be easily oxidized. To achieve a sufficient amount of tracers, they injected nitrogen gas into the mercury before measurements. In this way, it is expected that for some minute gas bubbles existing in the mercury work as tracers for a limited period of time.

Recently, the liquid metal GaInSn is widely used as a working fluid. The flow driven by a rotating magnetic field in a closed cylinder was measured by Cramer et al. (2004). The results show that the secondary flow in a cylinder meridional plane consists of two vortex pairs due to the Ekman effect. In the experiments, the amount of tracers directly influences the ultrasound attenuation, which further influences the signal quality. Too few tracers lead to worse signals because of the poor correlations, whereas too many tracers result in strong attenuations and weak echoes, which directly limit the maximum distance that can be measured. It is expected that there should be a compromise concerning the optimal amount of tracers. In practice, it is possible that the GaInSn can contain too many tracers. For instance, minute air cavities can come into the bulk during the process of filling the melt into the cylinder, or oxidation can appear when the melt is exposed to air. Since it is difficult to quantify the amount of tracers in the bulk, the criteria to judge the optimal conditions are still rather empirical up to now.

The measurements of hot liquid metals are very difficult up to now. The commercial transducers cannot be used directly. Therefore, additional modules need to be applied to bridge the transducer and the hot medium. A waveguide sensor was developed by Eckert et al. (2003) and applied successfully in several high temperature metals, such as PbBi within the range of $200-400\,^{\circ}$C, CuSn around $600\,^{\circ}$C and liquid aluminum at about $750\,^{\circ}$C. However, the duration of the measuring time is limited.

In summary, we can see that the UDV has demonstrated its capacity for the measurements of liquid metal flows through various experimental studies. Questions may arise when the UDV is applied to the measurements of gas-liquid two-phase flow. The influence of larger

gas bubbles on the measured results are not investigated in literature. In the following parts, the UDV will be used to measure several two-phase flow problems, which are chosen to test its capability.

2.4.3 UDV for two-phase flow

Gas bubbles in water can be considered as ideal reflectors for ultrasound, because of the distinct difference of acoustic impedance at the gas-liquid interface, see for example Krautkrämer (1990). This can be briefly explained in the following way. The acoustic impedance Z is defined by

$$Z = \rho \cdot c \tag{2.17}$$

where ρ is the density of the medium and c the sound velocity. Typical values of the acoustic impedance are 1.5×10^6 N·s/m^3 for water and 1.5×10^3 N·s/m^3 for air.

When the dimension of an object is much larger than the wavelength of an incoming wave, the reflection coefficient at interface, R, can be considered as a criterion to judge if the object works as an ideal reflector or not. R is expressed as

$$R = \frac{(Z_2 - Z_1)^2}{(Z_2 + Z_1)^2} \tag{2.18}$$

where Z_1 and Z_2 represent the corresponding acoustic impedance of the two adjacent media, respectively. R is nearly 1 at the air/water interface and about 0.935 at a water/steel interface. Therefore, it is justified to consider a gas bubble, or a sphere of stainless steel, as a good reflector in water.

Ultrasound methods have been used in several experiments to measure the single- or multi-bubble motion. Andreini et al. (1977) detected the noises generated by the bubbles released from an orifice attached to a brass seal by an acoustic microphone. In this way, they were able to determine the frequency of bubble formation and consequently the bubble diameter in tin and lead. Recently, an ultrasound Doppler instrument based on continuous waves was developed by Mordant et al. (2000, 2004, 2005). They used the device to track the settling motion of a solid sphere in a bulk of stagnant liquid, as well as the Lagrangian trajectory of a particle in a turbulent flow. The apparatus is also used to study the motion of a single bubble rising in water or other non-newtonian liquids, and three dimensional trajectories of the rising bubbles can be fully reconstructed. Since the instrument uses continuous waves, its sampling frequency can be very high (for example no limitation due to T_{PRF}). However, this technique focuses on the motion of a single object, such as a rising bubble or a moving particle, and it does not simultaneously measure the velocity of the ambient flow, such as the

velocity distribution in the wake behind a bubble. In comparison, a device based on pulse waves can deliver simultaneously the velocity of the moving object and the ambient flow, although sampling frequency cannot be as high as that of a continuous-wave one.

Several experiments are conducted to measure two-phase flows by UDV. The flow problems under consideration include a bubbly pipe flow and a bubble column, see for example, Suzuki et al. (2002) and Wang et al. (2003). However, there are still many unanswered questions. The ultrasound signals can be extremely complicated by the multi-bubbles randomly appearing on the beam line, especially when multi-reflections need to be considered.

In this work, we will study several simple test problems step by step. The experimental results can be compared either with the data in literature or with those obtained by other measuring techniques in parallel. In this way, the results from DOP2000 can be verified directly and the capability of the device can be explored.

2.5 Test problems for UDV in two-phase flow

In this section, three test problems are investigated. The DOP2000 is applied to measure the velocity of a settling sphere, a rising bubble, as well as the flow driven by a bubble chain. These problems can be considered as simplified models which represent several key features of the bubble-driven flow. We carry out the experiments in transparent liquids, which allow optical methods like LDA to measure the flow in parallel.

2.5.1 Settling sphere experiment

We start with the experiment of a solid sphere settling down in a stagnant liquid. Complications such as the deformation or oscillation of the object surface do not exist. Furthermore, the sphere settles down with a linear trajectory when its density is large enough in comparison to that of the liquid, see Mordant & Pinton (2000).

The experimental setup is shown in Figure 2.7. The liquids in use were water solutions of glycerin with different concentrations, whose physical properties are taken from D'Ans & Lax (1992). The fluid was stored in a cylindrical Perspex vessel with a diameter of 0.125 m and a height of 0.3 m. At the free surface, a 4 MHz ultrasonic transducer was immersed vertically into the liquid to make the emitted beam coincide with the axis of the cylinder. Therefore, the velocity distributions along the vessel axis can be measured. Specifically, the transducer measured the vertical component of the velocity along the axis. We used spheres of stainless steel with diameters from 2.0 to 7.5 mm. Each sphere was released directly

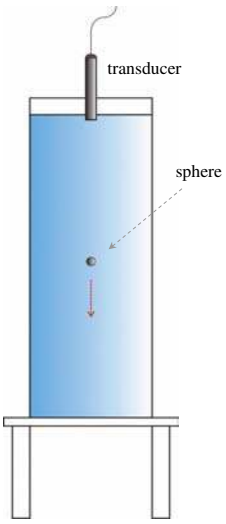

Figure 2.7: Experimental setup for the velocity measurements of a settling sphere.

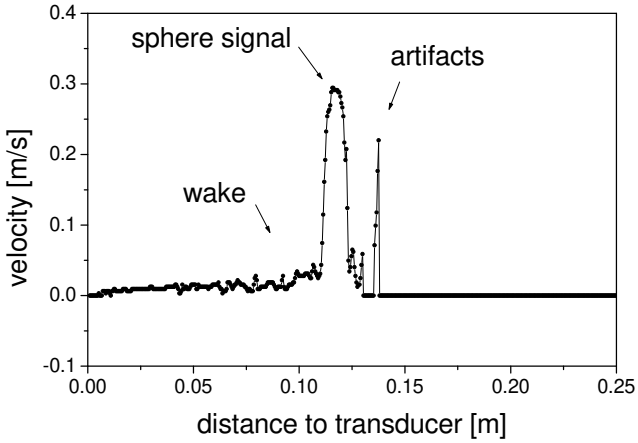

Figure 2.8: A snapshot of a typical velocity profile acquired by DOP2000 when a solid sphere settled down in glycerin.

below the transducer. In this way, we observed the velocity of the sphere and its wake simultaneously until the sphere reached the cylinder bottom.

We focus on the terminal velocity of the sphere when the settling motion is steady. As a validation, the velocity magnitude acquired by DOP2000 can be compared with the classical results in literature, for example, the standard curve of drag coefficient C_D and Reynolds number Re of a sphere, see Clift et al. (1978).

Figure 2.8 shows a snapshot of the typical velocity profile when the sphere settles down in the liquid. A sharp peak of velocity can be observed. In the experiment, the position of the

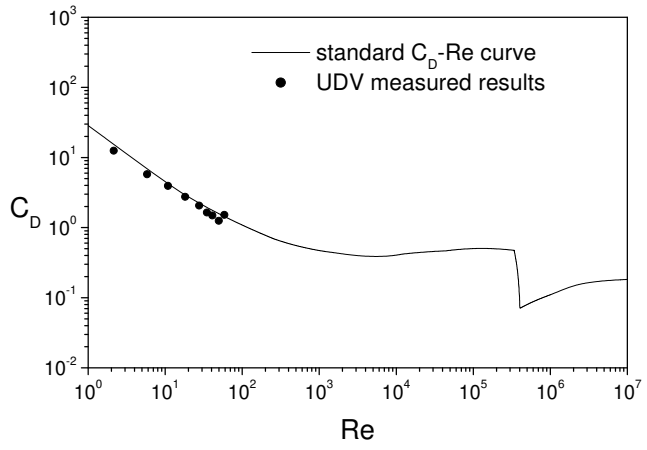

Figure 2.9: Comparison of the results measured by DOP2000 to the standard drag curve of a sphere.

velocity peak moves with the settling sphere. The height of the peak becomes steady after an initial increase. This indicates that the peak corresponds to the velocity of the sphere. A wake region is visible behind the sphere. The velocities there are smaller and decay with time gradually. The liquid is still stagnant in front of the sphere. The velocities are zero everywhere except several places showing sharp spikes. For different runs of the experiment, the spikes are always sharp and narrow; in addition, they appear at random locations and do not represent any physical meaning of the flow.

We obtained comparable velocity profiles in various experiments of various sphere diameters. The profiles change only quantitatively in the velocity magnitudes. If the maximum of the velocity peaks is considered as sphere velocity u_T, the drag coefficients C_D of the spheres can be determined according to the following equation (Clift et al. 1978)

$$C_D = \frac{4}{3} \frac{(\rho_p - \rho_l) d_p g}{u_T^2 \rho_l} \tag{2.19}$$

where ρ_p and d_p represent the density and diameter of the sphere and ρ_l represent the density of the liquid, respectively. These results reveal a good agreement with the standard $C_D - Re$ curve of a sphere, as shown in Figure 2.9. Therefore, the capability of the DOP2000 to measure the velocity of spherical bodies in liquids is demonstrated.

2.5.2 Rising bubble experiment

As the next step, the DOP2000 was used to measure the velocity of a gas bubble rising in stagnant tap water and the glycerin solvent. The experimental configuration was similar to that in the solid sphere experiment. A sketch of the set-up is displayed in Figure 2.10. The

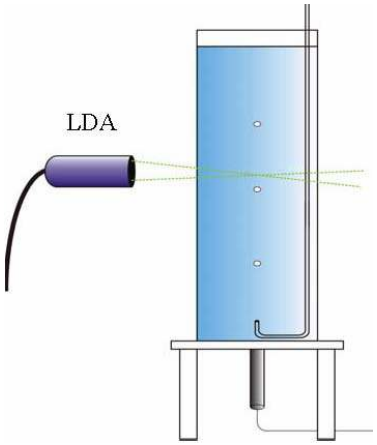

Figure 2.10: Experimental configuration of the measurements of the bubble driven flow using UDV and LDA. (A chain of bubbles is sketched here instead of a single bubble case)

cylindrical vessel was the same as the one used in the previous section. Gas bubbles were injected into the liquid through a single nozzle of stainless steel. The outer diameter of the nozzle was 3 mm. Different orifices were used to vary the inner diameter between 0.3 mm and 1.5 mm. A mass flow controller (MKS 1359C, MKS Instruments) was used to regulate the gas flow rate, which was in the range of 0.005-0.02 cm^3/s in order to guarantee a regime of single bubbles. This resulted in intervals of about 15 s between two consecutive bubbles. The DOP2000 showed that the wake of a bubble decayed completely during this time. Therefore, the influence caused by the preceding bubbles can be considered as negligible.

The ultrasonic transducer was installed at the bottom wall of the cylinder, with the beam directed vertically along the bubble path. The recorded velocity profiles are very similar to those of solid spheres. In fact, the measured peak represents the vertical component of the velocity coming from the rear interface of the bubble, which is facing towards the ultrasonic transducer. In the experiment, it is observed that small bubbles possess a spherical shape. For larger bubbles, the bubble shapes are deformed and become close to an ellipsoid (more discussions concerning this topic will be given in the next chapter).

The parameter d_e, called "equivalent bubble diameter", is used as a measure for the bubble size, see Clift et al. (1978). It can be estimated according to the following equation based on the injected gas volume V during a time period and the number of bubbles n generated in the same interval

$$d_e = \left(\frac{V}{n} \cdot \frac{6}{\pi} \right)^{1/3} \tag{2.20}$$

Figure 2.11 displays the terminal rising velocity of the bubbles u_T as a function of the

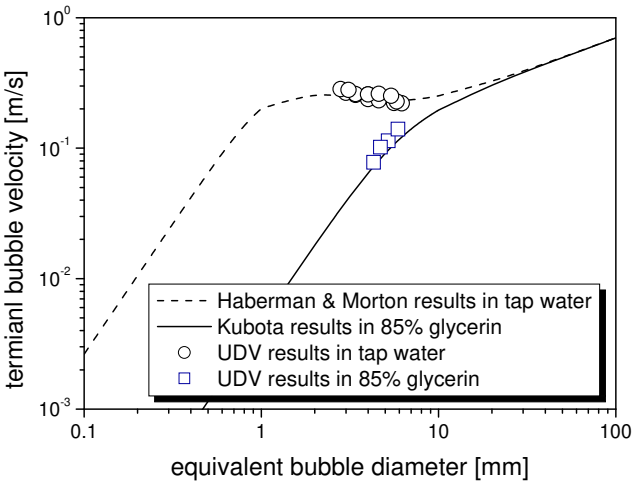

Figure 2.11: Bubble terminal rising velocities as a function of the equivalent bubble diameter.

equivalent bubble diameter d_e. The dots are the results measured by DOP2000 in the present work. We compare our measured values with curves fitted from experimental results reported by Haberman & Morton (1953) and Kubota et al. (1967) for water and glycerin, respectively. The agreement can be considered as satisfying.

2.5.3 Bubble chain flow experiment

In this section, we focus on the liquid velocity in a flow driven by a bubble chain. The experimental set-up was the same as depicted in Figure 2.10. The gas flow rate was increased to 0.18 cm^3/s. A chain of bubbles was generated and rose up continuously, which induced a recirculation motion in the liquid bulk. Measurements of the velocity profiles along the cylinder axis were carried out by the DOP2000 as well as an LDA system (DANTEC). The data from the two measuring techniques can be compared afterwards.

In the experiment, the LDA device works on a back scatter mode, which is a well developed measuring technique. Detailed discussions can be found, for example, in Durst et al. (1981). There are many studies concerning the LDA measurements for two-phase flows, see for example Mudde (2005) and the reference therein. Specifically, the signals of LDA in a flow driven by a bubble chain are investigated by Mudde et al. (1998). They found that the contribution of the bubble signals is negligible for a LDA with back scatter mode; in other words, the liquid velocities are measured predominantly. Additional application of thresholds to try to eliminate the contributions of the bubbles do not have a significant effect on the results. Therefore, we assume that the data measured by LDA are liquid velocities in this work, as long as the flow is driven by a bubble chain.

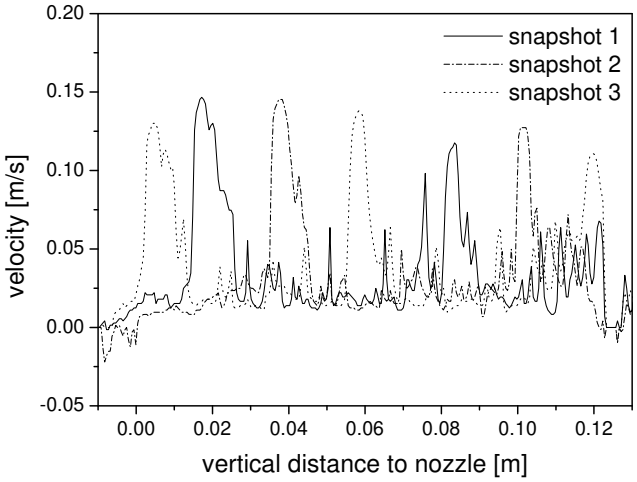

Figure 2.12: Typical examples of velocity profiles acquired by DOP2000 in the flow driven by a bubble chain, three consecutive snapshots are given.

Figure 2.12 shows several typical velocity profiles recorded by DOP2000 in a bubble-chain driven flow. The profiles contained the velocity signals of two or three bubbles, as well as some narrow spikes which cannot be related to them. The occurrence of such spikes are noticed in the sphere experiment, too. In the experiment, the possibility to generate such artifacts increases significantly when the gas flow rate is increased.

Generally, there are large differences between the gas velocities and liquid velocities. Therefore, a threshold method can be used to extract the liquid velocities from such profiles. We developed a threshold method to calculate the liquid velocity based on the velocity histograms. Figure 2.13 shows the velocity histogram from the velocity time series at the mid-height of the cylinder axis. We can observe a two-peak distribution, which corresponds to the velocities of gas and liquid, respectively. The measured values between the two peaks come from the artifacts described above.

We explain the procedure to select the threshold. At the beginning, a constant-value threshold is applied on every velocity snapshot to cut off the bubble signals and distinct spikes. The signals above the threshold are eliminated. In addition, the signals from their neighboring points are deleted too, although they are not always above the threshold. In other words, several points adjacent to an artifact spike are removed as well, because it is not clear if these data represent the real flow velocities or not (more discussions concerning the number of the adjacent points being removed will be given below).

The value of the first threshold can be determined based on the snapshots of the velocity profile and the distributions of velocity histogram, see Figure 2.12 and Figure 2.13, respec-

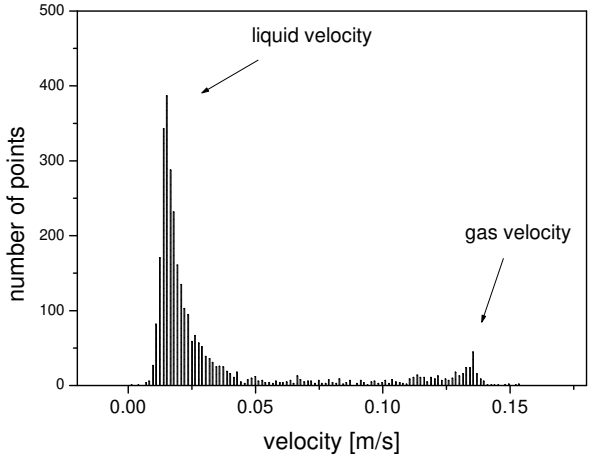

Figure 2.13: Histogram of the vertical velocity measured at mid-height of the centerline of the bubble chain, based on the velocity time series at that point.

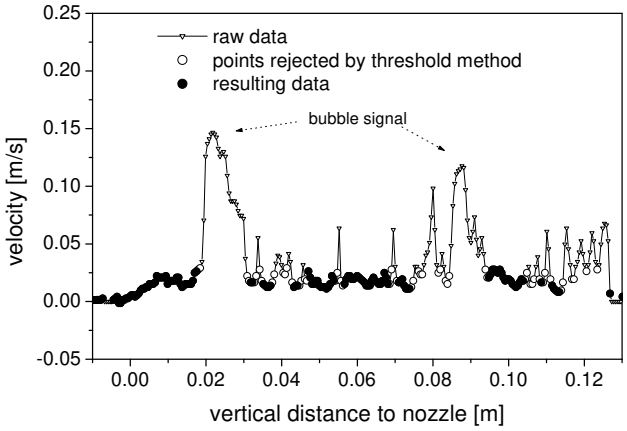

Figure 2.14: A velocity profile acquired by DOP2000 in the flow driven by a bubble chain, as well as the results after the threshold method applied on it.

tively. When the velocity differences between the two phases are large, such as in the present situation, the value can be chosen easily. The value for the threshold is 0.03 m/s here. It can be a higher one as well, such as 0.04 m/s. This does not change the final results significantly, because it is just the first-round filtering of the data. The filtered profile is shown in Figure 2.14 as solid dots. For this figure, at each spatial position where the signal is higher than the threshold, we choose that two neighboring points on each side of it should be deleted too.

For the above filtered results, further thresholds are applied repeatedly to remove lower spikes, which can be artifacts, too (this procedure is not shown in Figure 2.14). The velocity histograms are evaluated again. The histogram distributions are changed because the signals

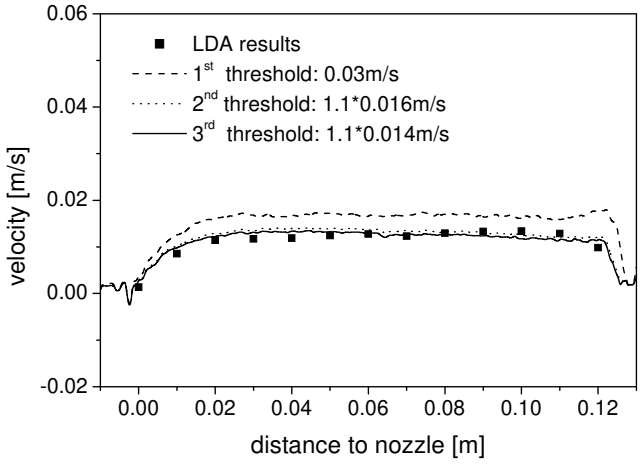

Figure 2.15: Time-averaged profiles of the liquid velocity resulting from different steps of the iterative threshold method. Comparison of the UDV measurements with corresponding results obtained by means of LDA.

of those adjacent points are removed. For each location on the bubble chain centerline, the velocity magnitude corresponding to the maximum peak in its histogram is selected as the reference for the threshold of the second round. Those velocities obtained from different locations are multiplied by a coefficient larger than unity in order to take into account the flow fluctuations, which are related to the width of the histogram distribution. For the current flow, the coefficient is chosen to be 1.1. The new threshold is then applied to the velocity profiles again. Similar to the previous round, the new threshold removes the signals above it and simultaneously deletes their adjacent points. The procedure is repeated several times until the results obtained from two subsequent rounds are almost the same.

The development of the filtering process of the velocity profiles can be followed in Figure 2.15. At first, the bubble velocities are eliminated by a constant threshold of 0.03 m/s, which gives a time-averaged result of the liquid velocity shown as dashed line (the highest curve). The second threshold is found to be 0.016 m/s. After the multiplication of the coefficient 1.1, it is applied again on the data. The resulted profile of time-averaged velocities is shown as dotted line. Evaluating the histograms again, the third threshold value is 0.014 m/s. As it is applied, the achieved result (solid line) is very close to the previous one. Therefore, we consider the velocity profile after the third iteration as the final result. The corresponding profile of the liquid velocity from the LDA measurements is also included into the figure and a good agreement can be observed.

In the aforementioned procedure, there are two aspects which need further discussion;

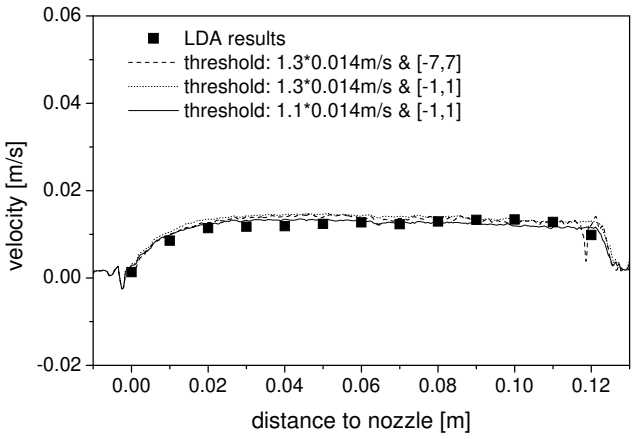

Figure 2.16: Effects of modifications of the turbulence coefficient and the number of neighboring points to be eliminated.

namely, the coefficient multiplying the threshold, as well as the number of adjacent points eliminated together with the spikes. For the present flow problem, the coefficient is varied from 1.1 to 1.3, and the number of neighboring points is changed between 2 and 14. The influence on the final results shown in Figure 2.16 can be considered as negligible.

The flow problem here is a simple bubble-driven flow. There are several reasons why the study is focused on it. Firstly, the few number of bubbles minimizes the measuring difficulties, such as the complicated multi-reflections among different bubbles and strong turbulent fluctuations of the liquid. Another important advantage is the application of LDA, which provides a reference for the validation of the threshold method. When the gas flow rate is increased, it becomes complicated to apply the threshold method. This is not only because the signals from the DOP2000 are more noisy, but also because it is difficult to acquire reliable results by other measuring techniques. Therefore, the validation can become less trustworthy. For example, the reflections and refractions at the bubble interface can significantly disturb the optical techniques when the void fraction is high, whereas intrusive methods such as hot film anemometry also encounter numerous difficulties concerning the phase separation. Detailed and comprehensive investigations of this topic demand huge efforts and go beyond the scope of this thesis. In following chapters, we constrain our investigation to the problems where the gas flow rate is very low; specifically, the flow is driven by a single bubble or a weak plume of dispersed bubbles with low void fraction.

Chapter 3

Flow driven by a single bubble in a static magnetic field

The motion of a single bubble in a bulk of stagnant liquid metal is investigated in this chapter. Specifically, the study is focused on the influence of a static magnetic field on the bubble motion as well as the bubble-induced liquid motion. At the beginning, we introduce some dimensionless parameters related to the flow problem. Next, we present a brief literature review, concerning the shape, velocity and path of a rising bubble and its wake. Then, we show the experiments concerning the single bubble motion in GaInSn without a magnetic field. The velocities of the bubble and its wake are measured simultaneously by DOP2000. We validate the results with theory and other experimental data in the literature. After that, the flow is exposed to a static magnetic field. We consider two different configurations with the field in the vertical and the horizontal direction, respectively. In the end, a discussion is given concerning the results.

3.1 Dimensionless parameters

For a bubble rising freely through liquid, the following dimensionless parameters are usually used to characterize the flow problem (Clift et al. 1978):

Reynolds number

$$Re = \frac{\rho u_T d_e}{\mu} \tag{3.1}$$

Eötvös number

$$Eo = \frac{\rho g d_e^2}{\sigma} \tag{3.2}$$

Morton number

$$Mo = \frac{\mu^4 g}{\rho \sigma^3} \tag{3.3}$$

where g represents gravity, and ρ, μ and σ are the density, dynamic viscosity and surface tension of the liquid respectively; u_T is the terminal bubble rising velocity, and d_e is the

equivalent bubble diameter defined by

$$d_e = \left(\frac{6V}{\pi}\right)^{\frac{1}{3}} \tag{3.4}$$

with V denoting the bubble volume.

For the above parameters, the Re number represents the ratio of inertial force to viscous force; the Eo number indicates the ratio between buoyancy force and surface tension force. The third parameter Mo is also called Haberman-Morton number Hm, which only depends on the physical properties of the liquid.

Several other dimensionless parameters are often encountered in literature as well; in fact, they can be derived from the above ones:

Weber number

$$We = \frac{\rho u_T^2 d_e}{\sigma} = \frac{Re^2 Mo^{1/2}}{Eo^{1/2}} \tag{3.5}$$

Drag coefficient

$$C_D = \frac{4gd_e}{3u_T^2} = \frac{4Eo^{3/2}}{3Re^2 Mo^{1/2}} \tag{3.6}$$

The We number can be considered as the ratio of the dynamic pressure ρu_T^2 to the surface tension force, where the first one causes the bubble shape to distort and the latter one resists to that distortion. The parameter C_D is used to refer to the total drag D exerted on a bluff body in a stream of speed U_0,

$$C_D = \frac{D}{\frac{1}{2}\rho U_0^2 A} \tag{3.7}$$

where A is the area of the projection on a plane normal to the stream, see Batchelor (1967). Usually, the drag on a bubble is very complicated. It depends on many factors such as the bubble velocity, the bubble shape and the fluid flow surrounding it. The problem can be simplified when the flow is steady; in other words, if the bubble rises steadily at the terminal velocity u_T, then the drag and the buoyancy force balance each other (Haberman & Morton 1953), which gives rise to equation (3.6). In literature, the same formula of C_D is also used to represent the time-averaged value when the flow is not strictly steady, for instance, when u_T fluctuates periodically, see Clift et al. (1978).

Harper (1972) suggested a classification for liquids based on the Morton number Mo. In high-Mo liquids, C_D decreases monotonically as the bubble Re number increases; whereas in low-Mo liquids, the $C_D - Re$ curve has a minimum. This can be observed from the curves labeled from G to M in Figure 3.1. Generally, a liquid metal has a high surface tension and a low viscosity, which lead to an extremely low Mo number (for instance, GaInSn has a $Mo \sim 2.2 \times 10^{-13}$). Therefore, the non-monotonic variation in the $C_D - Re$ curve can be expected in this work.

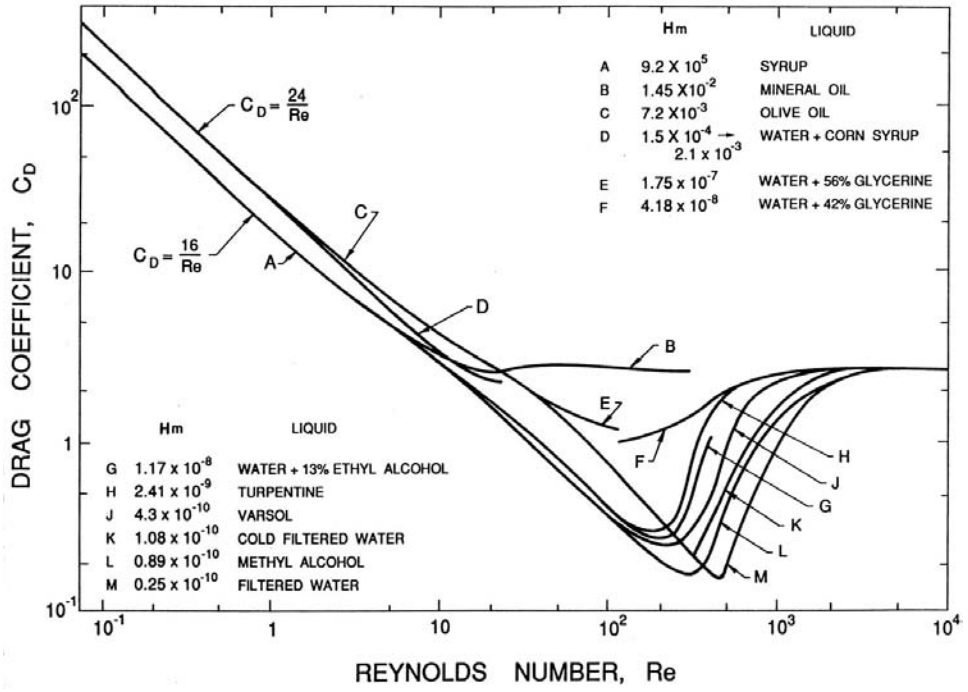

Figure 3.1: Drag coefficient as a function of Reynolds number for bubbles in various liquids. The figure is given by Haberman & Morton (1953).

3.2 Single bubble motion: a literature review

The rising motion of a single bubble in stagnant liquid has been attracting researchers' attention for a long time. Research interests are mainly focused on topics such as the shape, velocity, trajectory of a rising bubble and the liquid flow surrounding it. Comprehensive reviews are given, for instance, by Clift et al. (1978), Fan & Tsuchiya (1990), Brennen (1995), Magnaudet & Eames (2000), de Vries (2001) and Loth (2008a,b).

3.2.1 Bubble shape

As a gas bubble rises up, its shape usually can be classified into several categories, such as spherical, ellipsoidal and spherical-cap. Some typical examples are shown in Figure 3.2. Conventionally, a bubble is called spherical if the minor to major axis ratio lies within 10% of unity, see Clift et al. (1978), Fan & Tsuchiya (1990). The term "ellipsoidal" is used to refer to the bubbles which are oblate, although the actual shape of the bubbles may be considerably different from a true ellipsoid. For instance, the shape may not be fore-and-aft symmetric, and the bubble may undergo periodic dilations or random wobbling motions. A "spherical cap" denotes a large bubble with a flat or indented base and lacks any semblance of fore-

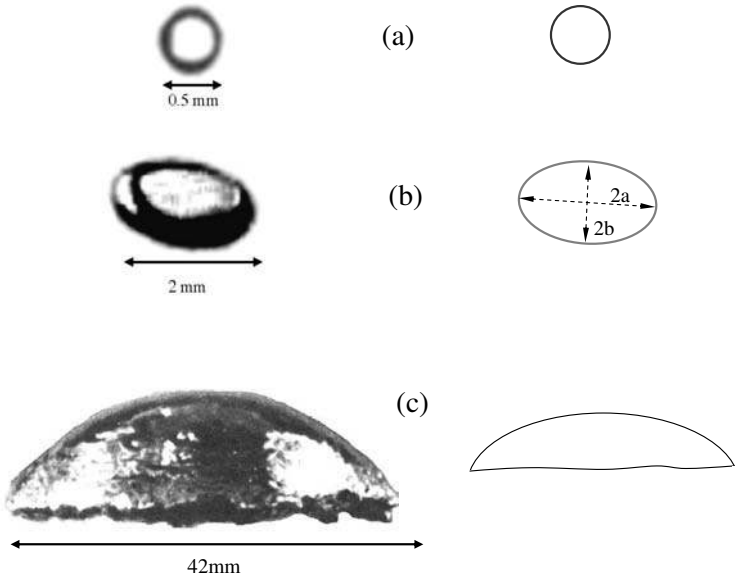

Figure 3.2: Some typical examples of the shape of a bubble rising in liquid: (a) spherical bubble rising in champagne at $Re \approx 25$ and $We \approx 0.02$ (Liger-Belair & Jeandet 2002); (b) ellipsoidal air bubble rising in water at $Re \approx 600$ and $We \approx 2$ (Tomiyama et al. 2002); (c) spherical-cap air bubble rising in water at $Re \approx 2500$ and $We \approx 50$ (Clift et al. 1978). The figures in the left column are given by Loth (2008a), the right column contains the sketches showing the interface outline.

and-aft symmetry. The "ellipsoidal bubbles" will be the objects of the current investigation.

Using Re, Eo and Mo, Clift et al. (1978) provided a shape regime for bubbles rising freely in an infinite fluid media, as shown in Figure 3.3. The arrow in the figure points to the parameter range of the present work. A very similar map was also provided by Bhaga & Weber (1981). Generally speaking, the following systematic trend can be noticed: bubbles are spherical at either low Re or low Eo; they are ellipsoidal at intermediate Re and Eo; spherical cap bubbles appear at high Re and high Eo.

For a small gas bubble in water, with a diameter less than 1 mm approximately, the surface tension force generally dominates and the bubble shape is spherical. Larger bubbles, with volumes greater than 3 cm^3 ($d_e > 18$ mm), are usually dominated by the inertial or buoyancy force with negligible effects of surface tension; therefore, the bubble shape tends to be a spherical cap.

For bubbles of intermediate size in water, both the surface tension force and the inertial force of the liquid can be important. Therefore, it is hard to predict the shape accurately.

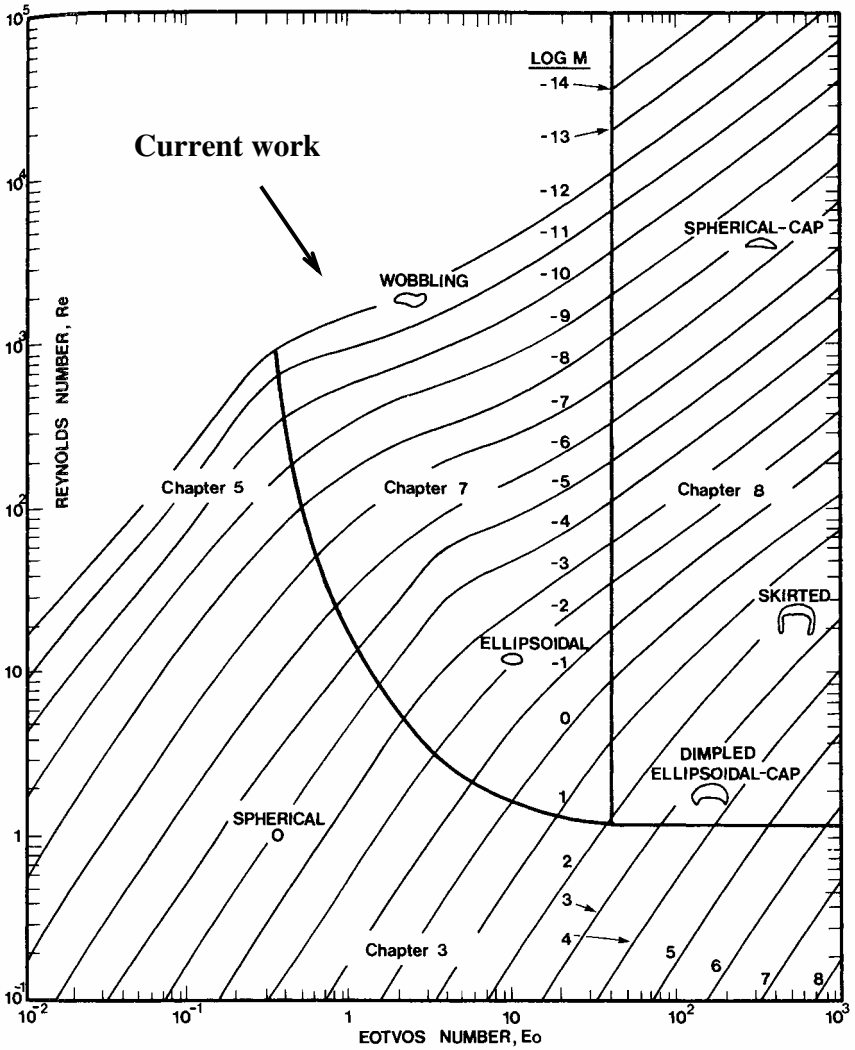

Figure 3.3: Shape regime for bubbles and drops in unhindered gravitational motion through liquids. The figure is taken from Clift et al. (1978)

The Weber number We can be used here since it shows the ratio of the two forces. For clean bubbles which deviate slightly from a spherical shape, Moore (1965) showed that the aspect ratio χ of a bubble can be approximated by the following equation (valid when $We \ll 1$.)

$$\chi = 1 + \frac{9}{64}\, We + o(We^2) \tag{3.8}$$

where $\chi = 2a/2b$ is the ratio of the cross-stream axis to the parallel axis of the oblate spheroid, as shown in Figure 3.2 b.

For a bubble with $We \sim 1$, Moore (1965) gave the following equation

$$We(\chi) = 4\chi^{4/3}(\chi^3 + \chi - 2)[\chi^2 \sec^{-1}\chi - (\chi^2 - 1)^{1/2}]^2(\chi^2 - 1)^{-3} \tag{3.9}$$

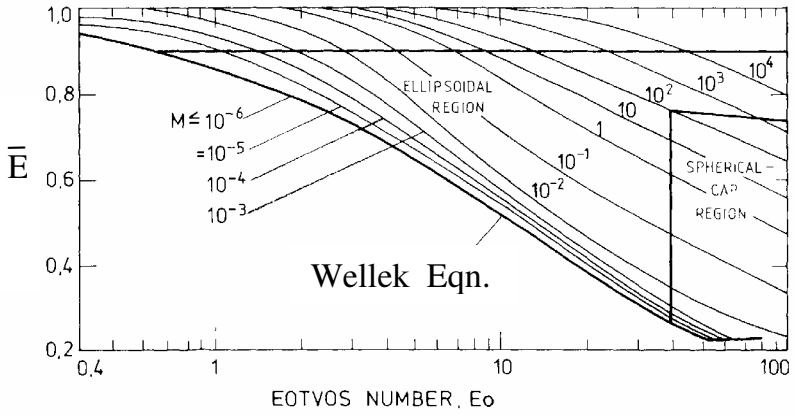

Figure 3.4: Correlation for the parameter $\overline{E}$ of bubbles in contaminated liquids, The equation (3.8) is also shown here. The figure is taken from Clift et al. (1978) and "M" here refers to Mo number.

which is derived by assuming that the bubble is still symmetric with respect to a horizontal plane through the bubble center. In practice, as the deviation from a spherical shape increases, the assumption of the symmetry becomes less and less plausible. It is shown that equation (3.9) works well as long as $\chi < 2$, see Moore (1965) and Duineveld (1995).

It becomes more difficult to predict the bubble shape theoretically when the deviation from the spherical shape increases. Based on experimental results, Wellek et al. (1966) gave the following correlation between a parameter $\overline{E}$ and the Eo number of a bubble

$$\overline{E} = 1/(1 + 0.163Eo^{0.757}) \qquad Eo < 40, Mo < 10^{-6} \tag{3.10}$$

where $\overline{E}$ is defined as the ratio of the maximum vertical dimension to the maximum horizontal dimension of the bubble. $\overline{E}$ can be considered as the reciprocal of χ in equation (3.8). Note that all their experiments are carried out in transparent liquids, and no experimental result in liquid metal was acquired by Wellek et al. (1966). Later, Clift et al. (1978) reviewed earlier investigations concerning the bubble shape and plotted the results as in Figure 3.4. The following tendency can be found in Figure 3.4: in the same liquid, the deformation of the bubble shape increases as Eo becomes larger; whereas for the same Eo, the deformation increases as the Mo number of the liquid decreases.

Recently, Loth (2008a,b) suggested to correlate the parameter $\overline{E}$ to the bubble Weber number, since We represents the force ratio which directly controls the deformation of the bubble shape. His summary of earlier experimental data is displayed in Figure 3.5, which shows that $\overline{E}$ is a unique function of We. The results from Wellek et al. (1966) are also included. For We between 1 and 10, which corresponds to the regime of "ellipsoidal" bubbles,

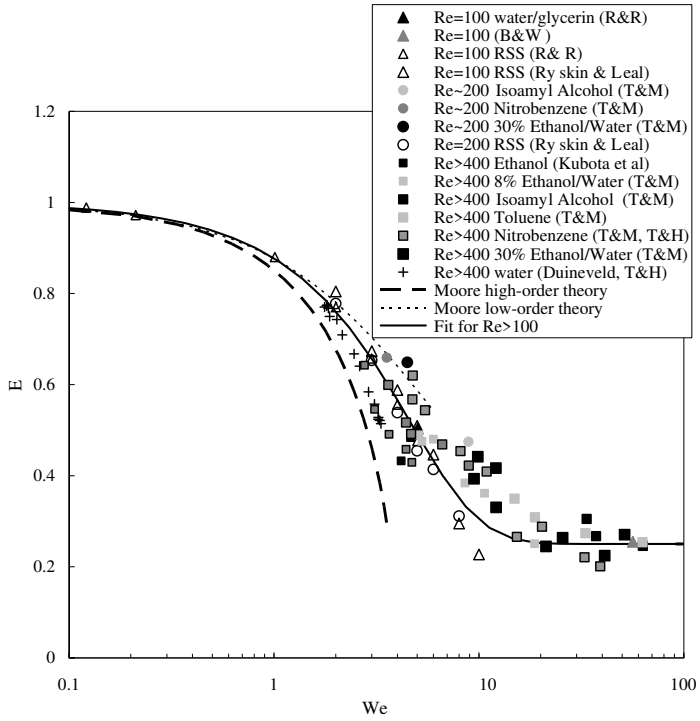

Figure 3.5: Correlation between $\overline{E}$ and bubble Weber number We in liquids. The figure is given by Loth (2008b) for bubbles with $Re > 100$, the parameter "E" in the figure is the same as $\overline{E}$ defined by Wellek et al. (1966).

the parameter $\overline{E}$ decreases very fast. For an even higher We number, the bubble shape tends to be a spherical-cap and the parameter $\overline{E}$ becomes constant around 0.25. Note that $\overline{E}$ in Figure 3.5 does not explicitly depend on the Mo numbers of the liquids.

3.2.2 Drag coefficient & terminal velocity

For a small bubble with $Re \ll 1$, the viscous force and the surface tension force dominate the flow, whereas the inertial force is negligible in comparison. Under this condition, analytical solutions can be derived for the drag coefficient. There are two well-known theories: the Hadamard-Rybczynski theory for clean bubbles with the boundary condition of zero-shear-stress at the gas-liquid interface

$$C_D = \frac{16}{Re} \qquad u_T = \frac{\rho g d_e^2}{12\mu} \tag{3.11}$$

and the Stokes theory for contaminated bubbles whose boundary condition is non-slip

$$C_D = \frac{24}{Re} \qquad u_T = \frac{\rho g d_e^2}{18\mu} \tag{3.12}$$

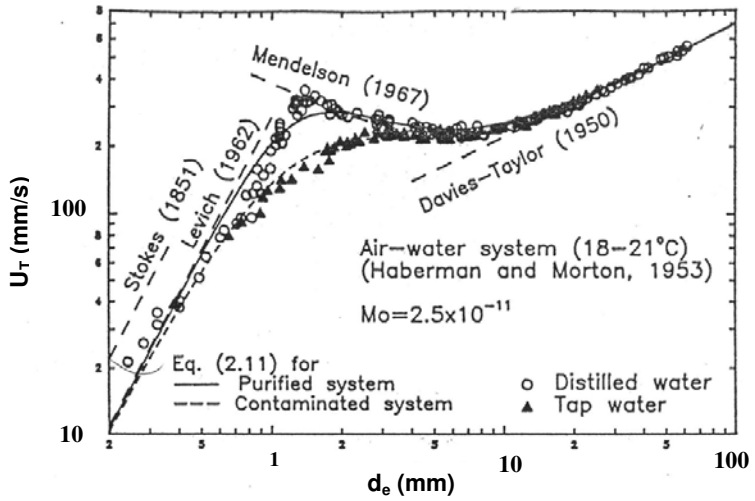

Figure 3.6: Terminal velocities of air bubbles in water. The figure is taken from Fan & Tsuchiya (1990).

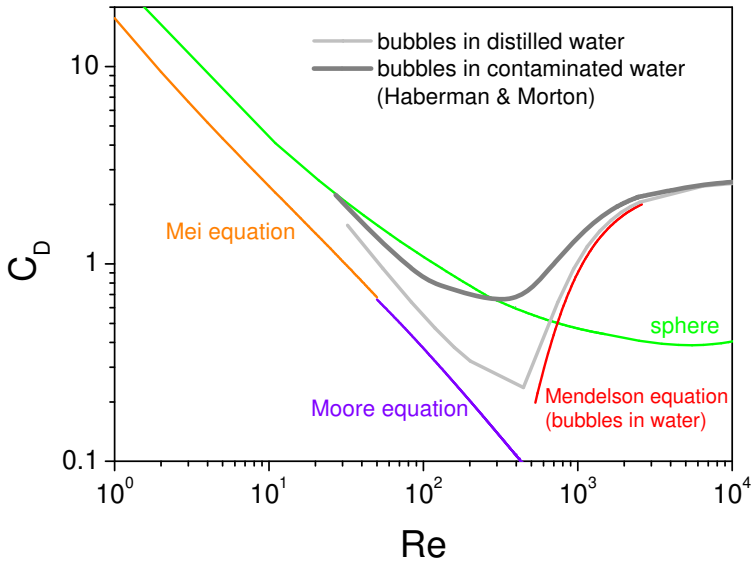

Figure 3.7: Curves of drag coefficient of air bubbles and a rigid sphere. The data of Haberman & Morton are provided by Fan & Tsuchiya (1990) in the form of correlation curves.

The change of the boundary conditions can be caused by impurities in the liquid, which will be discussed at the end of this section.

For bubbles in the range of $1 < Re < 50$, there seems to be no theoretical expression available. Mei et al. (1994) provided an empirical drag law for clean spherical bubbles

$$C_D = \frac{16}{Re}\left\{1 + \left[\frac{8}{Re} + \frac{1}{2}\left(1 + 3.315Re^{-1/2}\right)\right]\right\} \tag{3.13}$$

which is confirmed by Takagi & Matsumoto (1998).

For clean bubbles at a higher Re ($Re > 50$), Levich (1962) gave an asymptotic result for the drag coefficient in the simple form

$$C_D = \frac{48}{Re} \qquad u_T = \frac{\rho g d_e^2}{36\mu} \tag{3.14}$$

The equation (3.14) was later corrected by Moore (1965), who took into account a narrow wake flow containing vorticity. Moore (1965) showed

$$C_D = \frac{48}{Re}\left(1 - \frac{2.21}{Re^{1/2}}\right) + o\left(Re^{-11/6}\right) \tag{3.15}$$

For bubbles of even higher Re numbers ($Re \sim 10^3$) and still possessing an ellipsoidal form, the Mendelson equation (Mendelson 1967) gives a good prediction for the bubble velocities in pure liquids of low Mo numbers. The Mendelson equation is expressed as

$$u_T = \left(\frac{2\sigma}{\rho d_e} + \frac{g d_e}{2}\right)^{1/2} \tag{3.16}$$

The equation (3.16) consists of two competing terms, corresponding to the surface tension force and the inertial force (buoyancy force), respectively. It should be noted that the equation (3.16) is suitable for clean liquids.

Finally, for spherical-cap bubbles, Davis & Taylor (1950) obtained a theoretical result, which shows that the drag coefficient simply approaches to a constant

$$C_D = \frac{8}{3} \qquad \text{for} \quad We \to \infty,\ Re \to \infty \tag{3.17}$$

Discussions of such bubbles can be found in textbooks by Clift et al. (1978), Fan & Tsuchiya (1990) and Loth (2008a).

As an illustration, Figure 3.6 shows the terminal velocity of air bubbles in water. For small bubbles with d_e smaller than 1 mm, the terminal velocity increases with the size of the bubble. For bubbles of intermediate size with d_e from 1 mm to 10 mm approximately, the bubble velocity depends on the purity of the liquid.

Figure 3.7 shows the curves of the drag coefficient discussed above, as well as the experimental data obtained by Haberman & Morton (1953). For comparison, the standard drag coefficient curve of a rigid sphere is also included. The result of Levich (1962) is very close to that of Moore (1965); therefore, it is not shown here. Owing to flow separations behind bubbles, the curves show transitions at $Re \sim 500$. The flow separation leads to the increase of the drag at higher Re, which is well-predicted by the Mendelson equation. The drag coefficients of clean bubbles (equations 3.13 and 3.15) are lower than that of the rigid sphere, due to different boundary conditions at the interface.

The influence of impurities in the liquid is investigated for a long time. Reviews can be found for example by Clift et al. (1978), Fan & Tsuchiya (1990) and Magnaudet & Eames (2000). As a bubble rises up, the adsorbed impurities are swept downwards to the bubble rear part, which results in a gradient of concentration along the bubble interface. Furthermore, such a gradient leads to a surface tension force that retards the surface motion. As a result, the boundary condition of zero-shear-stress is replaced by non-slip condition, which increases the drag of the bubble.

3.2.3 Bubble trajectory

Previous studies show that gas bubbles exhibit different trajectories as they rise up in a liquid. A small bubble ($Re \ll 1$) always rises up rectilinearly. For ellipsoidal bubbles, path instabilities may occur. The trajectories then become non-rectilinear: zigzag, helical or rocking motions are typical examples in practice. Here, the term "zigzag" represents a side-to-side motion confined in one vertical plane, whereas the "rocking" refers to the irregular motion in a three-dimensional space. Such path instabilities are only observed from ellipsoidal bubbles. The trajectories of spherical-cap bubbles are rectilinear again.

Prosperetti (2004) referred to the failure of bubbles to follow a straight path as *Leonardo's paradox*, because Leonardo da Vinci's annotations are possibly the first scientific references to the phenomenon. After that, many investigations are carried out in order to achieve a comprehensive view of the phenomenon and to clarify the physical mechanism behind it; see for example reviews given by Fan & Tsuchiya (1990), Magnaudet & Eames (2000), de Vries (2001), Velhhuis (2007) and Loth (2008a). However, there are many unanswered questions. In this section, we will look through the literature concerning the following questions on the bubble trajectory.

When does the trajectory become non-rectilinear?

Earlier studies show unanimously that a bubble follows a rectilinear path if its size is small. However, different viewpoints exist concerning the threshold above which the path instability may occur. For instance, Haberman & Morton (1954) observed that the path is straight when $Re \lesssim 300$ in filtered liquids, such as water or oil. In another experiment of filtered water, Saffman (1956) reported that bubbles keep the rectilinear path if $d_e < 1.4$ mm. He also pointed out that the bubble wake must have changed as the path instability occurs, because the C_D of the bubble starts to increase after the path becomes non-rectilinear. The critical Reynolds number corresponding to the transition was $Re_{cr} = 400$. Aybers & Tapucu (1969a,b) showed that, for a bubble with $d_e = 1.31$ mm, the trajectory is rectilinear in

water at $Re = 408$, whereas the trajectory becomes helical when $Re = 725$. Additionally, they found that the rectilinear motion is not peculiar to spherical bubbles; instead, a bubble trajectory can be rectilinear at $\chi = 1.3$. They concluded that a path instability occurs at $Re_{cr} = 565$, which corresponds to $d_e = 1.34$ mm in water. Note that the experiments were carried out at different water temperatures.

Since the boundary conditions of small bubbles are very sensitive to the impurities in liquid, Hartunian & Sears (1957) gave two separate criteria for the onset of path instability. One criterion is $Re = 202$ for contaminated liquids, the other is a critical Weber number of $We_{cr} = 3.17$ for pure liquids. The latter criterion was improved by Tsuge & Hibino (1977), who pointed out that the We_{cr} is not unique but depends on the Mo of the liquids. They gave the following empirical function for pure liquids

$$Re_{cr} = 9.0Mo^{-0.173} \qquad We_{cr} = 21.5Re_{cr}^{-0.32} \tag{3.18}$$

For pure water of $Mo \approx 2.7 \times 10^{-11}$, equation (3.18) gives $Re_{cr} = 606$ and $We_{cr} = 2.77$. However, these values do not agree with later experimental results. For instance, in an experiment of "hyper clean" water, Duineveld (1995) showed the bubble trajectory keeps linear until $d_e = 1.82$ mm, which corresponds to $Re_{cr} = 660$ and $We_{cr} = 3.3$. This fact also indicates that the "distilled" water used by Saffman (1956) cannot be considered as clean, as discussed by Fan & Tsuchiya (1990). In another experiment, Maxworthy et al. (1996) showed $We_{cr} = 2.3$ for bubbles in clean water. They observed that We_{cr} increases when the Mo number increases, a tendency that indeed agrees with the prediction of Tsuge & Hibino (1977).

Recently, Zenit & Magnaudet (2008) investigated the path instability in five different pure liquids, whose Mo lies between 2.5×10^{-11} to 9.9×10^{-6}. Although Re_{cr} varies from 70 to 470 in these liquids, the critical aspect ratio χ changes only from 2.36 to 2.0. The results lead them to conclude that it is the shape of the bubble, rather than the Reynolds number, which is the dominant parameter to trigger the path instability. They pointed out that vorticity generated at the bubble interface is almost independent of Re but depends on χ directly. Therefore, they emphasized that the path instability is a direct consequence of the instability of the bubble wake, which further is a consequence of the vorticity generated at the bubble interface, which further again is directly related to χ.

Based on the above discussions, it is only possible to draw a few qualitative conclusions: the occurrence of a path transition depends on the dimension of the bubble and the physical properties of the liquid. In addition, impurities influence the transition, too. In pure liquids, the deformation of the bubble shape is usually considered as the threshold, either in terms

of We or simply χ. Furthermore, the critical We or χ decreases as the Mo decreases. In contaminated liquids, Re and d_e are usually used as criteria, as mentioned above.

What are the trajectories after the path instability?

For ellipsoidal bubbles, the trajectory can be either zigzag or helical. Haberman & Morton (1954) reported helical motion in the range of $300 < Re < 3000$ and rocking motion when $Re > 3000$ in distilled liquids. However, there are inconsistences in the literature. For instance, Saffman (1956) found the following tendency in his experiments

$1.4 < d_e < 2.0$	always zigzag
$2.0 < d_e < 4.6$	zigzag but can become helical

Table 3.1: Results from Saffman (1956)

For bubbles with $2.0 < d_e < 4.6$ mm, the path is zigzag when the disturbance is small during the injection process. However, if the bubble was deliberately disturbed, the zigzag path can transform into a spiral one. The radius of the spirals decreases slowly as the bubble size increases. The radius is about 1.5 mm as $d_e \sim 2$ mm, and the amplitude of a zigzag path is of the same magnitude. Furthermore, the transition cannot reverse; namely, the helical path can never change back into the zigzag one again. These results indicate that the zigzag motion occurs with a first instability, whereas the spiralling motion arises from another instability later than the zigzag one.

Aybers & Tapucu (1969a,b) obtained slightly different experimental results in tap water. The main conclusions are listed below

$1.34 < d_e < 2.00$	$(565 < Re < 880)$	always helical
$2.00 < d_e < 3.60$	$(880 < Re < 1350)$	zigzag but can become helical
$3.60 < d_e < 4.20$	$(1550 < Re < 1510)$	always zigzag
$d_e > 4.20$	$(Re > 1510)$	rocking

Table 3.2: Results from Aybers & Tapucu (1969a,b)

The bubble trajectory is helical when $1.34 < d_e < 2.00$mm, which is different from the results of Saffman (1956). Zigzag trajectories appear for larger bubbles with $2.00 < d_e < 4.20$mm. Similarly, they also observed that the zigzag path can transit into a helical one in the range of $2.0 < d_e < 3.6$. Rocking motions appear when $d_e > 4.2$mm.

Recently, Veldhuis et al. (2008) investigated the motion of bubbles with several values of d_e in clean water. Their results are shown in Table 3.3

d_e=3.0, 3.4	(Re=899, 973)	χ=2.2, 2.2	zigzag
d_e=3.6, 4.0, 4.5	(Re=1018, 1096, 1162);	χ=2.3, 2.4, 2.7	spiral
d_e=5.2	(Re=1305)	χ=2.8	chaotic

Table 3.3: Results from Veldhuis et al. (2008)

Note that the term "spiral" is used instead of "helical". For bubbles of $d_e = 3.6$ mm, 4.0 mm and 4.5 mm, the helical path becomes irregular as the d_e increases. They describe the path as spiral, flattened spiral and tilted flattened spiral, respectively. A chaotic trajectory is observed at $d_e = 5.2$ mm. They also show that the impurities in water clearly change the flow surrounding the bubble, which can result in different kinds of bubble shape oscillation and bubble wake.

Fan & Tsuchiya (1990) gave the following summary based on the studies of Garner & Hammerton (1954), Kubota et al. (1967), Tsuge & Hibino (1971) and Tsuge (1982). When a bubble rises in a liquid containing impurities, the path is usually zigzag. However, in pure liquid, the path is helical if the bubble is small ($1.5 < d_e < 3 - 5$ mm in distilled water); otherwise, the path is zigzag when the bubble size is large ($3 - 5 < d_e < 10 - 15$ mm in distilled water).

It is difficult to conclude accurately which trajectory a bubble will follow as the bubble size increases. Generally, zigzag motions are observed in liquids containing impurities when the bubble size is moderate and large, see Saffman (1956), Aybers & Tapucu (1969a,b) and Fan & Tsuchiya (1990). In contrast, the helical motions are observed only under certain limited conditions, such as small bubbles or pure liquids, as shown in Fan & Tsuchiya (1990) and Veldhuis et al. (2008). Another possibility to achieve a helical trajectory is via a later instability from a zigzag path, see Saffman (1956), Aybers & Tapucu (1969a,b). Indeed, the transition from a zigzag to a helical path is reproduced in recently numerical and experimental investigations, for example by Ellingsen & Risso (2001), Mougin & Magnaudet (2002), Shew et al. (2006) and Shew & Pinton (2006). It is worth to point out that the transition of this kind is only observed in pure liquids within a small range of d_e ($2.24 < d_e < 2.5$ mm) and all the above studies emphasize the purity of the water.

Saffman (1956) showed that the frequency of a zigzag motion is about 7 per second (7 Hz), whereas the frequency is about 5 revolutions per second (5 Hz) for spiraling motion. Both frequencies do not depend on the bubble size in his experiment. Tsuge & Hibino (1977) found that the frequencies of the motion do not change distinctively in purified liquids, and the frequencies stay within the range from 6.2 Hz to 8.3 Hz. In contaminated liquids, however, the frequency decreases monotonically from 7.7 Hz to 4 Hz as d_e increases from 2 to 8.5 mm. Specifically, Ellingsen & Risso (2001) investigated the non-rectilinear motion of a bubble with $d_e = 2.5$ mm in water. They found that both the vertical and the horizontal component of the bubble velocity oscillate periodically. The vertical velocity oscillates at twice the frequency of the horizontal velocity. Furthermore, the oscillation amplitude of the vertical velocity is much weaker compared to that in the horizontal direction. The frequency of the path oscillation is about 6.2 Hz in their experiments. The results are very close to

those of Duineveld (1995) in hyper-purified water, where the frequencies of the path are 6.4 Hz for a bubble with $d_e = 2.3$ mm and 7 Hz for a bubble with $d_e = 2.68$ mm. Veldhuis et al. (2008) reported the path frequency of different non-rectilinear motions in clean water. It is shown that the frequencies of smaller bubbles are higher than the larger bubble with rocking motion. The details are shown in the following table

d_e (mm)	3.0	3.4	3.6	4.0	4.5	5.2
f (Hz)	6.7	7.0	5.5	6.5	6.5	5.2

Table 3.4: Results from Veldhuis et al. (2008)

In summary, the above investigations give comparable results when the liquid is clean. The frequency of the motion is about 6 to 7Hz. For contaminated liquids, the frequency of the path decreases as the bubble becomes larger, as shown in Tsuge & Hibino (1977).

Why does the trajectory become non-rectilinear?

Saffman (1956) probably is one of the earliest who pointed out the importance of the bubble wake. He considered that the zigzag motion is caused by the interaction of an oscillating wake or a periodic discharge of vorticity behind the bubble. He also saw a similarity between a falling leaf and a zigzag rising bubble, although he admited that there is a different character, too. The leaf glides through the air with its velocity in the plane of the leaf, whereas a bubble moves perpendicular to its equatorial plane.

Later on, the importance of the wake was verified by other investigations. The review of Magnaudet & Eames (2000) show that there are strong supports that the path instability is intimately coupled to the instability of the wake. Since the boundary condition of a small contaminated bubble tends to behave like a solid sphere, it is helpful to look through some main conclusions concerning the wake behind a rigid sphere, too. The wake of a sphere firstly becomes non-axisymmetric at $Re_{cr1} \sim 210$, when two vortex filaments appear and the flow remains steady. A second instability occurs at $Re_{cr2} \sim 280$, after which the flow becomes non-steady and hairpin-like vortices are shed. Similar flow structures are observed in a bubble wake, too. Using dye visualizations, Lunde & Perkins (1997) displayed that the wake of a spiralling bubble is continuous; specifically, the wake consists of a continuous pair of helical vortex filaments attached to the bubble. In contrast, the wakes of zigzag and rocking bubbles are intermittent, and they are composed of alternately shed hairpin vortices. A snapshot of the wake structure of a rocking bubble is shown in Figure (3.8), together with a schematic illustration given by Brücker (1999). Brücker measured the wake of ellipsoidal bubbles with $4 < d_e < 8$ mm by PIV and achieved similar conclusions. A bubble rising in a

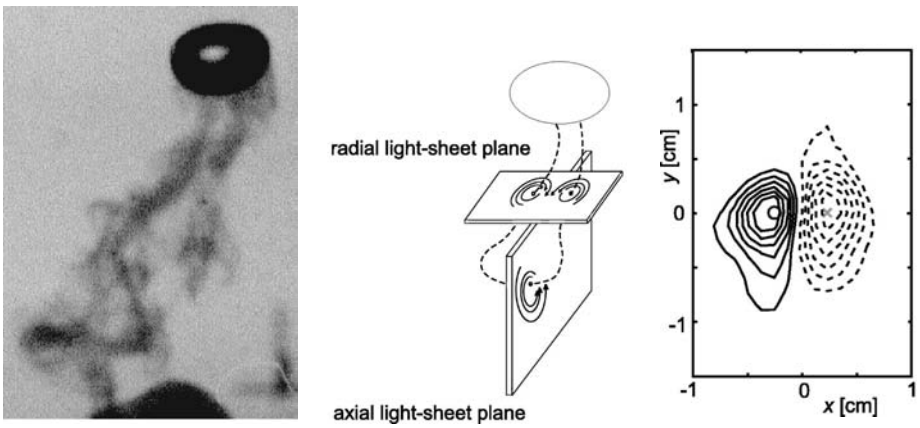

(a) (b) (c)

Figure 3.8: The wake structure behind a rocking bubble: (a) flow visualization by Lunde & Perkins (1997); (b) sketch of the hairpin vortex; (c) regions of concentrated streamwise vorticity in the radial light-sheet plane measured by PIV. The sub-figures (b) and (c) are taken from Brücker (1999).

helical trajectory shows a steady wake, which consists of a pair of counter-rotating vortices that attached to the bubble (for bubbles with $d_e \leq 4.0$ mm in his experiments). Furthermore, from the view of an observer moving with bubble, the wake looks like a pair of streamwise vortex filaments, which wound in a helical path and twisted around each other during one revolution of the bubble. However, for bubbles with zigzag or rocking trajectories, Brücker (1999) observed that hairpin-like vortices with alternately changed directions are generated and discharged regularly. Figure (3.8c) shows an example of the cross-section of the vortices.

Using Schlieren optics, Veldhuis et al. (2008) displayed different wake structures behind a helical and a zigzag rising bubble, respectively. Two typical examples are given in Figure 3.9, which shows a pair of continuous vortex filaments trailing behind a helical rising bubble, as well as hairpin-like vortices that are shed intermittently behind a zigzag rising bubble. The pictures verify that the wake of a bubble is directly coupled to the trajectory. Owing to the negligible mass, a bubble can be directly influenced by the force arising from the flow in the wake. It is shown that the lateral motion of a bubble is always normal to the plane which contains the two vortex filaments of the near wake, due to a lift force coming from the asymmetry of the two vortex filaments. Concerning a bubble with a zigzag path in contaminated liquids, it is also shown that the frequency of the vortex shedding behind the bubble is twice the frequency of the zigzag path.

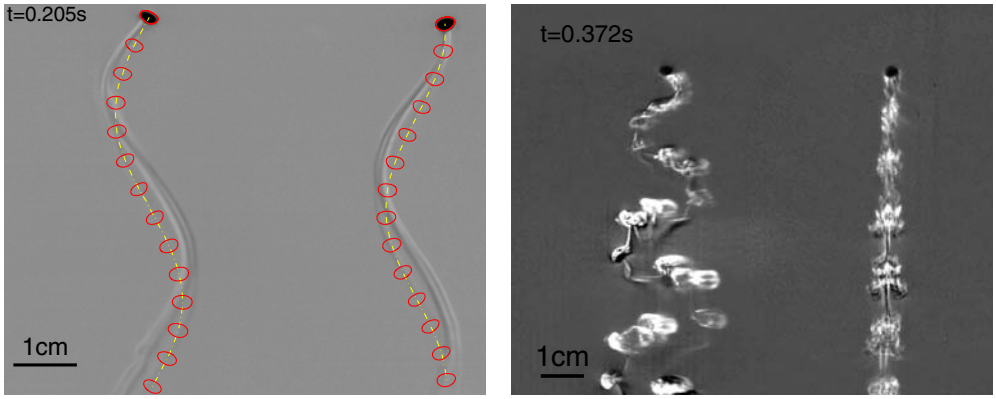

(a) (b)

Figure 3.9: The wake structure behind rising bubbles: (a) a helical rising bubble ($d_e = 2.2$ mm) in pure water; (b) a zigzag rising bubble ($d_e = 3.0$ mm) in tap water. Each figure shows the same rising bubble but at different projections simultaneously. The figures are taken from Veldhuis et al. (2008)

3.2.4 Bubble motion in liquid metals

The aforementioned results are all obtained in transparent liquids, where the flow can be measured by optical methods. The investigations are rare concerning the bubble motion in liquid metals. The motion of argon bubbles rising in mercury was studied by Schwerdtfeger (1968) using an ultrasonic instrument. It was shown that the terminal velocities of bubbles in mercury are slightly smaller than those in water. The data of Schwerdtfeger (1968) fit well with equation (3.16) derived by Mendelson (1967). Mori et al. (1977) investigated the influence of a horizontal static magnetic field on the motion of a single bubble in mercury. They used multi-wire sensors to measure the velocities of the rising bubble u_T, as well as the inclination angles of the bubble trajectory α. The results show that the horizontal magnetic field influences the bubble motion in different ways depending on the size of the bubble. Small bubbles with $d_e \sim 2$ mm follow helical trajectories when $B = 0$. The inclination angle α is monotonically decreased when B increases and the bubble rises up rectilinearly at $B = 1.5$ T. In parallel, the bubble velocity u_T is first increased when $B = 0.5$ T and $B = 1.0$ T, whereas u_T becomes clearly decreased when B is further increased to 1.5 T. The changes of u_T are attributed to the modification of the bubble trajectory by the magnetic field. Larger bubbles with $d_e \sim 6$ mm exhibit shapes of spherical-cap and rise up rectilinearly when $B = 0$. For such bubbles, the magnetic field decreases u_T monotonically in the range of $0 < B < 1.5$ T. The drag coefficient C_D of such a bubble is similar to that of a solid sphere in a transverse magnetic field, see Lielausis (1975). The experiment of Mori et al. (1977) seems to be the

only work that can be found in the literature, concerning the influence of a static magnetic field on the motion of single bubbles.

Summarizing chapter 3.2, we looked through the literature concerning the motion of a single bubble in stagnant liquids with the focus on the shape, the velocity and the trajectory of a bubble. In general, a bubble keeps the spherical shape and rises up with a straight path if its size is small. As the size increases, the bubble shapes change to ellipsoidal ones. There are different theories and empirical correlations to predict the rising velocity depending on different ranges of parameters. An ellipsoidal bubble has non-rectilinear trajectories, which can be helical, zigzag or rocking. The various kinds of bubble motion are directly related to the wake flow behind the bubbles. Up to now, the studies of bubble motion in the MHD context are rare in the literature. However, the investigation of the single bubble motion in liquid metals is necessary when we wish to have a better understanding, for instance, concerning the bubble-driven flows in a ladle refinement process.

In the following sections, we will present experimental results concerning a single bubble rising in GaInSn. The flow will be exposed to a vertical (longitudinal) as well as a horizontal (transverse) DC field, respectively.

3.3 Experimental setup

We carried out the experiment in an open cylindrical container of Perspex, as shown in Figure 3.10. The cylinder had a diameter of 90 mm and was filled with GaInSn to a height of $H = 220$ mm. The origin of the coordinate system was located at the center of the cylinder bottom, with the z-axis aligned with the cylinder centerline. The cylinder is inside a pair of copper coils with a Helmholtz configuration. The diameters of the coils were 210 mm and the distance between them was 150 mm. This configuration provided a homogeneous DC magnetic field over the fluid volume in the vertical direction. A DC current was supplied to the coils, which gave the maximum magnetic induction of 0.3 T at 1600 A. A horizontal magnetic field can be achieved by turning the coil system by 90°. Argon bubbles were injected into the liquid by a single nozzle. The inner diameter of the nozzle can be varied from 0.3 to 5 mm. The nozzle outlet was located at the center of the cylinder cross-section and 10 mm above the cylinder bottom. A mass flow controller (MKS 1359C, MKS Instruments) was used to regulate the gas flow rate Q_G, which was between 0.002 and 0.02 cm^3/s. We obtained single isolated bubbles with d_e between 4 mm and 8.5 mm in the experiment. The ratio between the diameter of the cylinder to the diameter of the bubble was larger than 10. Therefore, we can neglect the influence of wall confinement and consider the bubbles as rising

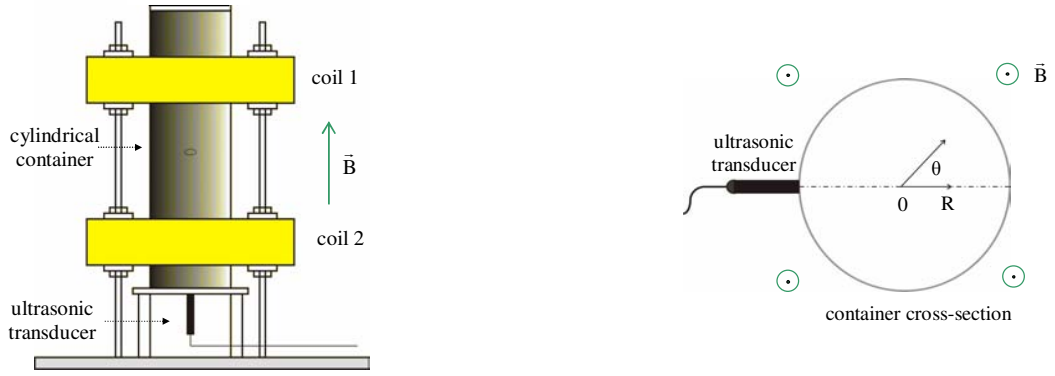

(a) (b)

Figure 3.10: Sketch of the experimental arrangement. (a) measurement of the vertical velocity along container axis (b) measurement of the radial velocity along the container diameter.

up in an infinite domain, see Clift et al. (1978). The time intervals between two consecutive bubbles were between 5 and 15 s. The measurements using the DOP2000 showed that the wake of a bubble decayed completely within this time. Therefore, the influence caused by the preceding bubble on the oncoming one can be neglected. In the experiment, we measured the vertical component velocity along the cylinder axis, as well as radial component velocity along the cylinder diameter by arranging the transducer at the cylinder bottom and the sidewall, respectively. The sketches of the experiment configuration are shown in Figure 3.10(a) and 3.10(b).

3.4 Experimental results

3.4.1 Flow without a magnetic field

At the beginning, we investigate the bubble motion in GaInSn at $B = 0$. The obtained results will serve as a basis for further discussions when a magnetic field is applied. The equivalent diameters of the bubbles are a few millimeters in the experiments. We were not able to directly measure the profiles of the bubble shape because of the opaqueness. Therefore, the bubble shape was estimated based on equation (3.10). If we take the minimum and the maximum d_e in the experiment, we obtain:

$d_e = 4.3$ mm:	$Eo = 2.2$	$\overline{E} = 0.77$
$d_e = 7.5$ mm:	$Eo = 6.6$	$\overline{E} = 0.60$

Table 3.5: Deformations of the bubble shape

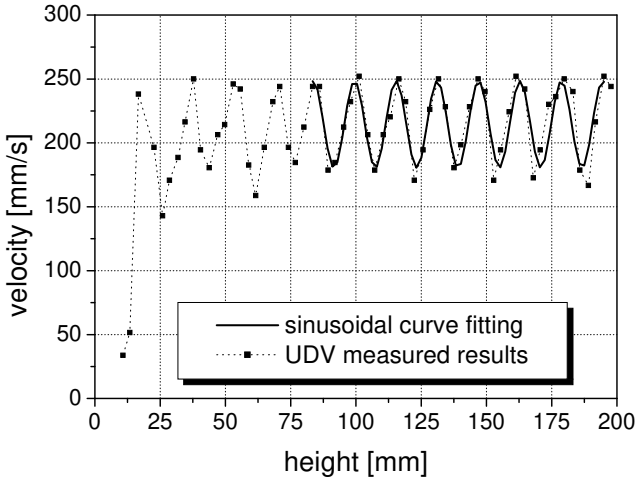

Figure 3.11: A typical example showing the evolution of the vertical velocity of a bubble with height. ($d_e = 4.6$ mm, $B = 0$)

In both cases the bubble shapes are ellipsoid.

Next, we investigate the velocities of the rising bubbles. Figure 3.11 shows a typical example of the vertical component of the bubble velocity along the height of the liquid column. As the bubble departs from the nozzle, it experiences a short period of acceleration, after which the bubble velocity starts to oscillate. Similar phenomena are also observed by other authors in transparent fluids, such as air-water and nitrogen-fluoroinert systems; see for example Ellingsen & Risso (2001), Marco et al. (2003), Mougin & Magnaudet (2002) and Magnaudet & Mougin (2007). It was shown that the velocity oscillations are related to the zigzag motion of the bubble. In the region between 100 and 200 mm, the velocity oscillation in Figure 3.11 appears to be regular and the mean velocity is constant. A similar tendency is found for other bubbles with different diameters in our experiments. In the following parts, quantities such as the bubble terminal velocity u_T and the oscillation frequency are determined in this parameter region.

For the analysis of the motion, we follow the procedure proposed by Ellingsen & Risso (2001) to fit the periodic velocity curve with a sine function (see also Figure 3.11)

$$u(z) = u_T + A \cdot \sin\left(\pi \frac{z - z_i}{\lambda}\right) \tag{3.19}$$

where A is the oscillation amplitude, z is the current vertical position, z_i is the initial position, and λ is the wavelength of the oscillation. Values of u_T and λ can be obtained by performing a least-square fitting of the experimental results. Ensemble averages of 20 bubbles are used to minimize the statistical error of the measurement.

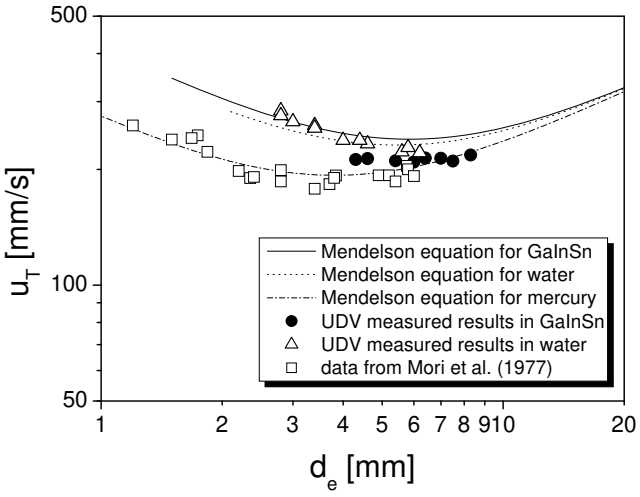

Figure 3.12: Bubble terminal velocity vs. bubble equivalent diameter in various liquids.

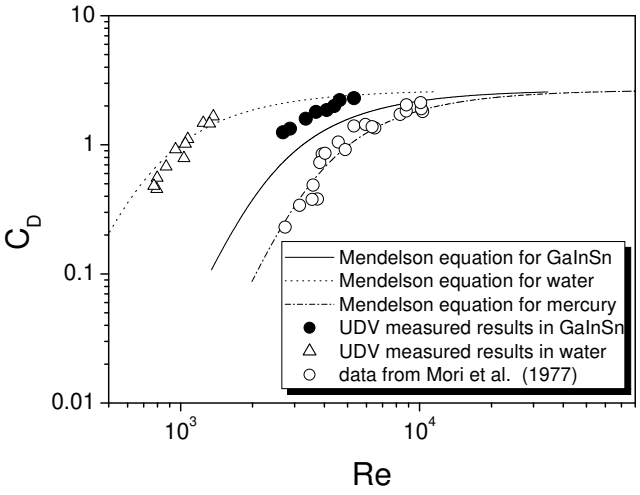

Figure 3.13: Bubble drag coefficient vs. bubble Reynolds number in various liquids.

The measured terminal velocities are presented in Figure 3.12 as a function of the bubble equivalent diameter. The data are compared with corresponding measurements in tap water, the results in mercury obtained by Mori et al. (1977), as well as the theoretical predictions according to equation (3.16) given by Mendelson (1967). The experimental data in tap water and mercury match equation (3.16) well, whereas a discrepancy can be observed in the case of GaInSn. This discrepancy can be attributed to the role of the impurities in the melt. In contrast to the noble metal mercury, the oxidation of the GaInSn alloy cannot be avoided with a reasonable effort in our experiment. The oxides decrease the surface tension of the melt, therefore, equation (3.16) gives an overestimation of the bubble velocity. Furthermore,

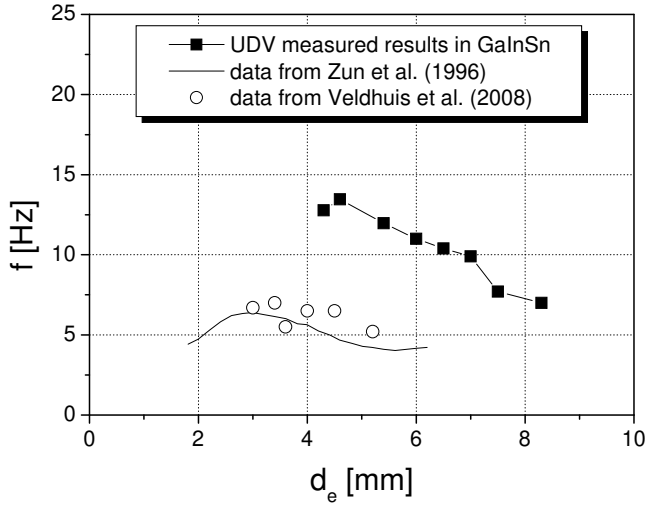

Figure 3.14: Bubble vertical velocity oscillation frequency vs. equivalent bubble diameter.

as a bubble rises up, impurities can be accumulated on the gas/liquid interface and change the boundary conditions, which result in a smaller rising velocity for the bubble as well, see Clift et al. (1978), Magnaudet & Eames (2000).

The discrepancy can be observed also in Figure 3.13, where the drag coefficient C_D is drawn as a function of the Reynolds number Re. These results are based on the data of the terminal velocity u_T by using equation (3.6). In Figure 3.13, the drag coefficients increase as the Re number increases, which indicates that the experiments were performed in the regime where flow separation occurred behind the bubbles, see Saffman (1956).

According to equation (3.19), we can determine the wavelength λ for the oscillation of the bubble vertical velocity. The corresponding frequency f_z of the oscillation is obtained as

$$f_z = \frac{u_T}{\lambda} \tag{3.20}$$

The results are shown in Figure 3.14, where the frequency of the vertical velocity decreases almost monotonically as the bubble size increases. For comparison, the figure contains the frequencies of the trajectory variation, which are obtained in water by Zun & Groselj (1996) and Veldhuis et al. (2008). It is shown that the frequency of the vertical velocity is approximately twice that of the trajectory variation. This agrees with the results of Ellingsen & Risso (2001) and Fan & Tsuchiya (1990), who showed that the oscillation of bubble motion in the vertical plane is about twice that in the horizontal plane. It should be noted that the experiments were carried out in water and GaInSn, which have different Morton numbers and Reynolds numbers, respectively. This can explain the differences in the comparison.

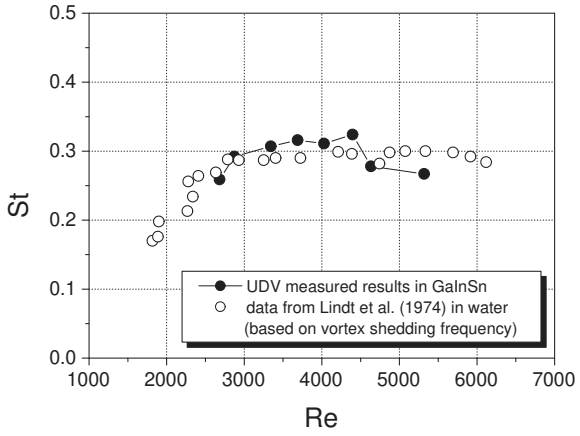

Figure 3.15: Bubble Strouhal number vs. Reynolds number.

The oscillation of the vertical velocity of a bubble is also analyzed in terms of the Strouhal number

$$St = \frac{f_z \cdot d_e}{u_T} \tag{3.21}$$

Figure 3.15 shows the Strouhal number St as a function of the bubble Reynolds number Re. The results are compared with data of Lindt (1972), who provided a $St-Re$ relationship for air bubbles in tap water. In his work, St is determined by counting the vortices shedding from the bubble on stroboscopic flash photographs. It turns out that the St increases when Re increases up to $Re < 3000$; afterwards, St becomes almost constant. Our results agree with those of Lindt (1972) fairly well. This indicates that the frequency of the vertical velocity oscillation is comparable to the frequency of vortex shedding. In other words, the frequency of the vortex shedding is twice that of the variation in the trajectory. As indicated in Figure 3.9, a zigzag bubble indeed sheds hairpin-like vortices twice during one period of the trajectory variation.

Several investigations showed that the oscillation of the bubble vertical velocity is directly related to the zigzag trajectory. Namely, the velocity oscillates periodically when the trajectory is zigzag, whereas the velocity is almost steady when the trajectory is helical. For instance, Mougin & Magnaudet (2006) simulated the motion of a rising bubble with its zigzag path changing to a helical one. The main results are shown in Figure 3.16. When the trajectory is zigzag, the vertical velocity of the bubble oscillates regularly. In comparison, the velocity of the y_a component oscillates at half the frequency of the vertical velocity and with a larger amplitude, as can be seen in Figure 3.16(b). When the bubble trajectory changes

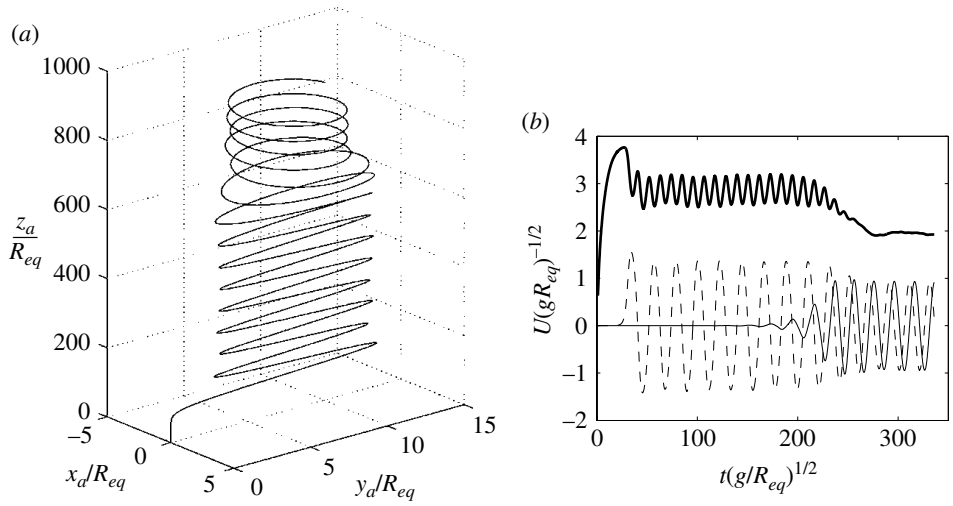

Figure 3.16: Path characteristics of a rising bubble: (a) trajectory of rising bubble; (b) evolution of vertical (thick line) and horizontal velocity components of the rising bubble, (dashed line represents y_a component velocity and thin line represent x_a component velocity). The figures are taken from Mougin & Magnaudet (2006).

into a helical one, the magnitude of the vertical velocity decreases. Afterwards, the vertical velocity becomes almost steady. At the same time, the velocity of the x_a component grows until it is comparable to that of the y_a component. A very similar result is also obtained by Shew & Pinton (2006) and Shew et al. (2006) in experiments. Therefore, if we recall the distinct oscillations of the bubble vertical velocity in Figure 3.11, Figure 3.14 and Figure 3.15, we can assume that bubbles follow zigzag trajectories in the current experiment.

In summary, we investigated the motion of a single bubble in liquid metals without a magnetic field in this section. In the current work, we expect ellipsoidal bubbles with zigzag trajectories. This is also supported by the fact that bubbles with helical trajectories are mostly found in purified systems when d_e is small, see for example Fan & Tsuchiya (1990). In the next section, we will apply a static magnetic field on the flow and observe how the bubble motion and the bubble wake can be influenced.

3.4.2 Flow in a vertical magnetic field

The influence of a steady magnetic field on the flows of electrically conducting liquids are investigated for long time; see for example textbooks or reviews given by Shercliff (1965), Lielausis (1975), Moreau (1990), Davidson (2001), Müller & Bühler (2001) and Knaepen & Moreau (2008). The motion of vortices in a static magnetic field was studied by Davidson

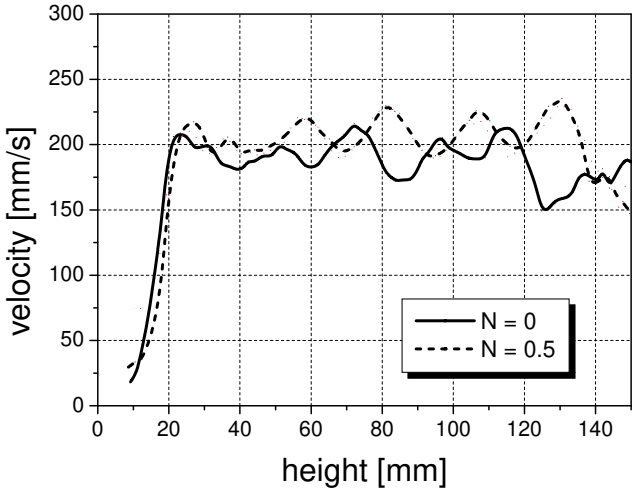

Figure 3.17: One typical example displaying the influence of a DC longitudinal magnetic field on bubble velocity.

(1995) and Sreenivasan & Alboussiere (2002). A static magnetic field suppresses the flow in a non-isotopic way, where vortices with the axis normal to the field lines are effectively damped, whereas vortices parallel to the field lines experience weak damping effects, or they can be free from the magnetic damping under certain conditions. As a result, the flow field becomes anisotropic; namely, the flow tends to become two-dimensional and independent on the coordinate parallel to the field lines.

In this section, we study the influence of a vertical magnetic field on the motion of a bubble and the bubble-induced flow. Figure 3.17 compares the ensemble-averaged vertical velocity of 20 rising bubbles at $B = 0.17$ T ($N = 0.5$) and the data of $B = 0$. The curves come from an ensemble average of the results of 10 bubbles. The mean value of the terminal velocity is slightly higher in the magnetic field than that with $B = 0$. For detailed discussions, we use the interaction number N defined in equation (1.10), where the characteristic length scale, the density and the velocity are based on the bubble equivalent diameter d_e, the density ρ_l of GaInSn and the terminal rising velocity u_T of the bubbles, respectively.

The dependence of the bubble drag coefficient on the interaction number is shown in Figure 3.18, where d_e is normalized as the Eötvös number Eo, and the drag coefficient is normalized with the original values of $C_D(N = 0)$ that are obtained at $B = 0$. Two different tendencies can be found in Figure 3.18: C_D of small bubbles ($Eo \leq 2.5$) decreases slightly and then starts to increase when N becomes larger; whereas C_D of larger bubbles ($Eo \geq 3.4$) decreases monotonically as N increases.

No literature seems available concerning the influence of an aligned DC magnetic field

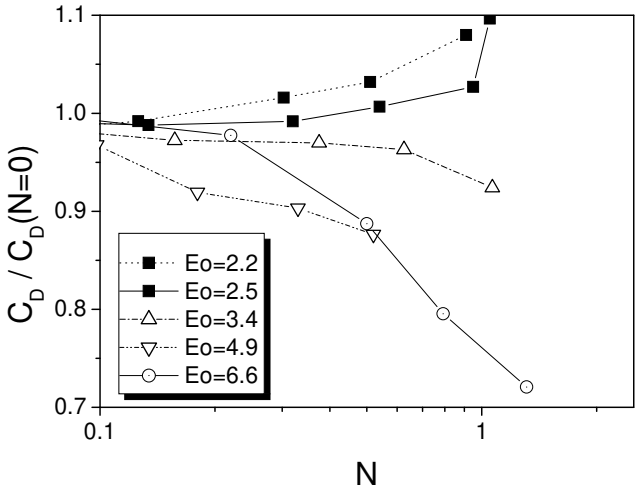

Figure 3.18: Drag coefficient vs. interaction number.

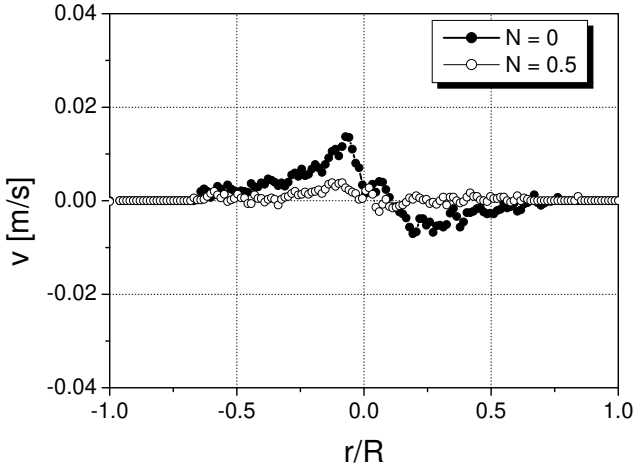

Figure 3.19: A typical snapshot of the radial velocity distributions with and without a DC longitudinal magnetic field. The profiles were measured at $t = 0.4s$ after the passage of the bubble.

on the bubble motion. We can only find investigations concerning the flow around a fixed sphere in an aligned magnetic field, for example Maxworthy (1962, 1968) and Yonas (1967). They studied the drag coefficients of spheres at large interaction numbers and high Reynolds numbers ($0 < N < 80$, $10^4 < Re < 25 \times 10^4$). Their results show a monotonic increase of C_D with the growing magnetic induction. For the current results in Figure 3.18, the increased C_D of small bubbles is similar to that of a sphere in a magnetic field. Namely, C_D increases if N is sufficiently large. For larger bubbles, the decreased C_D (increased u_T) probably can be attributed to the confinement of the bubble lateral motion by the longitudinal magnetic

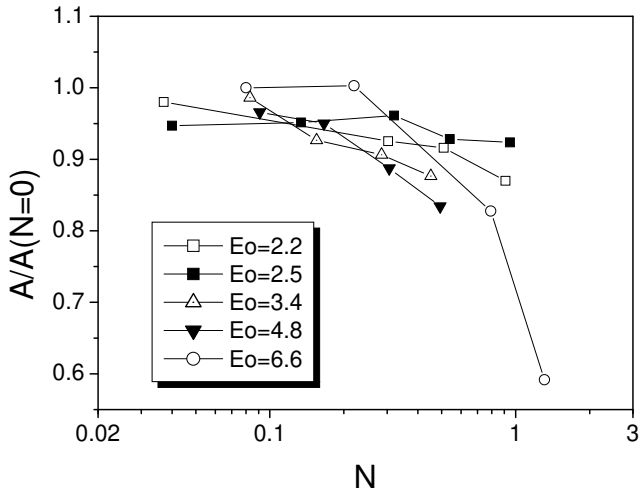

Figure 3.20: Velocity oscillation amplitude vs. interaction number.

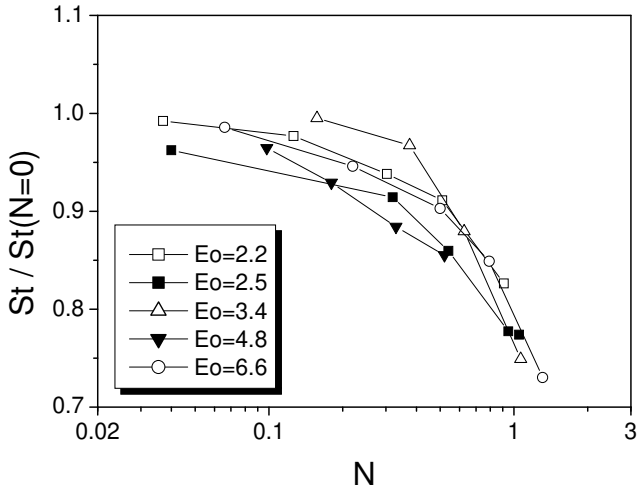

Figure 3.21: Bubble Strouhal number vs. interaction number.

field, as discussed by Mori et al. (1977). In fact, when the trajectory is zigzag, the bubble is accompanied with horizontal motions, too. A direct measurement of the lateral velocity of the bubble cannot be achieved by the single transducer displayed in Figure 3.10(b). In fact, the transducer measures the lateral component of the liquid velocity which is induced by a rising bubble. The velocity of the induced liquid flow can be considered as a measure for the lateral motion of the rising bubble, due to the direct link between them.

Figure 3.19 shows the influence of the vertical magnetic field on the radial velocity of the liquid motion. The profiles were obtained along the diameter of the cylindrical vessel at a position of $z = 100$ mm, and recorded 0.4 s later when the bubble passed the ultrasound

beam. The radial velocity at $B = 0.17$ T is up to 5 times lower than the velocity at $B = 0$. A similar effect is also observed in bubble clouds in a vertical channel flow, where bubbles are injected through an orifice positioned in the center of the channel cross-section. Eckert et al. (2000a,b) showed that the turbulent bubble dispersion in the lateral direction is significantly reduced by a longitudinal magnetic field, which results in a narrow peak in the distribution of void fraction above the injector. It can be expected that the longitudinal field confined the single bubble motion in the current experiment, too.

The increase of N decreases the amplitude as well as the frequency of the velocity oscillation of the bubbles, as shown in Figure 3.20 and Figure 3.21, respectively. The frequency of the bubble vertical velocity is normalized into the Strouhal number in the latter figure. A similar tendency concerning the frequency is observed by Lahjomri et al. (1993) in a flow around a cylinder, which is exposed to a static magnetic field aligned with the direction of the mean flow. The reduced frequency of the cylinder wake is attributed to the Joule effect, which reduces the generation of vorticity from the cylinder surface. The magnetic field delays the growth of eddies on the cylinder surface, hence their detachment by the external flow. Therefore, the shedding frequency of vortices is lowered in their experiments.

Besides the velocity of a gas bubble, we measured the liquid velocity in the bubble wake. Figure 3.22 shows the snapshots of the wake profile when the bubble reaches $z = 130$ mm and $z = 170$ mm, respectively. In the original flows at $N = 0$, the profiles show distinct velocity variations behind the bubble, see for example the local velocity peaks at $z \approx 70$ mm and $z \approx 110$ mm in Figure 3.22(a). Such variations can be related to the vortex structures shown in Figure 3.9(b). In the original flow, the wake is not yet fully developed until the bubble reaches a height of $z \approx 70$ mm, because the liquid velocities below that height are small. In comparison, the longitudinal field smoothes the profiles of the liquid velocity behind the bubble, as shown in both snapshots. In other words, the magnetic field decreases the velocity variations and elongates the flow structures along the field lines. The fluid motion is damped in the region of near wake; in contrast, the flow is enhanced in the region of far wake ($z < 70$ mm in both figures).

Figure 3.23 compares the decaying processes of the bubble-induced fluid motion with and without the magnetic field. Two examples at $z = 66$ mm and $z = 100$ mm are chosen. The fluid velocities are normalized by the terminal velocity of the bubble u_T, and the time axes are normalized by the period of the bubble velocity oscillation $T = \lambda/u_T$. At the beginning, the liquid velocities are smaller in the magnetic field, whereas they decay slower and finally become larger than the velocities at $B = 0$. This phenomenon correspond to the results shown in Figure 3.22.

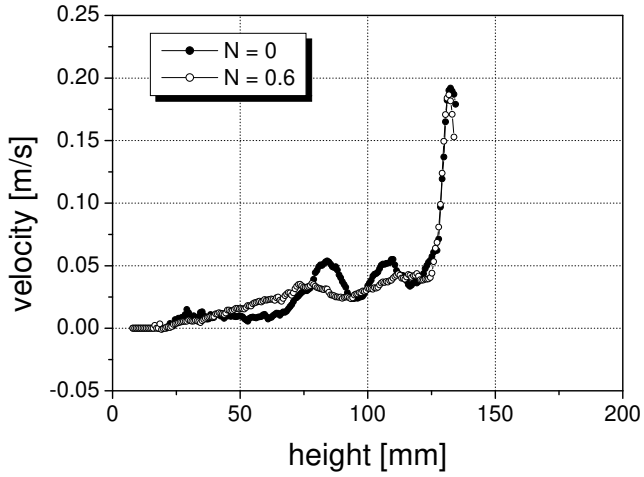

(a)

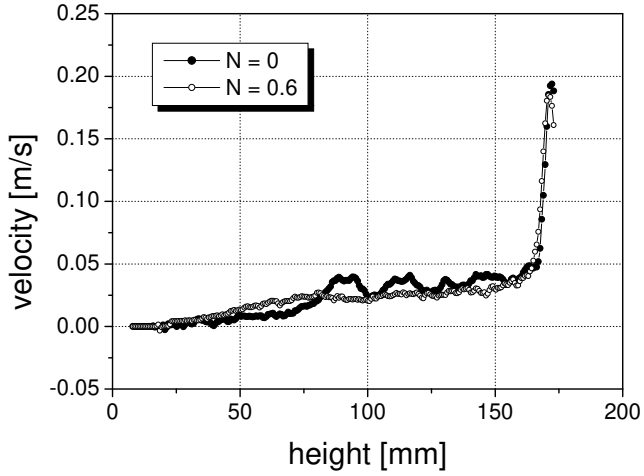

(b)

Figure 3.22: Two typical snapshots of the bubble wake velocity distribution along the ultrasound beam: (a) the bubble is 130 mm above the nozzle; (b) the bubble is 170 mm above the nozzle. The ultrasound beam coincides with the axis of the vessel as well as the trajectory centerline.

In the literature, it is shown that a bubble with a zigzag trajectory is accompanied with periodic oscillations in its vertical velocity and hairpin-like vortices shed behind. In the current experiment, we indeed found that the vertical velocities of the bubbles oscillate periodically and the profiles of the bubble wake contain large-scale structures corresponding to the hairpin vortices, too. These results agree with the visualization of a zigzag bubble in Figure 3.9(b) given by Veldhuis et al. (2008). The application of the vertical magnetic field smoothes the distribution of the liquid velocity in the vertical direction by spreading

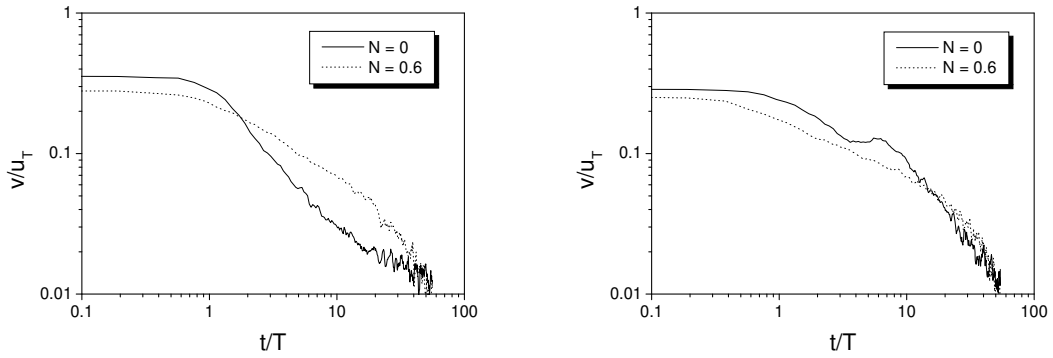

(a) (b)

Figure 3.23: Two typical examples showing the time series of the liquid velocity which are decaying with and without the longitudinal magnetic field. The fluid flow is induced by a bubble with $d_e = 7$ mm. (a) at the height of 66 mm above the nozzle; (b) at the height of 100 mm above the nozzle.

momentum along the field lines. Therefore, we obtained the uniform profiles of the liquid velocity in Figure 3.22.

3.4.3 Flow in a horizontal magnetic field

In this section, we investigate the flow in a horizontal magnetic field. The coils were turned by 90 ° to provide the transverse field. The experiment procedures were the same as those in the previous section. Figure 3.24 shows the influence of the transverse field on the bubble drag coefficients. For smaller bubbles with Eo at 2.7, 4.1 and 4.4 (d_e=4.8 mm, 5.9 mm and 6.1 mm), C_D mainly decreases in the range of $0.4 < N < 1.2$. However, for larger bubbles with Eo of 5.9, 6.4 and 6.9 (d_e=7.1 mm, 7.4 mm and 7.7 mm), the tendency is non-monotonic, C_D decreases first and starts to increase again when $N \gtrsim 1$.

The influence of a transverse magnetic field on bubble motion was investigated by Mori et al. (1977), who carried out the experiments in mercury in the range of $0.5 < B < 1.5$ T. The main results of Mori et al. (1977) are displayed as Figure 3.25(a). Since the physical properties of mercury and GaInSn are different, the results of Mori et al. (1977) are also re-plotted as Figure 3.25(b), where non-dimensional numbers are used. Besides, Table 3.6 shows a comparison between the two fluids. A bubble with $d_e = 5.9$ mm achieves very different We numbers and Re numbers in GaInSn and mercury, respectively. Therefore, we can expect different bubble shapes and bubble motion according to Figure 3.5 and Figure 3.7.

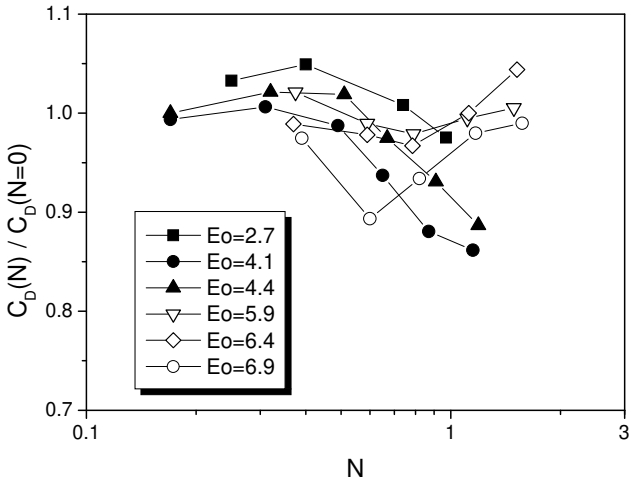

Figure 3.24: Normalized bubble drag coefficient vs. interaction number in a transverse magnetic field.

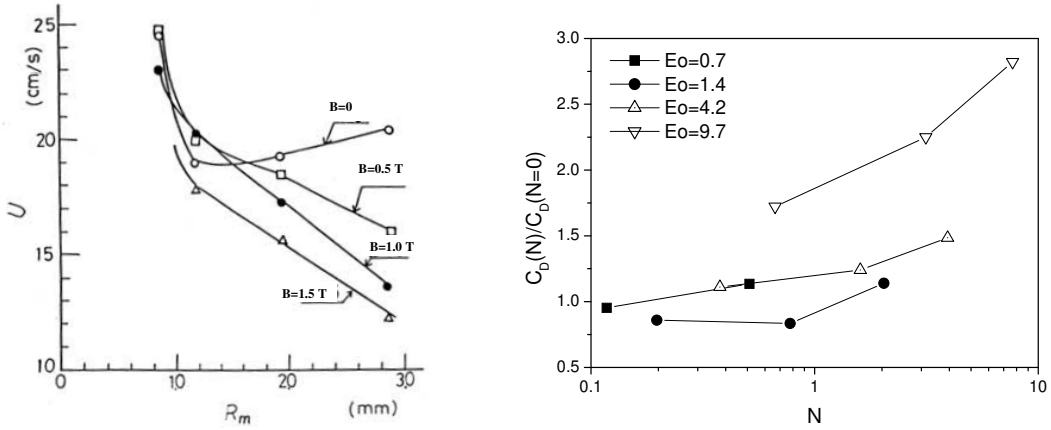

(a) (b)

Figure 3.25: Experimental results obtained by Mori et al. (1977) in mercury by a triple-wire sensor: (a) bubble rising velocity vs. equivalent bubble radius R_m at different magnetic inductions ($R_m = d_e/2$). The figure is given by Mori et al. (1977); (b) bubble drag coefficient vs. interaction number. The figure is re-plotted and based on the corresponding data provided on the left hand side.

	GaInSn	mercury
density ρ (kg m^{-3})	6361	13610
dynamic viscosity μ (kg m^{-1}s^{-1})	2.2×10^{-3}	1.53×10^{-3}
surface tension σ (N m^{-1})	0.533	0.460
electrical conductivity σ_e (Ω^{-1}m^{-1})	3.27×10^{6}	1.0×10^{6}
Morton number Mo	2.4×10^{-13}	3.6×10^{-14}
Eötvös number Eo	4.2	9.7
Weber number We	3.4	6.9
Reynolds number Re	3823	10384

Table 3.6: A comparison of the parameters between GaInSn and mercury. The non-dimensional parameters are estimated based on a bubble with $d_e = 5.8$mm.

Mori et al. (1977) showed that the magnetic field changes the bubble motion in different ways depending on the bubble size. A bubble with $d_e = 2.2$ mm ($Eo = 1.4$) follows a helical trajectory when $B = 0$. The inclination angle of the path decreases as B increases, and the bubbles rise up vertically at $B = 1.5$ T. As a result, the magnetic field decreases C_D of the bubble when $N \lesssim 1$; afterwards, C_D increases when $N \approx 2$, as shown in Figure 3.25. In contrast, a bubble with $d_e = 5.8$ mm ($Eo = 9.7$) has the shape of a spherical-cap and a rectilinear trajectory when $B = 0$. Mori et al. (1977) found that the magnetic field monotonically increases the C_D of the bubble. The tendency of C_D is similar to that of a fixed sphere in a transverse magnetic field, see Lielausis (1975). In summary, the results of Mori et al. (1977) indicate the following tendency. The transverse field tends to change a helical trajectory of a bubble into a rectilinear one, and the magnetic field decreases the C_D of the bubble during this time (namely, the field increases the vertical velocity of the bubble). After the trajectory becomes rectilinear, the increase of B leads to increased C_D of the bubble. In comparison, for a large bubble with a rectilinear trajectory originally, the increase of B simply leads to increased C_D monotonically.

Figure 3.25(b) shows that the transverse magnetic field changes remarkably the C_D of the large bubble ($d_e = 5.9$ mm, $Eo = 9.7$) in the range of $1 \lesssim N < 10$, whereas the modifications of C_D are less remarkable when $Eo \leq 4.2$ and $N < 2$. In the current experiment, we covered a range of the $2.7 \leq Eo \leq 6.9$ and $0 < N < 2$. The bubbles mainly follow zigzag trajectories in GaInSn when $B = 0$, rather than the helical or rectilinear trajectories as found by Mori et al. (1977) in mercury. It is difficult to compare the two experiments exactly. We can see only several similarities between Figure 3.24 and Figure 3.25(b). Since bubbles follow zigzag trajectories in the current experiment, the transverse field indeed decreases the C_D

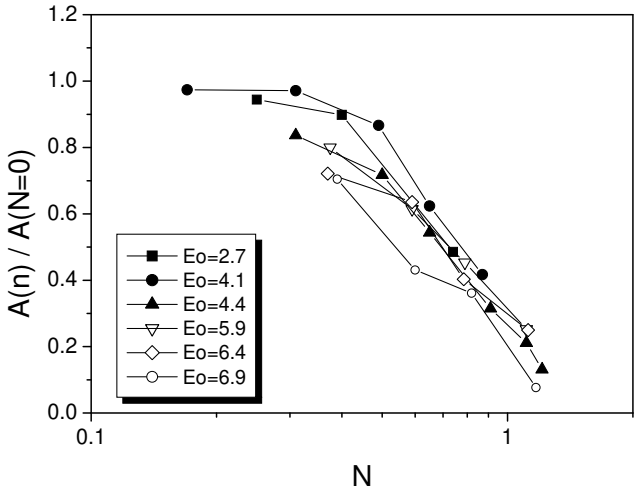

Figure 3.26: Velocity oscillation amplitude vs. interaction number in a transverse magnetic field.

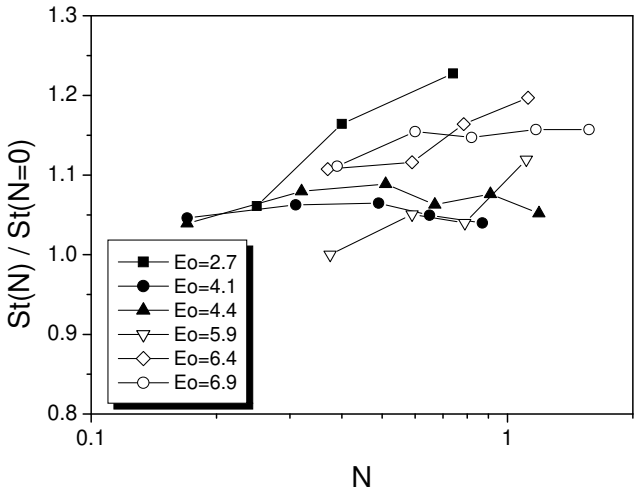

Figure 3.27: Bubble Strouhal number vs. interaction number in a transverse magnetic field.

of all bubbles when $0.5 \lesssim N \lesssim 1$, probably due to the modifications of the trajectories. Afterwards, the C_D of bubbles at $5.9 \leq Eo \leq 6.9$ start to increase when $N > 1$. However, we were not able to achieve larger N in the experiments because of the limitation of the facility.

Figure 3.26 shows the amplitudes of the oscillation concerning the vertical velocity of bubbles as a function of N. The transverse field decreases the oscillation amplitudes more distinctly in comparison to a longitudinal field, as shown in Figure 3.20. The significant decrease of the amplitudes indicate that the bubble trajectory variations are prohibited. The frequencies of the oscillations are slightly increased for all bubbles, a tendency contrary to

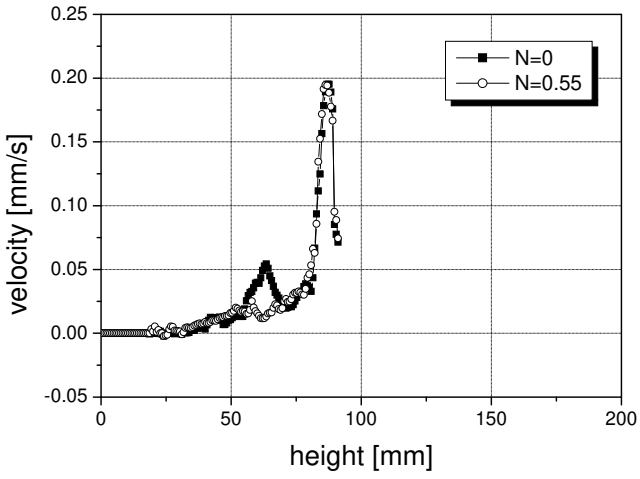

(a)

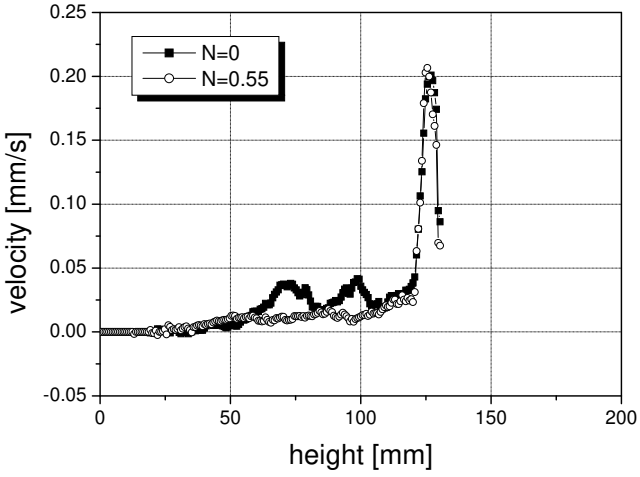

(b)

Figure 3.28: Two typical snapshots of the bubble wake velocity distribution along the path centerline ($d_e = 4.8$mm).

that in a longitudinal field (see Figure 3.21). The increased frequencies seem surprising and probably can be attributed to the modification of vorticity accumulation on the bubble interface.

The influence of the transverse field on the bubble wake is shown in Figure 3.28 by two typical snapshots. In comparison to the flow in a longitudinal field in Figure 3.22, different damping effects can be observed in Figure 3.28. The transverse field damps the near wake of the bubble more distinctively. Furthermore, the transverse field does not enhance the flow in the region between $20 \leq z \leq 100$ mm. On the whole, the flow velocities in the bubble wake become smaller if we compare the profiles along the axis of the cylinder.

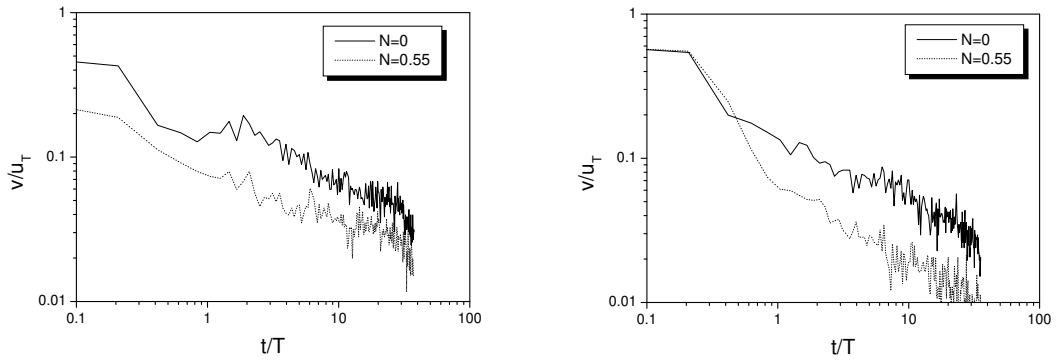

(a) (b)

Figure 3.29: Vertical component liquid velocity decay induced by a 4.8mm bubble with and without the presence of the horizontal magnetic field: (a) the time series of the liquid velocity at z=90mm; (b) the time series of the liquid velocity at z=125mm.

The transverse field also changes differently the decaying processes of the liquid velocity. Figure 3.29 shows two examples of velocity series located on the cylinder axis. The velocities always decay faster in the transverse magnetic field, a tendency contrary to that in Figure 3.23.

The different damping effects on the bubble-induced flows in the two magnetic field deserve further discussions. It is known that a static magnetic field damps fluid motion non-isotropically. The flow is restructured as if the momentum is transported along the magnetic field lines. As a result, the flow tends to become two-dimensional and independent on the field lines. In current experiments, bubbles shed intermittently hairpin vortices behind them, as shown in Figure 3.8 and Figure 3.9. Naturally, such vortices will be changed differently depending on the direction of the magnetic field. The damping effects will be strong if the axes of the vortex filaments are perpendicular to the field lines; whereas the damping effects are weaker if the axes of the vortex filaments are aligned with the field lines, as discussed in Chapter 1. Therefore, we obtained the different tendencies in Figure 3.22 and Figure 3.28, as well as between Figure 3.23 and Figure 3.29.

3.5 Summary and discussion

In this chapter, we investigate the motion of a single bubble in a bulk of stagnant liquid metal, especially with the focus on the influence of a static magnetic field on the bubble motion and the bubble-induced flow. In the original flow of $B = 0$, the bubble motion is analyzed in terms of the terminal velocity, the drag coefficient, the oscillation frequency of

the bubble velocity and the corresponding Strouhal number. The obtained results in GaInSn are validated with the theoretical prediction of Mendelson equation (equation 3.16) and other experimental data in water or mercury in the literature. A static magnetic field changes the motion of bubbles and the bubble wakes simultaneously. The main results concerning the drag coefficient in the two magnetic fields are shown in Table 3.7

In a longitudinal magnetic field											
Eo	2.2	2.5		3.4	4.9	6.6					
C_D	↗	↗		↘	↘	↘					
In a transverse magnetic field											
Eo			2.7	4.1	4.4		5.9		6.4		6.9
C_D			↗ ↘	↘	↘		↘ ↗		↘ ↗		↘ ↗

Table 3.7: A summary of the drag coefficients of bubbles in the two magnetic fields

A longitudinal field stabilizes the bubble motion. Although the velocity of a bubble still oscillates at $N \sim 1$, the amplitude and frequency of the velocity decreases monotonically. The longitudinal field increases the drag coefficients of small bubbles (Eo = 2.2 and 2.5), whereas the field decreases the drag coefficients of larger bubbles (Eo = 3.4, 4.9 and 6.6). Furthermore, the fluid flow in the bubble wake is changed, too. The distribution of the fluid velocity becomes smooth in the field direction. The phenomenon corresponds to the transport of momentum along the field lines. As a result, the liquid velocities in far wake become larger than those of the original flow. The results show that the magnetic field re-organizes the fluid flow, rather than simply damps the motion.

In comparison, a transverse magnetic field changes the flow differently. The transverse field decreases the drag coefficients of smaller bubbles (Eo = 2.7, 4.1 and 4.4), however, the tendency becomes non-monotonic for bubbles with Eo = 5.9, 6.4 and 6.9. The oscillations of bubble velocity are changed, too. The amplitudes of oscillation are decreased significantly, whereas the frequencies are increased. Besides, the transverse field damps the flow in the bubble wake effectively. The magnitudes of liquid velocity are decreased along the vertical line of the cylinder axis.

The modifications of the bubble motion can be related to the changes of the bubble wake by the magnetic fields. For instance, the bubble lateral movement can be caused by the asymmetry of the vortex filaments in the hairpin vortex, see for example de Vries (2001) and Prosperetti (2004). Furthermore, for a bubble with a zigzag trajectory in a contaminated liquid, the frequencies of the velocity oscillation, the vortex shedding and the

trajectory variation are directly coupled together, see Fan & Tsuchiya (1990) and Veldhuis et al. (2008). In the current experiments, both magnetic fields damp the flows in the near wake of a bubble. Therefore, the lateral motion of the rising bubble is weakened. As a result, the averaged vertical velocity of the bubble is increased. This explains the results of decreased C_D in both the transverse and the longitudinal field.

Furthermore, it is shown that the transverse field damps the bubble wake more effectively. In other words, the two filaments of the hairpin vortices, hence the bubble lateral motion, will be more effectively damped. The bubble will follow a vertical linear trajectory if N is large. The increase of N will increase the drag coefficient of the bubble, a tendency similar to that of a fixed sphere in a transverse magnetic field. We found this tendency for large bubbles in the transverse field.

There are several questions that cannot be directly answered now, due to several reasons. We are limited in the range of $N < 2$ in the current experiments; therefore, it is impossible to answer when the drag coefficient of the bubbles will start to increase finally when N is large. Besides, the current measuring technique is not able to resolve the process of vorticity generation as well as the vortex shedding on the bubble interface, since the sizes of those vortices are probably smaller than the size of measuring volume. Additionally, new measuring techniques probably are needed in order to study accurately the zigzag trajectory of the bubble motion in this opaque environment.

Chapter 4

Flow driven by a bubble plume in a static magnetic field

This chapter is concerned with the fluid flow driven by a bubble plume in a cylindrical container, which is exposed to a vertical and horizontal magnetic field, respectively. We start with a review of literature. Convective flows driven by heat are intensively investigated up to now. It is well-known that a static field damps the convection. However, several studies based on temperature measurements show that the convective heat transfer can be enhanced by a static field under certain circumstances. Nevertheless, there seems no direct measurement of the velocity field of the corresponding flow. In the current work, we measure the recirculating flows driven by rising bubbles in the cylinder using UDV, which allows a flow mapping for the first time. The results show that a vertical field always stabilizes the fluid motion, whereas a transverse field can result in transient oscillating flow patterns with dominant frequencies in a range of moderate Hartmann numbers. In the end, a discussion is given concerning the phenomena. We also point out a similarity between the flows in the current work and air-water flows in two-dimensional containers.

4.1 The influence of a DC field: a literature review

In this section, we briefly look through the literature concerning the influence of a DC magnetic field on the flows driven by jets, either single-phase or two-phase, as well as the flows driven by a buoyancy force if a temperature gradient is applied.

4.1.1 MHD two-phase flow

Fluid flows driven by gas bubbles in a container, known as bubble column, are studied for long time. Most of the investigations are concerned with the flow of transparent liquids, such as water or electrolytes. For instance, a global recirculation of fluid can be generated inside the container by injecting bubbles through a nozzle at the center of the bottom. The

resulting fluid motion is characterized by ascending flows in the center of the container and descending flows close to the wall. Different flow patterns can appear when the gas flow rate is high, and detailed discussions can be found, for example, in the reviews given by Mudde (2005) and Guet & Ooms (2006).

Similar two-phase flows occur in metallurgical engineering. For instance, gas bubbles are usually injected into a bulk of molten metal contained in a ladle. The rising bubbles drive the melt into motion and therefore enhance the mixing inside the liquid. Several experiments and simulations were carried out in a water or liquid metal bath concerning the flow without a magnetic field, see for example Iguchi et al. (1992, 1994), Mazumdar & Gathrie (1995) and Mazumdar & Evans (2004). The investigations are concerned with the global flow structures, the turbulent fluctuations in the fluid, the recirculating zones below the free surface, as well as the distributions of the void fraction inside the vessel. However, no investigation is conducted until now concerning the influence of the magnetic field on such flows.

Earlier studies are mainly concerned with the influence of a DC field on bubbly pipe flows. For instance, Eckert et al. (2000a) investigated the lateral dispersion of a bubble swarm in a channel flow in a longitudinal and transverse magnetic field, respectively. Gas bubbles were injected via a single orifice in the center of the cross section. The results show that a longitudinal field keeps the flow axis-symmetric and confines the bubbles around the centerline, whereas a transverse field leads to a strong anisotropy in the distribution of the void fraction with respect to the direction of the field lines.

In two-phase flows, it is the liquid metal, rather than gas bubbles, which directly experiences the electromagnetic force. Therefore, we will also look through the investigations concerning the influences of a static magnetic field on the single-phase melt flows driven by injecting fluid or a temperature gradient in the following sections.

4.1.2 Jet flow in a static magnetic field

Davidson (1995) investigated the flow of a single-phase jet in a static magnetic field. Figure 4.1(a) shows the configuration of the problem. The flow is generated by a side-wall injection of fluid in y direction and exposed to a transverse magnetic field in z direction. On the axis of the jet, the fluid velocity is the highest. Therefore, the induced electric current mainly goes in the x direction. The current closes itself in far region where the fluid velocities are smaller. The distribution of the current loop is similar to that shown in Figure 4.1(b). Under such conditions, the jet experiences a non-isotropic electromagnetic force. The force points either into or out of the page, depending on the induced current. The directions of the force are

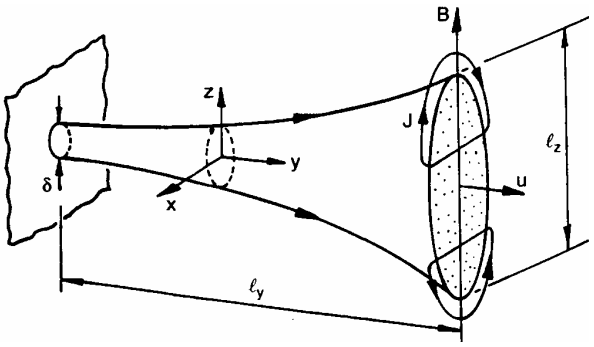

(a)

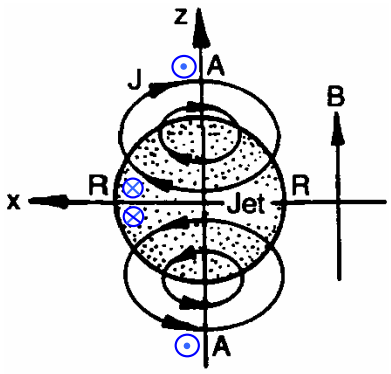

(b)

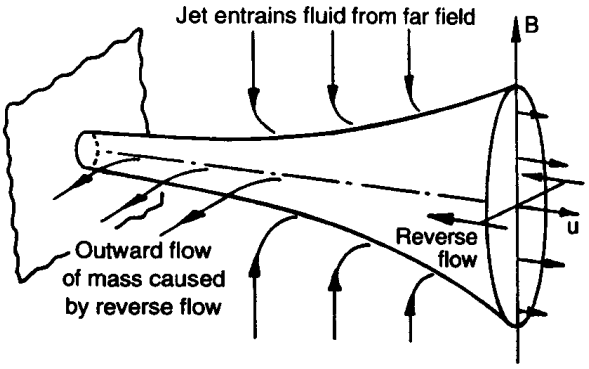

(c)

Figure 4.1: A jet produced by side-wall injection in a transverse magnetic field: (a) configuration of the jet and the magnetic field; (b) the path of the induced electric current and the direction of the induced electromagnetic force, the reverse flow is marked by **R** and energy diffuses to points marked by **A**; (c) the evolution of the MHD jet, the jet draws in fluid from the far field and produces reverse flows for the outward flow of mass. Pictures are taken from Davidson (1995) and Davidson (2001).

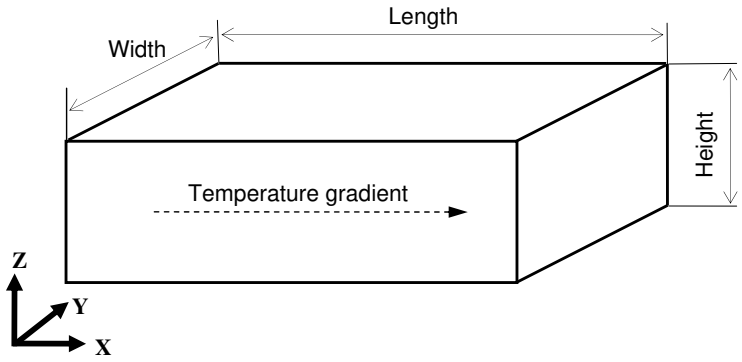

Figure 4.2: A schematic view of a convective flow driven by a horizontal temperature gradient in a static magnetic field. The temperature gradient is horizontal. In the discussion of this section, a "longitudinal" magnetic field is parallel to the temperature gradient, a "transverse" field is horizontal and perpendicular to the temperature gradient, and a "vertical" field is parallel to the gravity.

indicated by the symbols in the figure. Correspondingly, the shape of the jet is changed in the way depicted in Figure 4.1(c). The jet entrains fluid from far field along z axis, whereas the jet also creates a reverse flow along x axis. As a result, the cross-section of the jet is stretched along the direction of the field lines.

4.1.3 Convective flow damped by a static magnetic field

Convective flows driven by a temperature gradient are studied intensively in the literature, especially with the focus on the influence of a DC magnetic field. The research background comes from crystal growth or other metallurgical applications, where an electromagnetic field can be used to control the melt flow.

Convective flow driven by a horizontal temperature gradient

One of the pioneering investigations was conducted by Hurle et al. (1974) concerning the onset of an oscillating flow of gallium in a rectangular container in a "transverse" magnetic field, which is illustrated in Figure 4.2. A horizontal temperature gradient is supplied by heating a vertical side wall while cooling the opposite side. The critical Rayleigh number is used to represent the critical temperature difference ΔT_c corresponding to the onset of non-steady flows

$$Ra_c = \frac{\alpha g \Delta T_c d^4}{\nu \kappa l} \tag{4.1}$$

where α is the expansion coefficient of the melt, g the gravity acceleration, ν the kinematic viscosity, κ the thermal diffusivity, d the melt depth and l the container length. The magnetic

induction B is normalized into the Hartmann number Ha, as defined in equation (1.9). The results show that Ra_c is delayed by the magnetic field and Ra_c increases linearly with Ha^2 when $3 \times 10^3 < Ra < 15 \times 10^3$ and $0 < Ha^2 < 300$. Juel et al. (1999) investigated the flow in an analogous configuration. They focus on the changes of the convective heat transfer in the transverse field. The maximum magnetic induction of the field is 0.125 T, which corresponds to $Ha = 64$. They use thermocouple to measure the temperature of the fluid; in addition, the velocity field is simulated numerically. It is shown that the flow becomes two-dimensional with respect to the field direction. The velocity magnitudes are decreased and the velocity distributions become increasingly uniform over the length of the container. Besides, the transverse field decreases the temperature difference in the vertical direction. The distribution of the temperature becomes symmetric in the upper and lower parts of the cavity, which is otherwise hard to be observed without the magnetic field.

Hadid et al. (1997) and Hadid & Henry (1997) investigated numerically the convective flows in a longitudinal and a vertical field, respectively, in a cavity of $length : width : height = 4 : 1 : 1$. Their results show that both magnetic fields damp the flow velocities and change the flow structures. Compared to the longitudinal field, the vertical field damps the velocity maxima more efficiently. This phenomenon is explained by taking into account of the different distributions of the electrical currents, electrical potentials and, therefore, different electromagnetic forces in the two fields.

Investigations are also carried out concerning the different influences when the direction of the field is changed with respect to the temperature gradient. Hof et al. (2003, 2005) measured temperature fields of the gallium flow in a rectangular container ($length : width : height = 5.0 : 1.3 : 1.0$). They found that a vertical field gives the strongest damping effects on the steady convection and the oscillations of the liquid velocity. In contrast, they observed that the longitudinal field is the least effective one, which is different from other studies. This inconsistency is attributed to the differences in the aspect ratios of the cavity in different studies. For example, Ozoe & Okada (1989) simulated the convective flows of molten silicon in a cubic enclosure, which is exposed to a static field in different directions. In the range of $10^6 < Ra < 10^7$ and $0 < Ha < 500$, their computations show that the longitudinal field damps the convection most effectively, whereas the transverse field is the least effective one; the vertical field, in comparison, gives moderate effects in-between. The calculations are later confirmed by experiments by Okada & Ozoe (1992) using molten gallium in a cubic enclosure ($30 \times 30 \times 30$ mm) with the maximum Ha number up to 461. They considered the magnetic field influence on the heat convection, which is characterized by the Nusselt number Nu of the system. Nu represents the ratio of the convective to conductive heat transfer in the flow.

In their experiments, the transverse field is the least efficient in damping the convection, which is the same as the conclusion from their calculations. In addition, they found that the transverse field slightly enhances the convection when Ha is moderate. However, the difference is so small that no concrete conclusions can be drawn. Later on, Aleksandrova & Molokov (2004) considered the influence of the container geometry in a configuration similar to those of Juel et al. (1999), Hof et al. (2003, 2005) and Ozoe & Okada (1989). It is shown that magnetic damping effects depend on the aspect ratio of the cavity. For the longer cavity, the vertical field is the most effective one. For the cubic container, however, the longitudinal field is the most efficient. Therefore, the inconsistencies in the above discussions are reconciled.

Convective flow driven by a vertical temperature gradient

The Rayleigh-Bénard convection, where the flow is driven by a vertical temperature gradient, has been attracting researchers' attention for a long time. Chandrasekhar (1981) considered the stability of the flow in a fluid layer heated from below in a vertical field. It is shown that the primary threshold varies with the square of Ha, a tendency similar to the results given by Hurle et al. (1974).

The convective flow in a shallow cavity, with a geometry of $length : width : height = 6 : 3 : 1$, in a vertical field was investigated by Mößner & Müller (1999). At $Ha = 0$, the flow is stationary and consists of six convective rolls when Ra is slightly higher than the critical value at $Ra_c = 1950$. However, the flow becomes oscillating if Ra is further increased. When $Ra > 10^4$, the number of convection rolls decreases to four and the flow becomes irregularly time-dependent. The application of a vertical magnetic field changes the flow clearly, the flow becomes steady and the convection is suppressed. Touihri et al. (1999) simulated the convective flows in a cylindrical container with $H/D = 0.5$ and 1, which are exposed to a vertical and a horizontal magnetic field, respectively. It is found that both fields damp the fluid motion, whereas the vertical field is more efficient. Besides, it does not break the axis-symmetry of the flow. However, the horizontal field changes the axis-symmetry of the flow. Specifically, the flow rolls are stabilized if their axes are parallel to $\mathbf{B}$, whereas they are strongly damped if the axes are perpendicular to field lines.

In a turbulent Rayleigh-Bénard convection, the dependence of the heat transfer on a magnetic field is investigated by Cioni et al. (2000). They measured the temperature of mercury by arranging thermistors on the top and bottom plate of a cylindrical vessel ($D/H = 1$), which is exposed to a vertical magnetic field. The field reduces the convective heat transfer clearly and results in two different flow regimes. Nu is proportional to Ra when Ra is low,

whereas Nu scales as $Ra^{0.43}$ when Ra is high.

Kenjereš & Hanjalić (1999) compared the Rayleigh-Bénard convection in a vertical and a horizontal magnetic field, respectively. It is found that the vertical field can totally suppress the convection and lead to a pure diffusive regime. In contrast, the horizontal field reduces the heat transfer until the flow becomes fully two-dimensional with respect to the field lines; Afterwards, a further increase of the field cannot reduce the heat transfer any more.

4.1.4 Convective flow enhanced by a static magnetic field

Most of the investigations demonstrate that a DC magnetic field damps or stabilizes liquid metal flows. The effect depends on several factors, such as the direction of the magnetic field and the geometry of the fluid domain. Recently, several studies also show some unexpected phenomena. Owing to the anisotropic character, a DC field can intensify a flow under certain circumstances.

Tagawa & Ozoe (1997) investigated numerically the natural convection in a cubical enclosure. The flow is induced by heating one side of the vertical wall and cooling the opposite one. The system is exposed to a transverse magnetic field. The results show that, for a wide range of Ra, a weak magnetic field slightly enhances the convective heat transfer, which is manifested by an increased Nusselt number. A further increase of Ha decreases the convective heat transfer again. The numerical results are verified in experiments by Tagawa & Ozoe (1998).

The enhancement of the convective heat transfer by a DC field is observed by Burr et al. (2003), Tagawa et al. (2002) and Authie et al. (2003) in their experimental and numerical studies, too. They considered buoyant flows in long vertical cavity driven by a horizontal temperature gradient. Likewise, the flows are exposed to a transverse magnetic field. In comparison to the original flow at $Ha = 0$, Burr et al. (2003) observed that the convective heat transfer is clearly enhanced when $Ha < 400$. They explained that the damping effect on the convection is counterbalanced by a re-organization of the flow structures due to the magnetic field. The new flow state improves the heat transfer. The measured spectra of temperature fluctuations indicate the formation of larger-scale vortices in the flow, which can be more effective in transferring heat by convection.

The Rayleigh-Bénard convection in a horizontal magnetic field is studied by Burr & Müller (2002), who observed enhanced heat transfer compared to the ordinary flow, too. Local temperature measurements show that the increase in the heat transfer is associated with an increasingly non-isotropic state of convection, where flow rolls become aligned with

the magnetic field lines.

In summary, there are intensive studies on the convective flows of single-phase fluids in a DC magnetic field. The unexpected phenomenon of the enhanced heat transfer can occur because of the strong non-isotropic effect of the magnetic field. However, owing to the limitation of the measuring techniques, most of the previous investigations rely on the temperature measurements and numerical simulations to study the flow. Direct measurements of the velocity field are rare concerning the phenomena inside the opaque liquids. Until now, no study seems to exist concerning the flow driven by a bubble plume in a static magnetic field. We will investigate the flow driven by a bubble plume in a magnetic field in the following parts. Two field configurations will be considered: the direction of the magnetic field is either vertical or horizontal. We use the ultrasound Doppler method to directly measure the flow velocity field.

4.2 Experimental setup

The experimental setup is shown in Figure 4.3. The eutectic alloy GaInSn was contained in a cylindrical vessel of Plexiglas, which provided insulating walls. The bulk of the liquid metal had a diameter $D = 2R$ of 90 mm and a height H of 220 mm, leading to an aspect ratio of $A = H/D = 2.44$. Argon gas bubbles were injected through a single nozzle with an inner diameter of 1 mm located at the center of the container bottom. The gas flow rate Q_g was adjusted using a mass flow controller (MKS 1359C, MKS Instruments). Experiments were carried out in a range of low gas flow rates (Q_g=0.33-6.67 cm^3/s) to ensure the formation of a dispersed bubbly flow. The Helmholtz configuration of a pair of copper coils was used to generate a homogenous magnetic field, which covered the bulk of the liquid metal. The direction of the magnetic field can be arranged as either vertical (longitudinal) or horizontal (transverse). In our experiments, magnetic fields were applied up to a maximum strength of 0.28 T, which corresponded to a maximum Hartmann number of $Ha = 484$.

We used the DOP2000 instrument with standard 4 MHz (TR0405LS) or 8 MHz (TR0805LS) transducers to measure the flow field. By a standard 8 MHz transducer, we achieved a spatial resolution of about 0.69 mm in the axial direction and 7.1 mm in the lateral direction at the distance of 100 mm ahead of the transducer, respectively. We carried out the measurements under different sampling frequencies, which were varied from 5 Hz to 30 Hz. The ultrasonic sensor was vertically installed at the container bottom. The emitted ultrasound beam can be considered as a vertical line inside the meridional plane. In this way, profiles of the vertical velocities can be obtained along the line. A traversing system controlled the movement and

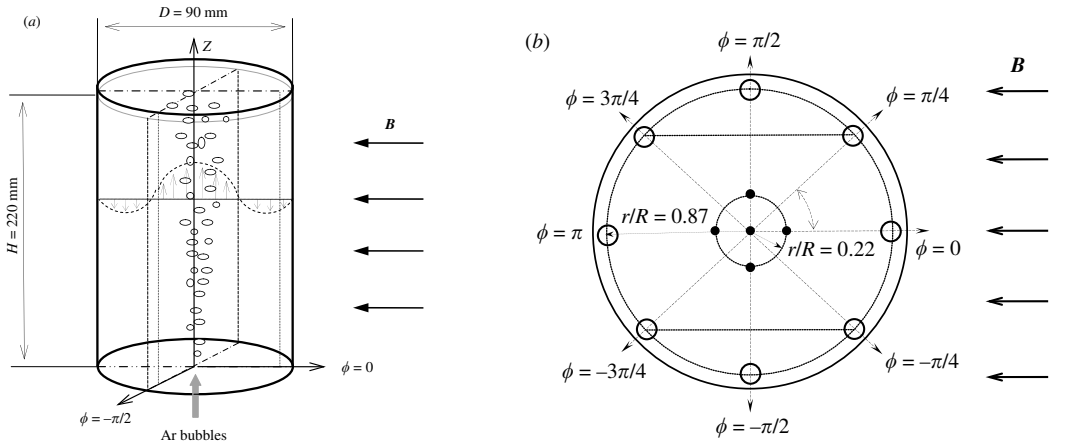

(a) (b)

Figure 4.3: Sketch of experimental set-up: (a) schematic view of the bubble column configuration; (b) container cross-section with indicated measuring positions used for the conductance probes (marked by •) and UDV sensors (marked by ◯).

the position of the transducer. Therefore, flow mappings can be carried out in a cylinder meridional plane. During the measurement, the sensor moved in a step of 3 mm along the diameter of the container bottom. The measuring time at each spatial position was 3 minutes, which was long enough to yield reliable results. In all figures below, we use positive velocities to represent upward flows and negative velocities for downward flows.

4.3 Experimental results

In this chapter, all results from DOP2000 are liquid-phase velocities. To extract the liquid velocity from the measured signals, we used the threshold method in Chapter 2. In the following sections, we will start with the flow in a vertical magnetic field. Afterwards, the magnetic field will be changed into the horizontal direction. Finally, the results will be compared and discussed.

4.3.1 Flow in a longitudinal magnetic field

Figure 4.4 shows the measured velocity fields of the bubble-plume-driven flow with and without the magnetic field. We use the container height H to normalize z coordinate and the container radius R for radial coordinate r. Figure 4.4(a) shows the original flow of $B = 0$. An upward flow exists around the centerline of the cylinder because of the rising bubbles. The fluid descends close to the wall and forms a global structure of recirculation. The strongest

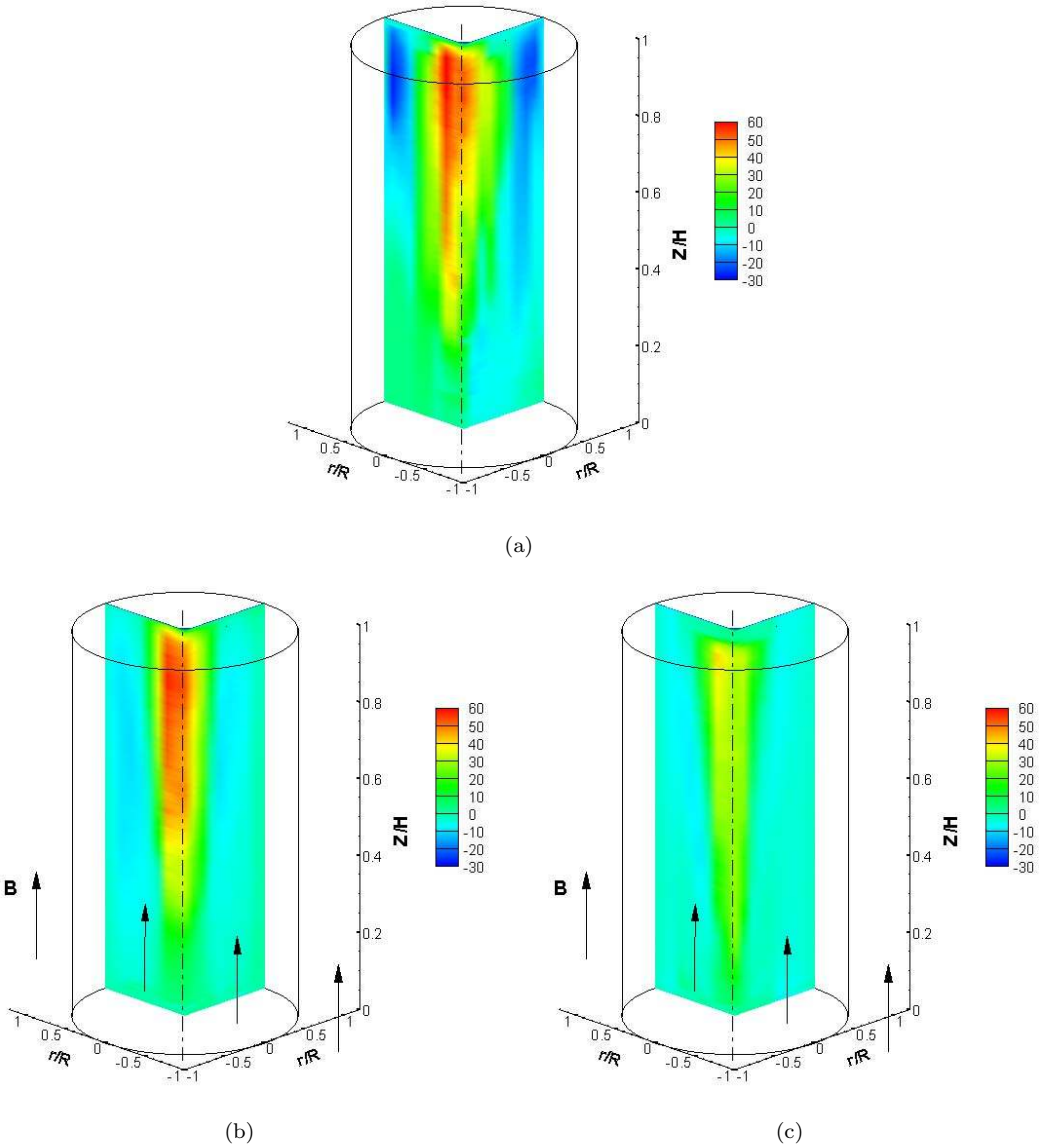

(a)

(b)

(c)

Figure 4.4: Time-averaged liquid-phase flow fields of bubble-driven flow in a longitudinal magnetic field at various Hartmann numbers (Q_g=0.33 cm^3/s). (a) $Ha = 0$, (b) $Ha = 193$, (c) $Ha = 335$. The color bar denotes the velocity in mm/s.

downward flows are located just below the free surface, while the flow velocities are smaller in the lower part of the container. The flow structures are comparable to each other in the two orthogonal planes.

The flow fields at different magnetic inductions are shown in Figure 4.4(b) and 4.4(c), respectively. A clear tendency can be observed. As a weak field of $B = 0.11$ T ($Ha = 193$) is applied, the recirculation zones below the free surface disappear. Besides, the velocities of

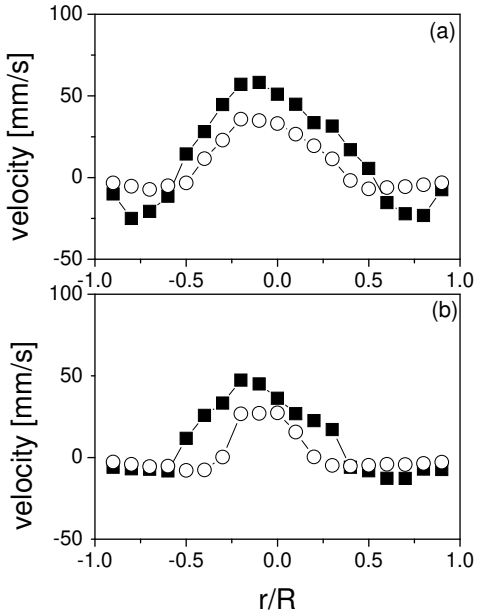

Figure 4.5: Radial distributions of the vertical velocity component at different heights and various Hartmann numbers in a longitudinal magnetic field: (a) $Z/H = 0.9$; (b) $Z/H = 0.5$. (■ denotes $Ha = 0$; ◯ denotes $Ha = 335$; Q_g=0.33 cm^3/s).

the flow are increased in the lower part of the container. In other words, the distributions of the velocity become almost uniform in the direction of the field lines. At $B = 0.19$ T ($Ha = 335$), the magnetic field damps clearly the upward flows around the cylinder axis and the downward flows outside the bubble plume.

Figure 4.5 shows the distributions of the liquid velocity along the cylinder diameter. we choose two different heights, which are below the free surface and at the mid-height of the cylinder, respectively. The velocity magnitudes are decreased for the ascending flows in the cylinder center and for the descending flows close to the cylinder wall. The region of the upward flow is confined in a narrow range in the cylinder center, (a similar effect on the distribution of the void fraction in a bubbly pipe flow is already shown by Eckert et al. 2000a,b). At the same time, the distributions of downward velocity become flattened in the region between $0.5 \lesssim |r/R| < 1$.

We also compare the downward flow of the fluid close to the container wall. In the current configuration, flow fields are almost axis-symmetric according to Figure 4.4 and Figure 4.5. Therefore, we only consider the flow contained in a meridional plane, which corresponds to $\phi = 0$ in Figure 4.3(b). If we choose the radial position at $r/R = 0.87$, the velocity distributions along the vertical line at that position are shown in Figure 4.6. The fluid goes

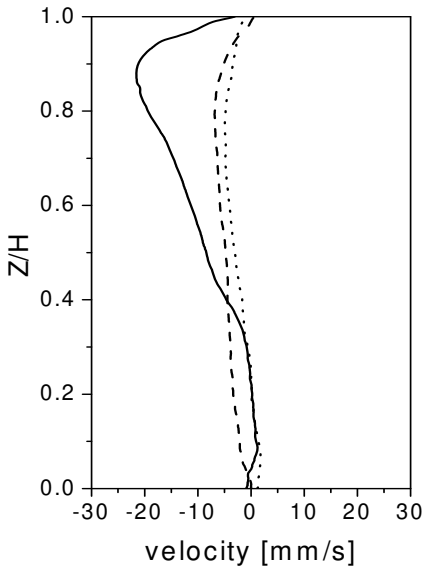

Figure 4.6: Vertical distributions of the vertical velocity component at various Hartmann numbers in a longitudinal magnetic field. —— $Ha = 0$; $---$ $Ha = 193$; $\cdots\cdots$ $Ha = 335$. The data were acquired at the radial position $r/R = 0.87$ and the gas flow rate Q_g=0.33 cm^3/s.

downward there. For the original flow, strong downward motion can be clearly observed below the free surface, where large magnitudes of negative velocities exist. The longitudinal field damps the flow effectively and smoothes the velocity profiles when Ha is increased. The effect corresponds to the spreading of momentum along the field lines, as discussed concerning the bubble wake in a vertical field.

The aforementioned results are concerned with time-averaged flow fields. In fact, the magnetic field changes the transient motion of the melt, too. For an illustration, we display a series of consecutive velocity profiles which were obtained at one location for a certain time. If we choose a vertical line at $r/R = 0.87$, the results can be plotted as a velocity contour in the form of the spatial-temporal distribution, as shown in Figure 4.7. In the figures, the color represents the velocity magnitude. The vertical coordinate represents the height along the cylinder, and the horizontal coordinate represents the time scale. At $Ha = 0$, a region containing distinct downward flows can be observed in the upper part of the vessel, whereas the flow is weak in the lower part. At $B = 0.11$T ($Ha = 193$), the field significantly damps the downward flow. A downward flow occurs only occasionally with smaller velocities and disappears in a short time. Further increase of Ha leads to a stable flow with smaller velocities, as shown in the Figure 4.7(c). The results confirm that a flow can be damped in

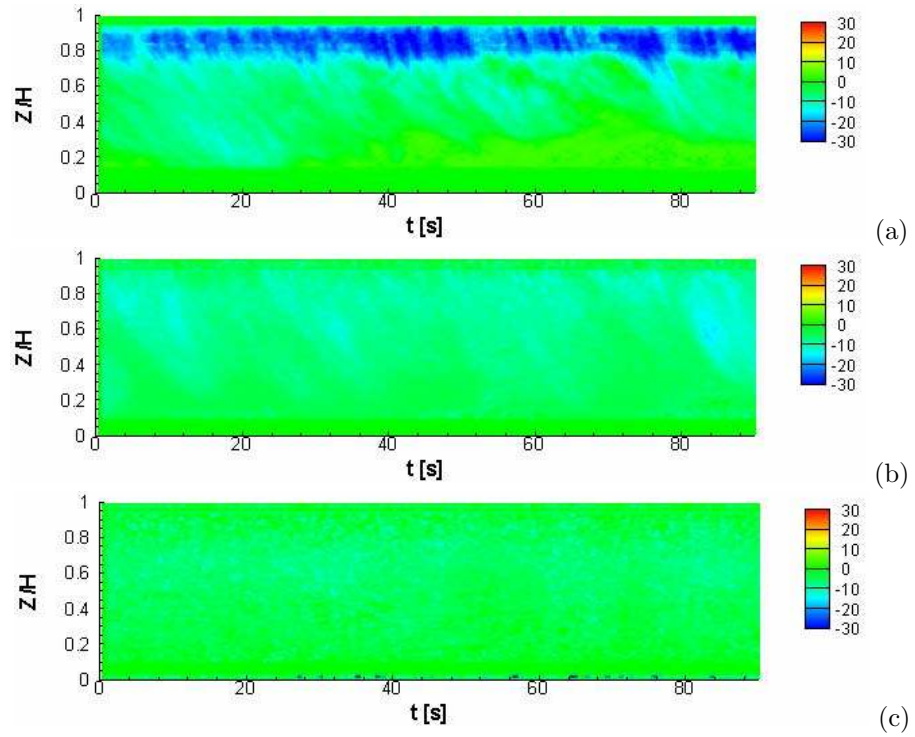

Figure 4.7: Spatiotemporal distributions of the vertical velocity component along a vertical line at various Hartmann numbers in a longitudinal magnetic field. (a) $Ha = 0$; (b) $Ha = 193$; (c) $Ha = 335$. The data were acquired at the radial position of $r/R = 0.87$ in the plane of $\phi = 0$ at the flow rate of Q_g=0.33 cm^3/s.

a static magnetic field.

It is worth to point out that, in the above results, the axes of the global recirculation flow in the meridian planes are perpendicular to the direction of the longitudinal magnetic field. The flow structures experience the same damping effects. Therefore, the flow field remains symmetric.

4.3.2 Flow in a transverse magnetic field

In this section, we expose the flow to a horizontal magnetic field, which is also called a "transverse" magnetic field. We focus on the flows in the meridional planes that are parallel and perpendicular to the magnetic field lines, respectively. At the beginning, a qualitative assessment of the bubble plume behavior is achieved by a visual observation on the free surface of the liquid metal. In the original flow of $B = 0$, gas bubbles emerge isotropically. The maximum of the bubble frequency appears around the center of the container cross-section. The magnetic field concentrates the bubbles into a smaller bounded spot. The

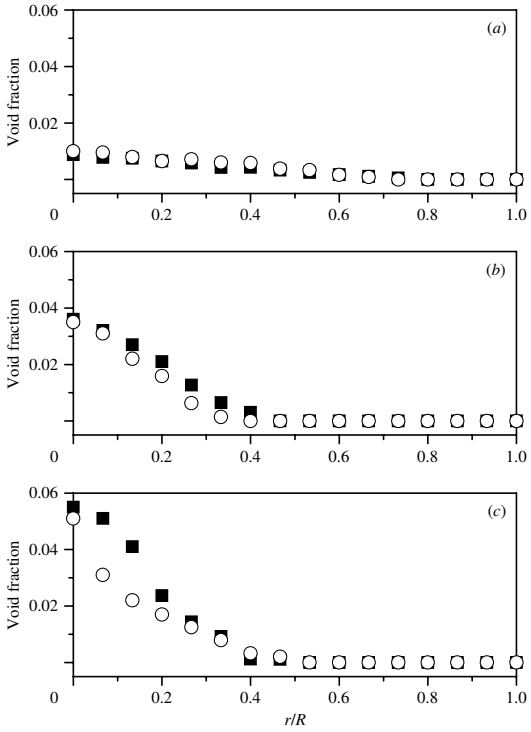

Figure 4.8: Time-averaged radial distributions of local void fractions measured using a conductance probe at various Hartmann numbers: (a) $Ha = 0$; (b) $Ha = 271$; (c) $Ha = 484$ (■ denotes the distribution along the radius at $\phi = \pi/2$; ◯ denotes the distribution along the radius at $\phi = 0$.) The data were acquired at the height of $Z/H = 0.9$ applying a gas flow rate of Q_g=3.67 cm^3/s.

position of this spot is not fixed, but shows a low-frequency oscillation along the diameter of the cylinder, which is perpendicular to the direction of the magnetic field. The distribution of the void fraction in the container cross-section can be measured using single-wire conductance probes. This kind of sensor is a standard technique in two-phase flows (Serizawa et al. 1975) and can be applied in liquid metals flows as well, see for example Eckert et al. (2000a,b).

Figure 4.8 shows the distributions of the void fraction along a cylinder diameter at a height at $z = 200$ mm ($z/H = 0.9$). The magnetic field results in a concentration of the gas bubbles in the central region around the axis of the fluid vessel. The focusing of the gas phase becomes non-isotropic with an increase of Ha and becomes more pronounced along the radial direction perpendicular to the magnetic field. This tendency agrees with the results from the MHD channel flow, see Eckert et al. (2000a).

Concerning the transient motion of the bubble plume, we use three conductance probes to count the bubble numbers at $r/R = 0$ and $r/R = \pm 0.22$ simultaneously. The three probes

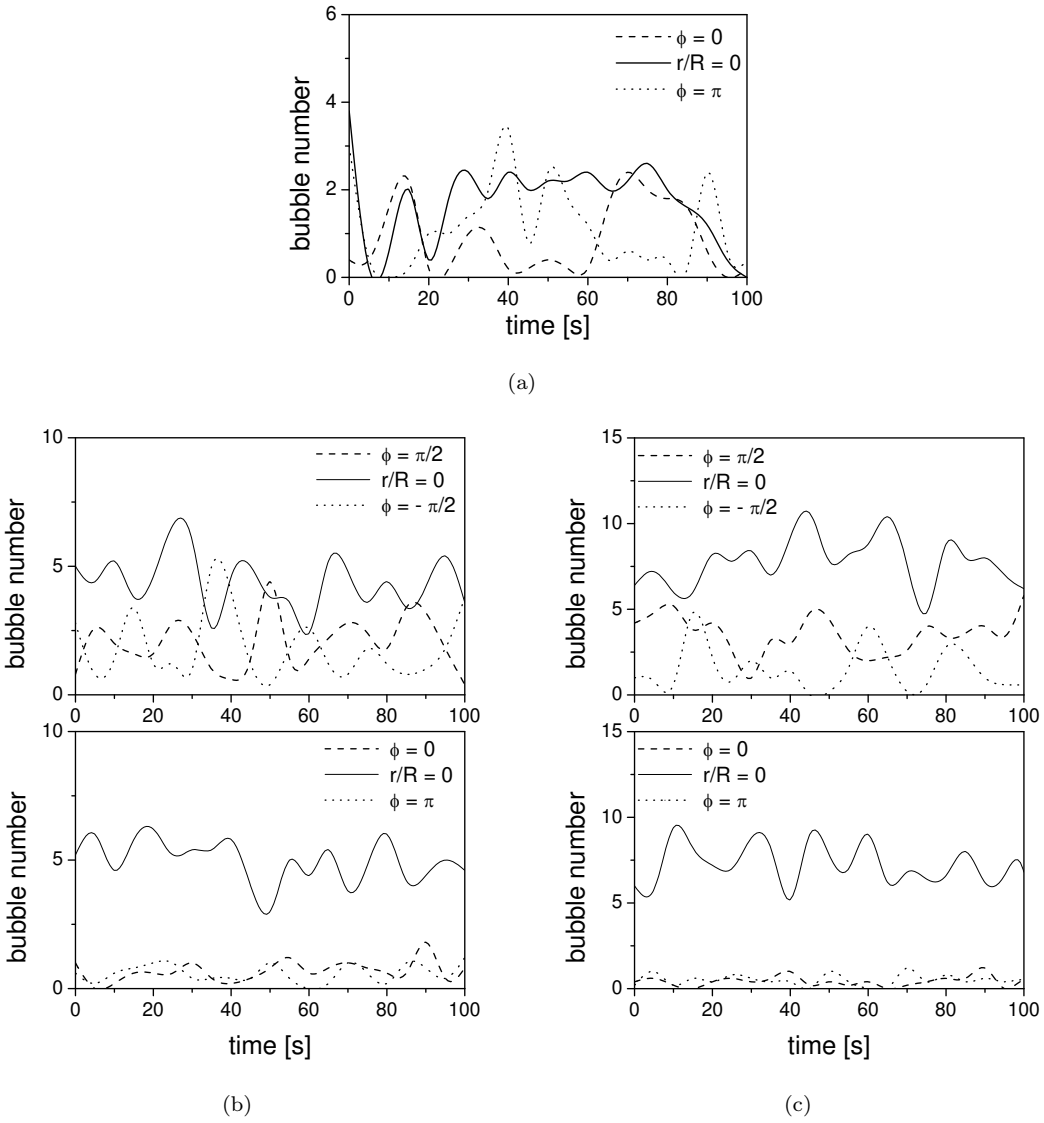

(a)

(b)

(c)

Figure 4.9: Time series of the locally counted bubble number (1/sec) at various Hartmann numbers simultaneously measured by 3 conductance probes: (a) $Ha = 0$; (b) $Ha = 271$; (c) $Ha = 484$. The data were acquired at the height of $Z/H = 0.9$ applying a gas flow rate of Q_g=3.67 cm^3/s.

are located on one container diameter, which is either perpendicular or parallel to the field lines. Time series of the measured bubble numbers are recorded in Figure 4.9 consisting of consecutively measured data points each with a time interval of 5s. Similar to our observations at the free surface, the results in Figure 4.9 also reflect that the bubble plume experiences periodic lateral motions, which occur along the diameter perpendicular to the direction of the magnetic field. This is manifested by the considerable out-of-phase oscillations of the

detected bubble numbers at $\phi = \pm\pi/2$. Long term observations show a mean periodicity of about 15s at $Ha = 271$. It is worth noting that an increase of Ha (showed in Figure 4.9c) does not result in a clear reduction of the oscillation amplitudes at $\phi = \pm\pi/2$, but significant reductions at $\phi = 0$ and $\phi = \pi$.

Figure 4.10 displays time-averaged flow fields at a relatively low gas flow rate of 0.33 cm^3/s. The velocity field in each plane is shown by velocity vectors. The original flow with $Ha = 0$ is shown in Figure 4.10(a) and (b), which correspond to the velocity fields in the two meridional planes. In the central region of the fluid container, the liquid metal is driven upwards by the rising gas bubbles. The corresponding downward motion appears in the regions close to the side walls. The magnetic field changes the velocity fields non-isotropically, as shown from Figures 4.10(c) to 4.10(h). Different flow patterns can be observed in both the parallel and perpendicular planes. The magnetic field decreases the downward flow in the parallel plane, whereas the field intensifies the circulation in the perpendicular plane. Specifically, distinct vortex structures appear at $Ha = 271$ (see Figure 4.10e), which are damped with a further increase of Ha (Figure 4.10g). Velocity measurements at higher gas flow rates reveal qualitatively similar flow patterns.

Contours of the vertical velocity obtained at $Q_g = 0.83$ cm^3/s are shown in Figure 4.11. Corresponding profiles of the vertical velocity along the radius r/R and the height Z/H are presented in the Figure 4.12 and Figure 4.13, respectively. The flow pattern of the ordinary bubble plume appears almost axis-symmetric. The maximum of the upward flow and the recirculation can be observed directly beneath the free surface. Substantial modifications of the flow structure can be observed when the magnetic field is applied. In the perpendicular plane, the fluid recirculation is intensified in the lower region of the vessel. Moreover, the recirculation zones are extended closer to the axis of the fluid container. In contrast, the fluid overall is set in an upwards motion in the parallel plane. This phenomenon is similar to that shown in Figure 4.1, as discussed by Davidson (1995, 2001).

Figure 4.12 shows the flattening of the velocity distributions along several cylinder radii, which are contained in the two orthogonal planes. The flow rises up uniformly along the radii parallel to the magnetic field lines, as shown in Figure 4.12(b). This tendency is comparable to the development of a Hartmann profile in a MHD channel flow. At the same time, a descending flow appears in the perpendicular midplane, as shown in Figure 4.12(a).

The distributions of the vertical velocity along vertical lines are displayed in Figure 4.13, corresponding to the radial positions of $r/R = 0.87$ for both parallel and perpendicular midplanes. The anisotropy of the flow field in the MHD case is demonstrated again. Periodic variations of the velocity profiles can be found in Figure 4.13(a), which correspond to the

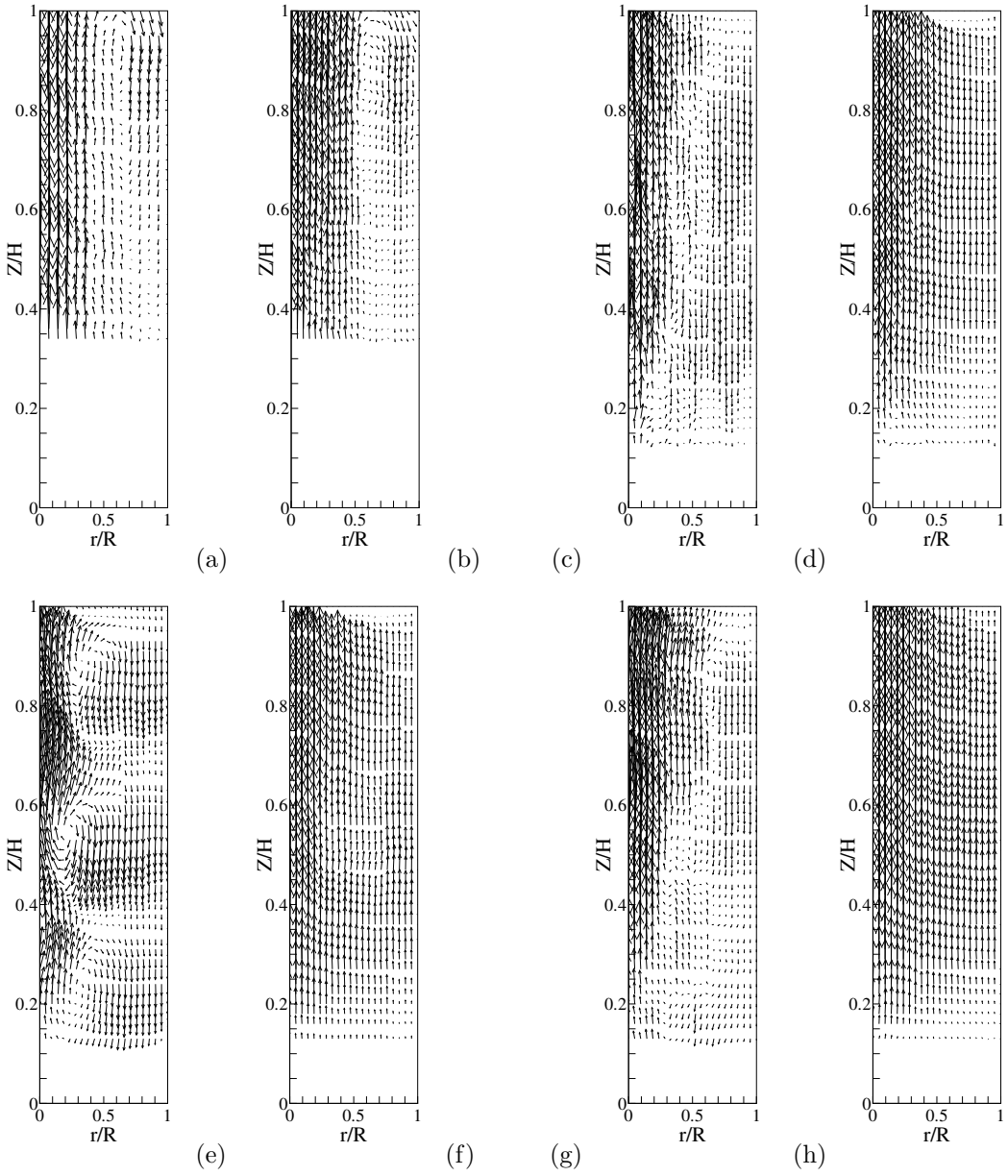

Figure 4.10: Vector plots of the liquid velocity structure at various Hartmann numbers: (a) & (b) $Ha = 0$; (c) & (d) $Ha = 162$; (e) & (f) $Ha = 271$; (g) & (h) $Ha = 484$. The figures (a), (c), (e), (g) display the flow in the perpendicular plane; and (b), (d), (f), (h) display the flow in the parallel plane. (Q_g=0.33 cm^3/s).

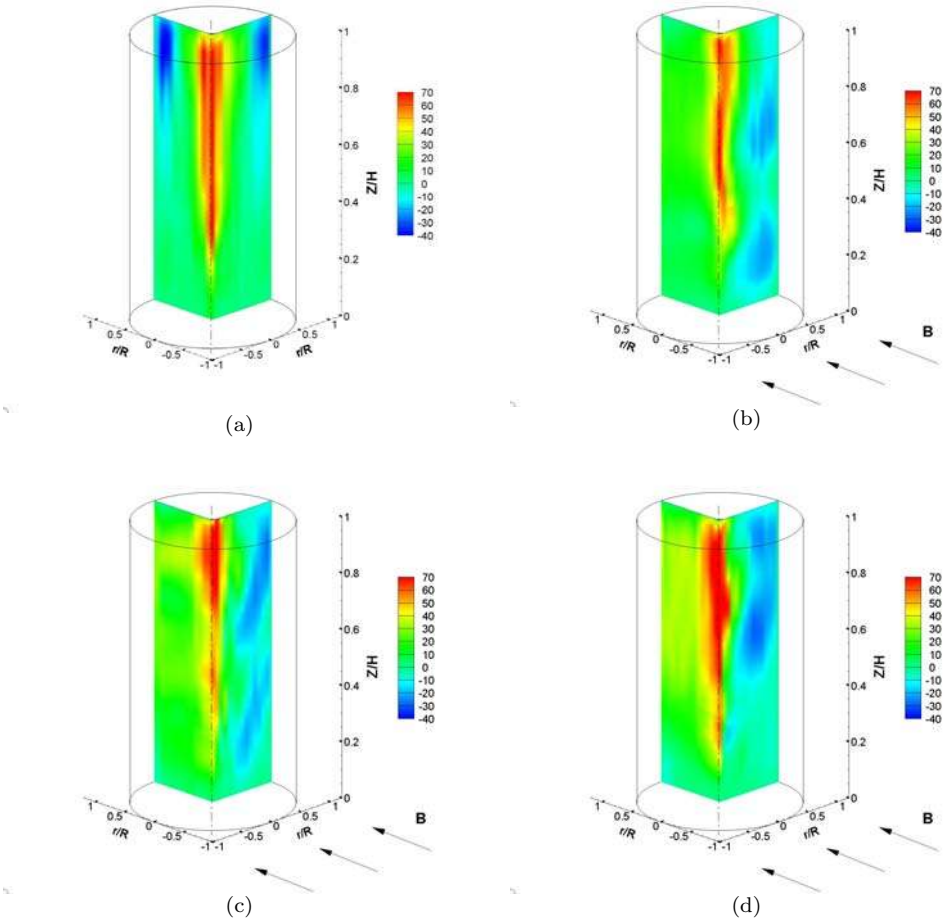

Figure 4.11: Contour plots of the vertical velocity component at various Hartmann numbers: (a) $Ha = 0$; (b) $Ha = 162$; (c) $Ha = 271$; (d)$Ha = 484$. (Q_g=0.83 cm^3/s). The color bar denotes the velocity in mm/s.

vortex structure in the flow field as already shown in Figure 4.11. In the case of the parallel plane, the magnetic field leads to a reversal of the mean velocities.

Figure 4.14 presents the time-averaged velocity and the RMS values as a function of Ha for gas flow rates of 0.83 and 3.67 cm^3/s, respectively. The values are deduced from the velocity time series at the position $r/R = 0.87$ and $z/H = 0.5$. As shown in Figure 4.14(a) the absolute values of the time-averaged velocity in both the parallel and perpendicular plane grow almost continuously as Ha increases. Furthermore, a considerable enhancement of the measured velocity variances (RMS) indicate that applying a magnetic field at moderate field strengths ($Ha = 162$ at Q_g=0.83 cm^3/s or $Ha = 271$ at Q_g=3.67 cm^3/s) gives rise to large coherent flow structures, see Figure 4.14(b). A further increase of Ha results in a damping of the oscillating flow structures accompanied by a significant decrease of the RMS value.

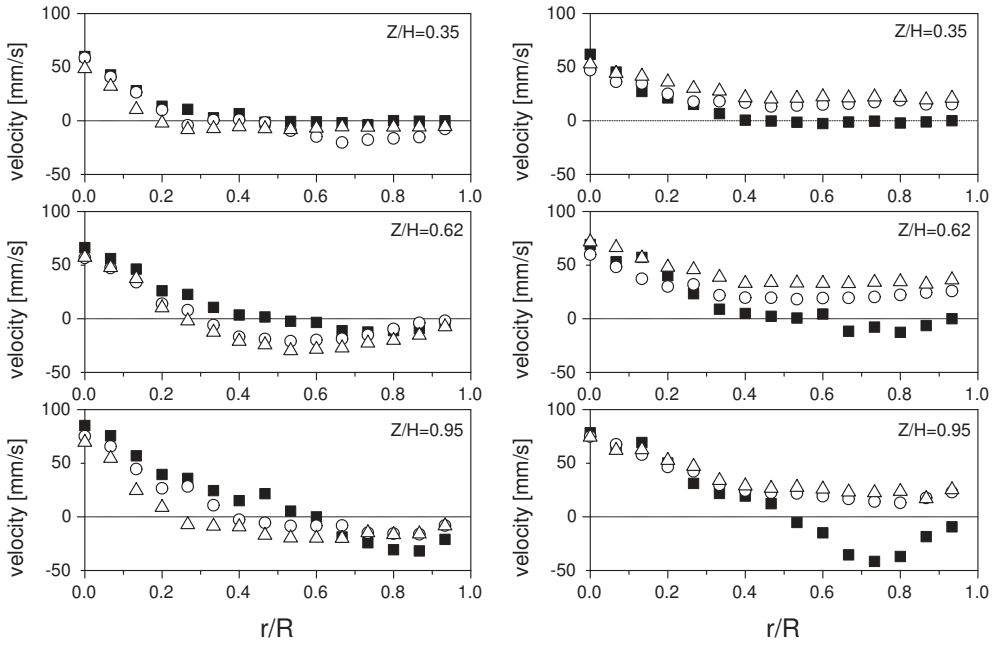

Figure 4.12: Radial distributions of vertical velocity component at different heights and various Hartmann numbers: (a) in the plane perpendicular to **B**; (b) in the plane parallel to **B**. (■ denotes $Ha = 0$; ◯ denotes $Ha = 271$; △ denotes $Ha = 484$; Q_g=0.83 cm^3/s).

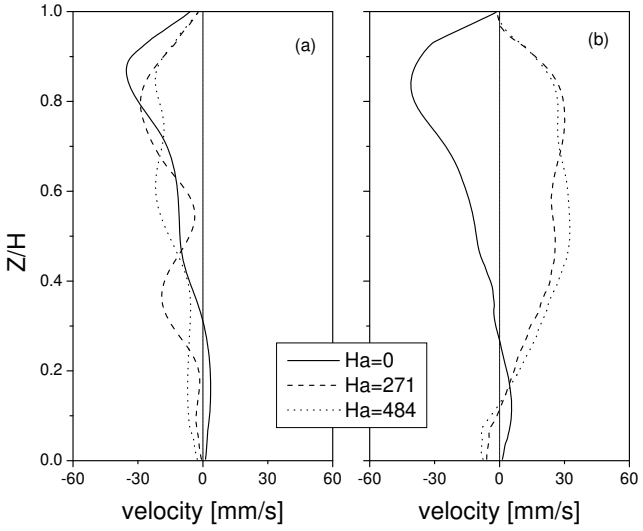

Figure 4.13: Vertical distributions of vertical velocity component at various Hartmann numbers: (a) in the plane perpendicular to **B**; (b) in the plane parallel to **B**; —— $Ha = 0$; − − − $Ha = 271$; · · · · · $Ha = 484$. The data were acquired at a radial position of $r/R = 0.87$ applying a gas flow rate of Q_g=0.83 cm^3/s.

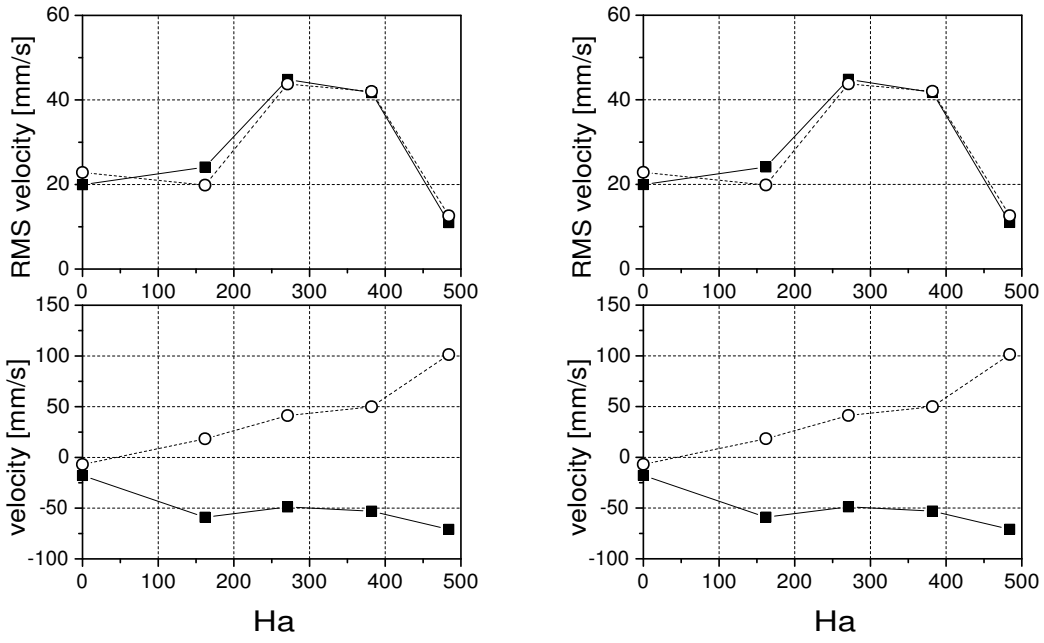

(a) (b)

Figure 4.14: RMS and time-averaged velocities calculated for different Hartmann numbers and two gas flow rates: (a) Q_g=0.83 cm$^3/s$; (b) Q_g=3.67 cm^3/s. ($-\blacksquare-$ denotes the flow in the perpendicular plane; $\cdots\bigcirc\cdots$ denotes the flow in the parallel plane) The data were acquired at the position $r/R = 0.87$ and $Z/H = 0.5$.

This tendency can also be supported qualitatively by the analysis of the transient flow to be presented in the next sections. However, the decrease of the RMS value is accompanied with a particular increment concerning the magnitude of the mean velocity.

The results regarding the spatial flow structure reveal that the application of a transverse magnetic field gives rise to large coherent structures in the flow field. In the following parts, the low-frequency transient behavior of these structures will be discussed. For this reason, the time series of the vertical velocity profiles are recorded along a vertical line in both orthogonal planes. Six sensor positions are chosen, located on a radius of $r/R = 0.87$ at different angles ϕ displayed in Figure 4.3(b). A sequence of velocity profiles recorded consecutively during 120 s is used to illustrate the spatial-temporal flow shown in Figure 4.15, for the case of an ordinary bubble plume at a gas flow rate of 0.83 cm^3/s. In the flow of $Ha = 0$, a permanent downward flow can be observed in a zone from about 30 to 70 cm below the free surface. Occasionally, this zone is stretched towards the central part of the fluid cylinder, whereas in the bottom part a weak ascending motion can be observed. Apart from local velocity fluctuations, the global flow pattern appears to be stationary. Figure 4.15(b) displays the

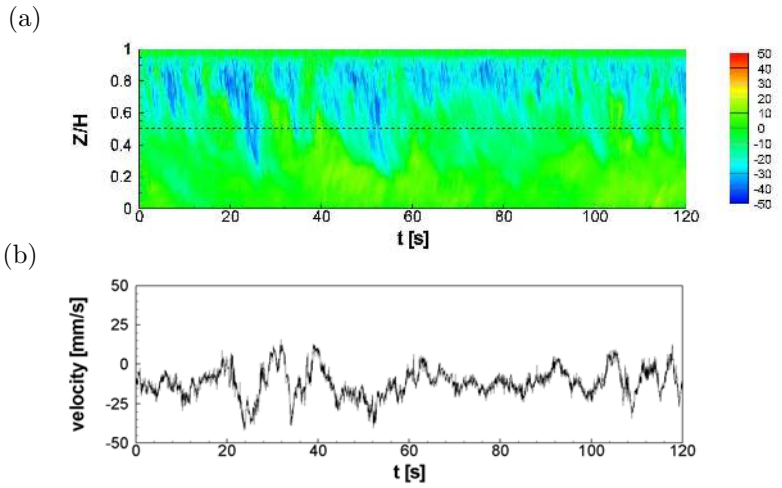

Figure 4.15: Vertical velocity measured along a vertical line at $r/R = 0.87$, $\phi = 0$, $Q_g = 0.83\ cm^3/s$ and $Ha = 0$: (a) the spatiotemporal distribution; (b) selected time series at the position $Z/H = 0.5$. The color bar denotes the velocity in mm/s.

velocity time series obtained at $z/H = 0.5$ mm, which is also marked as black horizontal line in Figure 4.15(a).

The magnetic field modifies the time variations of global flow structures distinctively. Figure 4.16 contains the spatial-temporal plots of the fluid velocity for Ha numbers of 162, 271 and 484. In Figure 4.16(a), the velocity profiles show two separate regions with a predominantly descending flow. A strong flow with negative velocities moves from the free surface downwards at intervals. At approximately the mid-height of the container, the flow returns abruptly to the location of departure. As shown in the figure, the domains of the downward flows are reciprocally paired with localized upward flow zones. In the perpendicular plane, it becomes clear that a recirculation zone is established with the maximum values for the downwards flow around the container mid-height. Similar patterns with an opposite sign of the velocity appears, in the parallel plane at $\phi = \pi/2$ as shown in Figure 4.16(b). The flow pattern changes when Ha is increased. However, it can be noted that no steady flow is achieved.

The existence of low-frequency flow structures is also reflected by the velocity time series in Figure 4.17, which are obtained at $z/H = 0.5$. The periodic time of the velocity signals recorded at $Ha = 162$ is about 30 s. Obviously, both the periodic time and the amplitude of the low-frequency oscillations decline as Ha increases. The averaged magnitude of the velocity increases in the parallel plane as Ha increases, whereas the temporary values oscillate between zero and a maximum value.

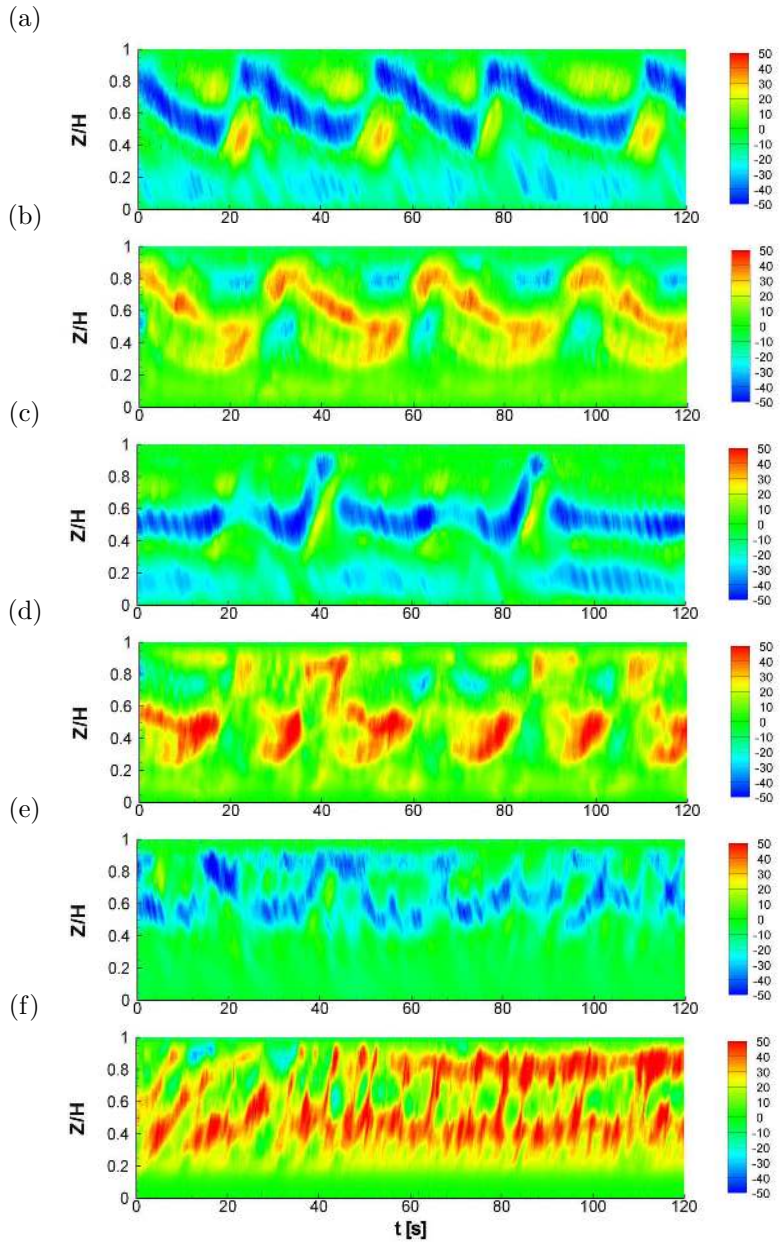

Figure 4.16: Spatiotemporal distributions of the vertical velocity component along a vertical line at various Hartmann numbers: (a) & (b): $Ha = 162$; (c) & (d): $Ha = 271$; (e) & (f): $Ha = 484$. The figures (a), (c), (e) depict the flow in the perpendicular plane; and (b), (d), (f) depict the flow in the parallel plane. (Q_g=0.83 cm^3/s) The color bar denotes the velocity in mm/s.

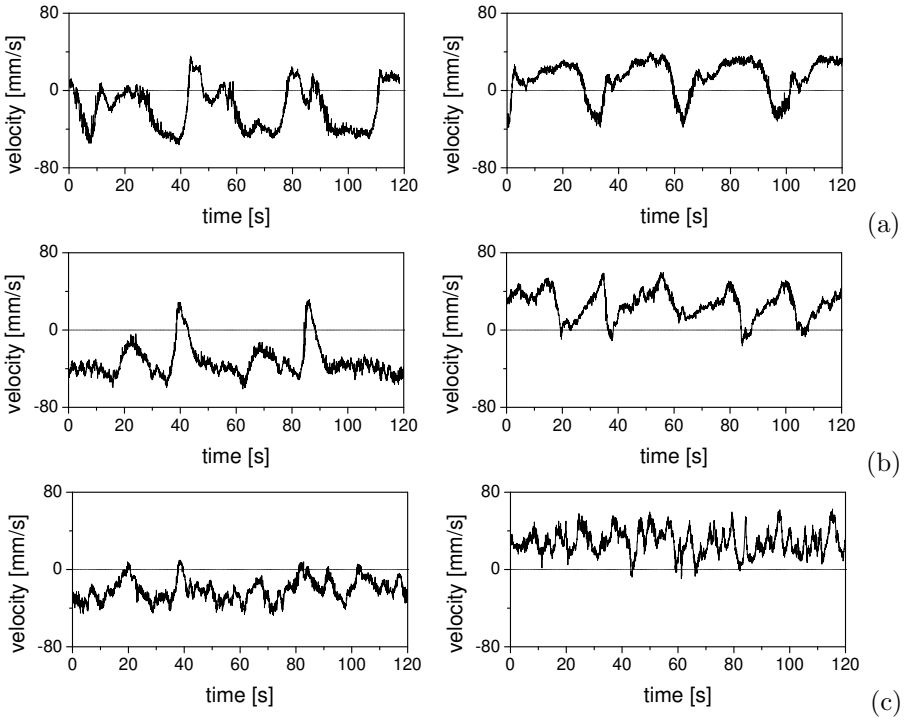

Figure 4.17: Time series of the vertical velocity component at different Hartmann numbers: (a) $Ha = 162$; (b) $Ha = 271$; (c) $Ha = 484$. The left hand side figure presents the flow in the perpendicular plane; the right hand side one presents the flow in the parallel plane. The data were acquired at the position $r/R = 0.87$, $Z/H = 0.5$ applying a gas flow rate of Q_g=0.83 cm^3/s.

Measurements at different gas flow rate were performed in the range Q_g=0.33-3.67 cm^3/s. The results show that the observed phenomena are similar and the trends already described can be generalized. As a second example, we present results at a gas flow rate of Q_g=3.67 cm^3/s. Figures 4.18, 4.19 and 4.20 show the spatio-temporal structures, the local time series and the corresponding frequency spectra calculated using FFT for the same set of Hartmann numbers as used in Figures 4.16 and 4.17. At this gas flow rate, distinct similarities can be noticed considering the spatial-temporal flow structures in both planes ($\phi = 0$ and $\phi = \pi/2$). Very regular oscillations are found at $Ha = 162$ in the perpendicular plane. Zones with strong descending flow appear periodically beneath the free surface and move continuously towards the bottom of the container.

The power spectra of the time series recorded at $Ha = 162$ in Figure 4.19 and Figure 4.20 reveal frequency peaks at 0.127 Hz and 0.131 Hz, respectively. Increasing the Hartmann number to $Ha = 271$ creates another flow pattern. Regions with alternating ascending and

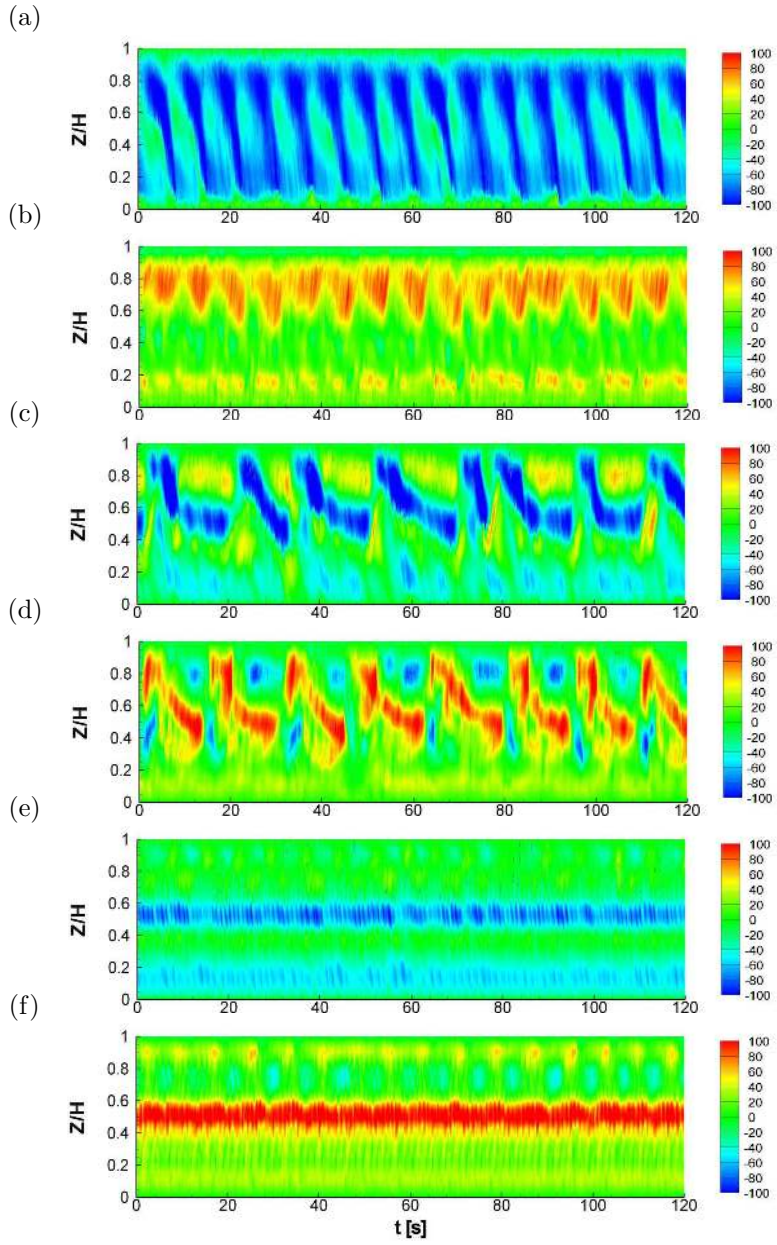

Figure 4.18: Spatiotemporal distributions of the vertical velocity along a vertical line at various Hartmann numbers: (a) & (b) $Ha = 162$; (c) & (d) $Ha = 271$; (e) & (f) $Ha = 484$. The figures (a), (c), (e) depict the flow in the perpendicular plane; and (b), (d), (f) depict the flow in the parallel plane. (Q_g=3.67 cm^3/s). The color bar denotes the velocity in mm/s.

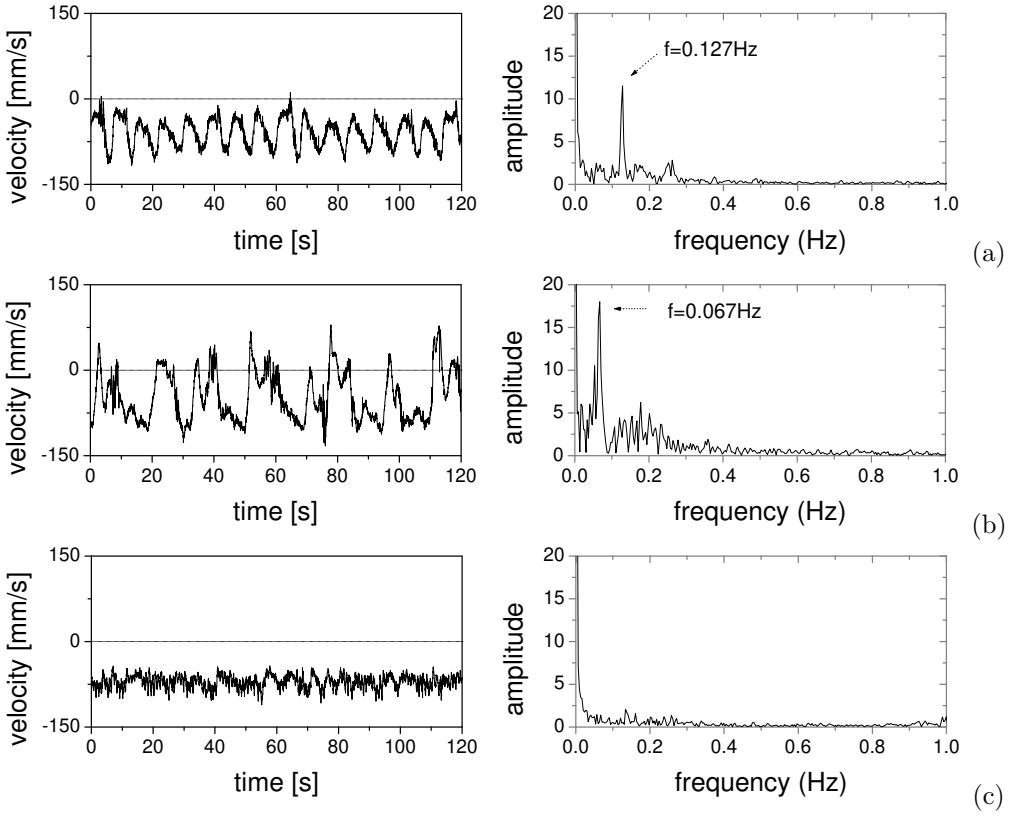

Figure 4.19: Velocity time series and corresponding FFT spectra of the vertical velocity component at different Hartmann numbers in the plane perpendicular to **B**: (a) $Ha = 162$; (b) $Ha = 271$; (c) $Ha = 484$. The data were acquired at the position $r/R = 0.87$, $Z/H = 0.5$ applying a gas flow rate of Q_g=3.67 cm^3/s.

descending fluid motion emerge. The FFT of the time series shows a distinct peak at 0.067 Hz for the time series in both planes. The large-scale fluctuations disappear almost completely when $Ha \sim 484$. Here, stable zones of descending (perpendicular plane) or ascending (parallel plane) flows appear. Consequently, no dominant frequency peaks can be identified in the FFT spectra. It is worth to point out that the maximum amplitude of the velocity oscillations is found at $Ha = 271$. The time-averaged velocity even increases in the case of the highest magnetic field strength ($Ha = 484$), although the amplitude of the large-scale oscillations is substantially damped. Figure 4.21 shows the dominant frequencies determined from the power spectra of the velocity time series at different gas flow rates. It can be noticed that increasing the gas flow rate leads to higher frequencies in general.

Further measurements are carried out at Q_g=3.67 cm$^3/s$ and $Ha = 271$, where vertical velocities are simultaneously measured at different azimuthal locations ϕ on a circle of $r/R =$

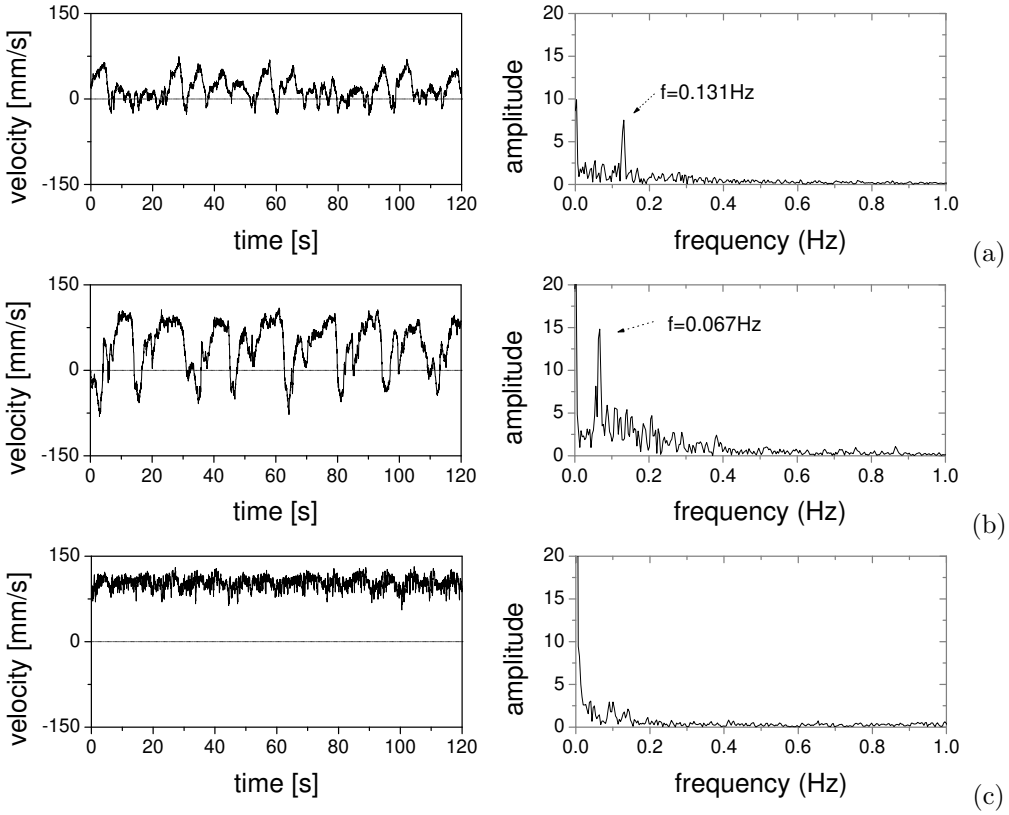

Figure 4.20: Velocity time series and corresponding FFT spectra of the vertical velocity component at different Hartmann numbers in the plane parallel to **B**: (a) $Ha = 162$; (b) $Ha = 271$; (c) $Ha = 484$. The data were acquired at the position $r/R = 0.87$, $Z/H = 0.5$ applying a gas flow rate of Q_g=3.67 cm^3/s.

0.87 (see Figure 4.3b). All the velocity time series are obtained at a height of $z/H = 0.77$. Auto- and cross-correlation functions are calculated according to the following formulas

$$R(\phi_1, \phi_1, \tau) = \frac{\overline{u(\phi_1, t) \cdot u(\phi_1, t+\tau)}}{\overline{u(\phi_1, t)^2}} \tag{4.2}$$

$$R(\phi_1, \phi_2, \tau) = \frac{\overline{u(\phi_1, t) \cdot u(\phi_2, t+\tau)}}{\sqrt{\overline{u(\phi_1, t)^2} \cdot \overline{u(\phi_2, t)^2}}} \tag{4.3}$$

Simultaneous measurements of the vertical velocity are performed at

1. $\phi = 0$ and $\phi = \pi$,
2. $\phi = \pi/4$ and $\phi = 3\pi/4$,
3. $\phi = -\pi/4$ and $\phi = -3\pi/4$,
4. $\phi = 0$, $\phi = \pm\pi/4$ and $\phi = \pi/2$

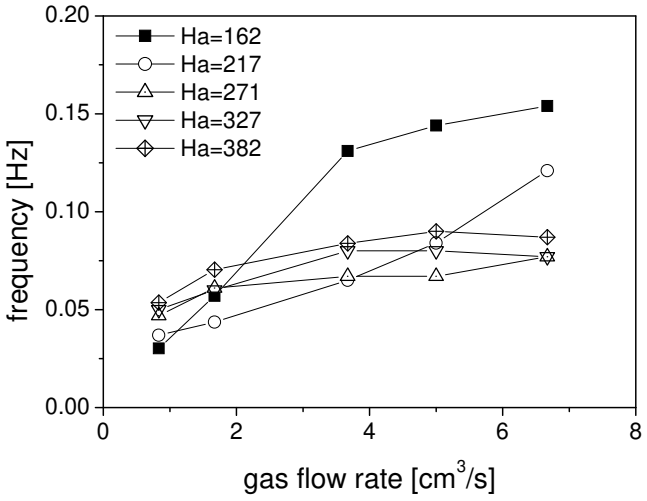

Figure 4.21: Predominant frequency of the vertical velocity at different gas flow rates and various Hartmann numbers. The measurements were performed in the perpendicular plane at $r/R = 0.87$, $Z/H = 0.5$ applying a gas flow rate of Q_g=3.67 cm^3/s.

which allow us to examine the relation of the velocity time series along chordal lines parallel to and across the magnetic field lines respectively. If the magnetic field causes an elongation and alignment of the flow structures in the direction of the applied magnetic field (Davidson 1995), a high degree of correlation should be found regarding to the velocity signals obtained at chords aligned with the field lines. In fact, the comparison between auto-correlation functions calculated at $\phi = \pm\pi/4$ and cross correlation functions $R(\pi/4, 3\pi/4)$ and $R(-\pi/4, -3\pi/4)$, respectively, demonstrates an almost perfect agreement, as shown in in Figure 4.22. Regular oscillations occur showing a periodicity of about 16 s. The velocity time series obtained at ϕ = 0 and $\phi = \pi$ are also found to be highly correlated. At a first view, it might be surprising that the correlation along the diameter is less remarkable than those along the parallel chords. This can be understood if we take into account of the existence of the bubble plume in the center of the container, which might disturb the spreading of momentum along the magnetic field lines and, therefore, are responsible for the weak distortion of the correlation function along the diameter. Another evident feature is the appearance of another oscillating mode leading to a doubling of the frequency, as shown in Figure 4.22(c).

This twofold frequency also can be recognized in Figure 4.23, which shows the velocity time series at $\phi = 0$, $\phi = \pi/2$, as well as $\phi = \pm\pi/4$. Related auto-correlation and cross-correlation coefficients can be found in Figure 4.24. All four time series in Figure 4.23 exhibit oscillations with a dominating periodicity of around 16s. It corresponds to a frequency of 0.06 Hz approximately, which is confirmed by prominent peaks in the spectra (not shown here).

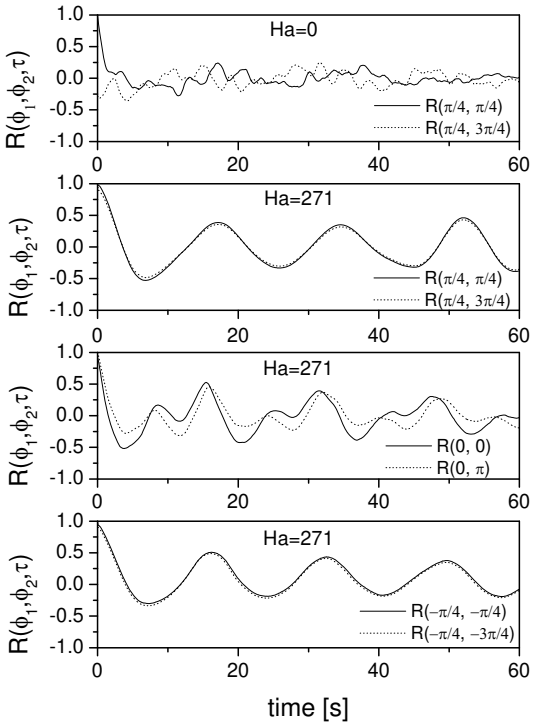

Figure 4.22: Correlation coefficients of the vertical velocity component along the direction of the magnetic field lines. (—·— denotes the auto-correlation coefficient; ····· denotes the cross-correlation coefficient.) All data were simultaneously measured at the position $r/R = 0.87$, $Z/H = 0.77$ applying a Hartmann number of $Ha = 271$ and a gas flow rate of Q_g=3.67 cm^3/s.

The velocity series at $\phi = \pi/2$ and $\phi = \pi/4$ show a positive concurrence, whereas the time series obtained at $\phi = \pm\pi/4$ are negatively correlated. This means that, in the magnetic field, the fluid motion becomes uniform along the field lines. The half volumes on both sides of the parallel midplane are filled with large-scale flow structures which are oriented parallel to the magnetic field lines. The position of these vortices changes with time. A further question remains concerning the temporal relations between the flow structures in the half volumes on both sides of the parallel midplane, respectively. As shown in Figure 4.24, velocity time series recorded at $\phi = \pi/4$ and $\phi = -\pi/4$ are in anti-phase, which indicates a reciprocal succession with a phase lag of a half period. The amplitude of velocity oscillations at $\phi = 0$ is considerably smaller compared to those at the other three measuring positions. Here, the flow is mainly ascending. The originally downward flow is reversed by the electromagnetic force. In addition to the primary oscillation, another periodicity of about 8s is manifested by smaller velocity peaks. The comparison between the time series in Figure 4.23 shows that

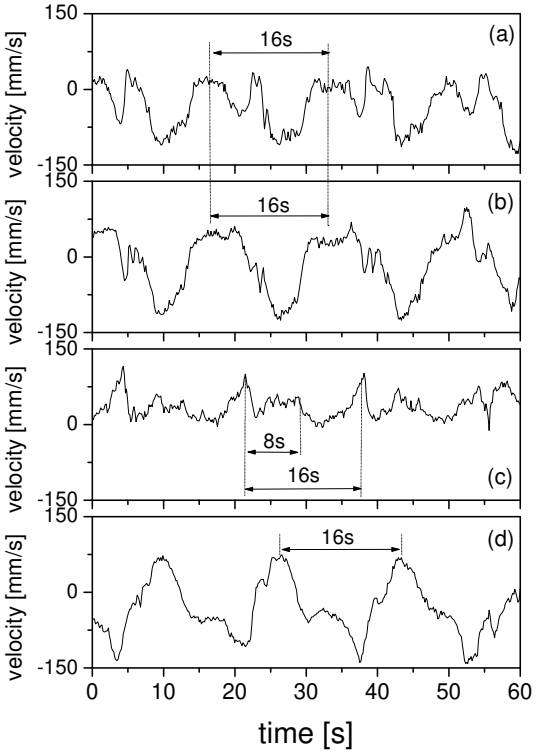

Figure 4.23: Time series of the vertical velocitiy component at different angular positions across the magnetic field lines: (a) $\phi = \pi/2$; (b) $\phi = \pi/4$; (c) $\phi = 0$; (d) $\phi = -\pi/2$. The velocities were simultaneously measured at the position $r/R = 0.87$, $Z/H = 0.77$ applying a Hartmann number of $Ha = 271$ and a gas flow rate Q_g=3.67cm^3/s.

the peaks of ascending flow at $\phi = 0$ correspond at any time to a maximum of descending flow at $\phi = \pm\pi/4$. The interlaced progression of vortices, with a periodicity of about 16 s, in both half volumes should be registered at the midplane with a time shift of 8s. However, it is worth noting that, along the entire height of the fluid vessel, this twofold frequency could not be so clearly identified at all vertical positions. This indicates that the flow symmetry is not perfect with respect to the midplane parallel to the magnetic field. Although the vortical structures at both sides of the parallel midplane can be traced at $\phi = 0$ at several heights, the velocity variations recorded in other regions of the parallel plane are exclusively governed by the vortices of either of both half volumes. Then, only a single peak of 0.06 Hz appears in the spectra.

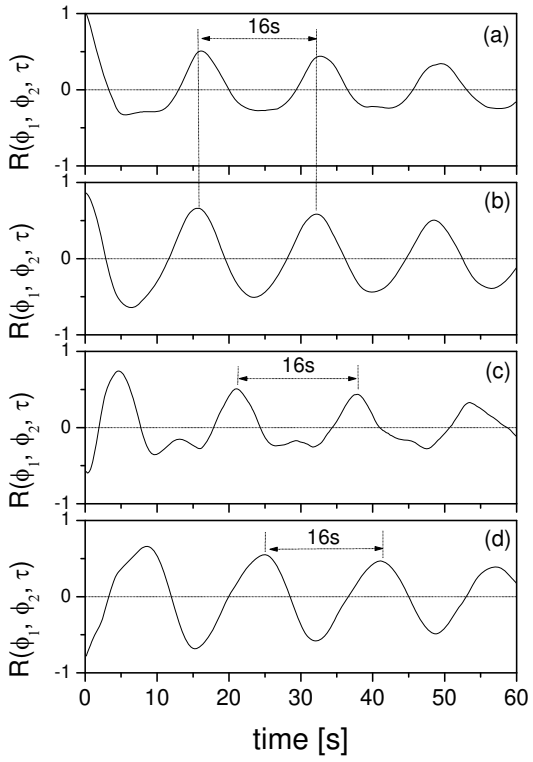

Figure 4.24: Correlation coefficients of the vertical velocity component corresponding to the velocity time series in Figure 4.23: (a) autocorrelation coefficient $R(\pi/2, \pi/2)$ at $\phi = \pi/2$; (b) cross-correlation coefficient $R(\pi/4, \pi/2)$ at $\phi = \pi/4$; (c) cross-correlation coefficient $R(0, \pi/2)$ at $\phi = 0$; (d) cross-correlation coefficient $R(-\pi/4, \pi/2)$ at $\phi = -\pi/4$.

4.4 Summary and discussion

In this chapter, we study the flow induced by a bubbly jet in a cylinder exposed to either a longitudinal or a transverse magnetic field. The results in the longitudinal field show that the flow is damped and stabilized. However, some seemingly surprising phenomena are found in the case of a transverse magnetic field. The flow is destabilized by the magnetic field, as shown by the spatial-temporal distributions of the velocity in the cylinder. Such phenomena deserve further discussions.

Davidson (1995) considered the generic problem of jet in a transverse magnetic field, as shown in Figure 4.1. The velocity profile of the jet is calculated by Davidson (1995) and shown in Figure 4.25. Originally stagnant fluid along the field lines is set into upward motion, whereas reverse flows appear on the both left and right hand sides of the jet.

These general features with respect to the reorganization of the flow pattern are also observed in our experiment of a bubbly jet, for instance, as shown in Figure 4.11 and Figure

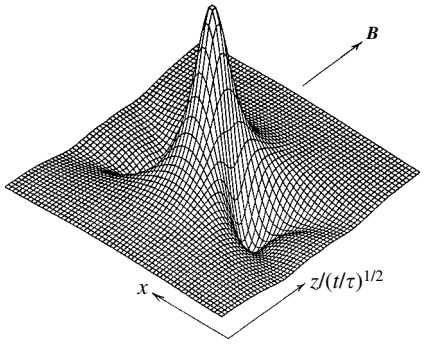

Figure 4.25: The change of a jet in a transverse magnetic field in an infinite domain. Note the negative flows on both sides of the jet as well as the ascending flows along the magnetic field lines. The picture is taken from Davidson (1995) and Davidson (2001).

4.12. In the bubble-plume-driven flow, the transverse magnetic field promotes an ascending flow and suppresses descending flows in the plane parallel to the field lines, whereas an inverse situation is found in the plane perpendicular to the field lines. The variation of the velocity along the magnetic field lines decreases considerably, which indicates the development of quasi-two-dimensional flow structures as already known from MHD theory, see for example Alemany et al. (1979) and Sommeria & Moreau (1982). We estimate the ratio of the electromagnetic force to the inertial force by calculating the interaction number N. At Q_g=3.67 cm^3/s, the typical velocity in the flow is $U_l \sim 200$ mm/s, which is the liquid velocity in the center of the bubble plume. This leads to $Re \sim 2.4 \times 10^4$ based on the length scale of the container radius. Therefore, we have $N \sim 1$ for $Ha = 162$. For the highest Hartmann number of $Ha = 484$, we have $N \sim 10$, which shows that significant modifications of the flow can be expected. In the current experiment, the fluid motion is dominated by large-scale flow structures that elongated along the direction of the magnetic field. Such flow structures cover the entire chord lengths of the cylinder cross-section, as shown in Figure 4.22.

Comparable flows are found on both sides of the bubble plume. The two-dimensional flow structures travel periodically in the vertical direction. Furthermore, there is a phase lag which equals to half of a period, between these flow structures on both sides of the bubbly jet. When Ha remains moderate, the vertical positions of these vortices oscillate periodically, as shown in Figure 4.23 and Figure 4.24. At higher Ha, the location of these recirculating zones becomes frozen. However, the resulted mean velocities of the flow are not necessarily smaller, see for example Figure 4.19 and Figure 4.20. A global damping of the flow is only observed at a very small gas flow rate and the maximum magnetic field, which gives $N \sim 50$.

The large-scale flow structures in the present work can explain the intensification of the

convective heat transfer as observed in MHD thermal convection by Authie et al. (2003), Burr & Müller (2002); Burr et al. (2003) at moderate Hartmann numbers. At sufficiently high Hartmann numbers, the vertical motion of the vortical structures will be suppressed, which is associated with a reduction of the transfer properties. It becomes apparent that detailed measurements of the flow structure are also essential to fully understand the transport of scalar quantities, as for heat transfer phenomena.

The question concerning the mechanism for the formation of the observed large-scale structures remains difficult. The magnetic field primarily influences the liquid flow structure, but the driving force of the flow, i.e. the plume of the rising gas bubbles, is affected too. Therefore we cannot definitely conclude that the reinforced large-scale velocity fluctuations appearing in a particular range of Hartmann numbers represent a universal feature connected with the application of a DC magnetic field to any originally isotropic flow. On the other hand, an acceleration of the liquid phase might be realized by increasing of the gas flow rate, too. However, in our experiment it was not possible to initiate the traveling vortex structures at any gas flow rate as long as the magnetic field was zero. The aforementioned studies concerning the heat transfer in MHD flows, see Authie et al. (2003); Burr & Müller (2002); Burr et al. (2003), suggest that the flow behaves in a similar manner. In contrast to an MHD flow in a straight channel, here we also have a free-developing flow; thus the phenomenon considered might be typical for the application of a DC magnetic field on free convection. In the case of the bubble plume, the flow is turbulent, showing velocity fluctuations on different length scales. It is well known that, due to the Joule dissipation, three-dimensional flow structures are quickly changed, whereas turbulent elements can survive if their vorticity is aligned with the direction of the magnetic field. Now it has been shown that under certain conditions these structures can also be amplified by a transfer of momentum leading to a reinforcement of velocity fluctuations, as observed in our experiment.

Local measurements of the bubble number using the conductance probes showed a periodic movement of the bubble plume along the container diameter perpendicular to the magnetic field, with a similar frequency as found to be typical for the detected velocity oscillations. This fact indicates a mutual interaction between the bubble plume and the traveling large-scale flow structures. The flow structures produce variations of the dynamic pressure, which are responsible for the wandering motion of the bubble plume in the two-phase system.

Such coupled oscillations between the lateral motion of the bubble plume and the velocity of the surrounding liquid have also been found in a conventional air-water system. Becker et al. (1999) performed measurements in a cylindrical and a flat bubble column, respectively. The authors described the flow in the cylindrical vessel to be chaotic and not predictable.

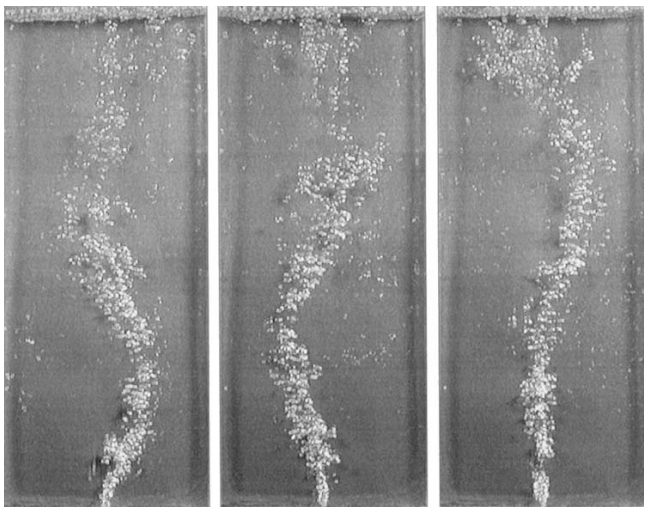

Figure 4.26: Snapshots of bubble plume motion in a two-dimensional flat container. The picture is taken from Becker et al. (1999).

The velocity time series contained a broad range of low-frequency contributions, but there was no characteristic frequency for the entire column. A meandering bubble plume was observed in a flat rectangular bubble column, as shown in Figure 4.26. The velocity series in this case exhibit undamped harmonic oscillations connected to staggered rows of vortices periodically moving downwards. The number of vortices increases with the liquid height, see Borchers et al. (1999). It is interesting to note that the application of a horizontal magnetic field on a bubble plume in a liquid column leads to a similar flow structure as known from flat bubble columns in ordinary hydrodynamics. In the latter case, the confinement of the container walls forced the flow to become two-dimensional leaving mainly one horizontal vorticity component. In the case of MHD the magnetic field causes quasi-two-dimesnional flow pattern. Moreover, the dominating frequency reported by Becker et al. (1999) is about 0.059 Hz, which is the same order of magnitude as found in our experiments. Naturally, the question arises of whether the same mechanism is responsible for the occurrence of the velocity oscillations in both cases. Further work could consider this similarity more explicitly.

The fact that a static magnetic field may give rise to non-steady, non-isotropic large flow structures could attain key importance in metallurgical engineering, especially, for the application of a DC magnetic field in the continuous casting process, where an electromagnetic brake of this kind is suggested to stabilize the flow field. The oscillations potentially arising within a range of moderate field intensity need to be taken into account for future activities regarding the process optimization by an electromagnetic brake.

Chapter 5

Summary

In this dissertation, laboratory experiments are carried out to study liquid metal flows driven by gas bubbles under the influence of a static magnetic field. We focus on the fundamental problems because they can be considered as prototypes of many two-phase flows in metallurgical engineering.

Chapter 1 provides the background for the current research work. Afterwards, we discuss the measuring technique for such two-phase flows in Chapter 2. Commercial measuring techniques for the special purpose of liquid metal flows do not exist, but in the recent literature several applications of the Ultrasound Doppler Velocimetry (UDV) are described. UDV allows to measure local velocity profiles in flows of opaque liquids. We adopted the measuring system DOP2000 to the needs of our liquid metal model experiments and used it throughout the experimental studies of this dissertation. The capability of DOP2000 is explored through several test problems. The settling velocities of single solid spheres in a stagnant liquid bulk were measured by UDV. The obtained results agree well with the standard drag coefficient curve of a sphere given in literature. The rising velocities of single gas bubbles in stagnant liquids, such as water or glycerin, were measured by UDV. The results were compared with other experimental data in literature and good agreements were achieved. A bubble-chain-driven flow in a transparent liquid was measured in parallel by UDV and a Laser Doppler Anemometer (LDA). Both instruments obtained the information of the liquid velocity along the bubble chain centerline. Working with a back scatter mode, the LDA gave directly the liquid-phase velocity. The results of UDV contained a mixture of the signals from the bubbles and the liquid along the whole centerline. A threshold method was developed to extract automatically the liquid velocity information. The obtained results agreed well with those obtained by the LDA. Thus, it was convincingly demonstrated that the UDV measurements allow to measure reliably liquid metal two-phase flows at low void fractions.

Liquid metal flows driven by a single rising bubble in either a vertical or a horizontal magnetic field are investigated in Chapter 3. The normal hydrodynamic case at $B = 0$ was investigated at the beginning. The terminal velocities of rising bubbles were measured by UDV and compared to the values predicted by the Mendelson equation, which is suitable for

pure liquids. The experimental data of UDV were slightly lower than the predicted values. The discrepancies can be explained by the fact that the GaInSn likely contained a small amount of impurities in the experiments. The vertical component of the bubble velocities displayed periodic oscillations, which indicate that the bubbles followed non-rectilinear trajectories as they rose up. The oscillation frequencies in the vertical direction were twice the frequencies in horizontal direction, as already found in the literature. A vertical (longitudinal) magnetic field affected the bubble rising velocity depending on the bubble size. The drag coefficients of smaller bubbles ($Eo = 2.2$ and 2.5) were increased as the magnetic interaction number N was about 1, whereas the drag coefficients of larger bubbles ($Eo = 3.4$, 4.9 and 6.6) were decreased in the same magnetic interaction number range. The amplitudes and frequencies of the bubble vertical velocities were both decreased. The vertical component of the liquid velocity induced by a rising bubble (bubble wake) was changed by the vertical magnetic field. In the region close to the bubble, the velocity magnitude was decreased; whereas in the far region, the liquid velocity was increased. The decay of velocity in the magnetic field became slower in comparison to the case without field. This was explained as a process of spreading of momentum along the magnetic field lines. A horizontal (transverse) magnetic field changed the bubble motion in a different way. The drag coefficients of the bubbles with $Eo = 2.7$, 4.1 and 4.4 were decreased when $N < 1.5$; whereas the drag coefficients of the bubbles with $Eo = 5.9$, 6.4 and 6.9 were firstly decreased at around $N = 0.5$ and then increased when $N > 1$. The oscillation amplitudes of the bubble vertical velocity were effectively decreased. However, the oscillation frequencies were increased by the horizontal magnetic field. The vertical component of the liquid velocity was decreased everywhere in the bubble wake in the horizontal magnetic field. The decay of the liquid velocity became faster in comparison to the case without field. The differences in the velocity distribution and decay in the two field configurations were explained by taking into account of the non-isotropic damping effect of a static magnetic field.

Liquid metal flows driven by a bubble plume in either a vertical or a horizontal magnetic field are investigated in Chapter 4. The flow without magnetic field was measured as a basis for comparison. The bubble plume was injected at the bottom center of a cylindrical vessel. The velocity fields of the induced flow were measured in two orthogonal meridional planes. The results showed that the fluid was flowing upward in the cylinder center and flowing downward in the region close to the cylinder wall. The flow field can be considered as axisymmetric in a good approximation. A vertical magnetic field stabilized and damped the flow effectively. The temporal variations of the fluid velocity became smaller if the magnetic induction was increased. The velocity magnitudes were decreased, and the velocity

distributions along the magnetic field lines were smoothed. The flow field keeps the axisymmetric distribution. A horizontal magnetic field destabilized and enhanced the flow within a range of moderate magnetic induction values. The flow became non-axisymmetric due to the non-isotropic influence of the magnetic field. In the meridional plane parallel to the field lines, the flow changed its direction from downward to upward. In comparison, enhanced downward flows were observed in the meridional plane perpendicular to the field lines. The flows in both planes became oscillating periodically within a range of moderate magnetic induction values. Whereas the damping influence of the vertical magnetic field on the bubble plume driven melt flow is fully as expected, the serious change of the flow in a horizontal magnetic field may be considered as surprising. It is for the first time here that such a destabilizing action of an external DC magnetic field on a liquid metal flow is experimentally demonstrated and investigated in detail. These results may have a significant impact on the application of steady electromagnetic brakes in metals processing, as it is already in use in the steel casting of thin slabs. The generally assumed damping action of such a brake on the liquid metal two-phase flow in the nozzle or the mold of this process, which was never experimentally tested up to now, may in reality appear in a totally different influence of the magnetic brake. The basic experiments performed in frame of the present dissertation give a strong hint into this direction and manifest very clearly that related experiments with careful velocity measurements are indispensable for a better understanding of complex liquid metal two-phase flows under the influence of external magnetic fields.

Appendices

A.1 The Lorentz force derived by Sommeria & Moreau

The equation (1.13) can be derived in the way shown in Robbert (1967). We start with the Faraday's law and the Ampére' law

$$\nabla \times \mathbf{E} = -\frac{\partial \mathbf{B}}{\partial t} \tag{1}$$

$$\nabla \times \mathbf{B} = \mu \mathbf{J} \tag{2}$$

where μ is the permeability of the fluid. In equations (1) and (2), the magnetic field $\mathbf{B}$ is a superposition of the imposed static field $\mathbf{B_0}$ and the induced magnetic field $\mathbf{b}$; namely

$$\mathbf{B} = \mathbf{B_0} + \mathbf{b} \tag{3}$$

Note that the induced $\mathbf{b}$ is only considered inside this Appendix. In the other parts of the thesis, we use $\mathbf{B}$ to represent the imposed magnetic field which is uniform and static.

The Lorentz force in equation (1.6) can be written as

$$\mathbf{J} \times \mathbf{B} = \frac{1}{\mu}(\nabla \times \mathbf{B}) \times \mathbf{B} = (\mathbf{B} \cdot \nabla)(\mathbf{B}/\mu) - \nabla(\mathbf{B}^2/2\mu) \tag{4}$$

by using the following identity

$$\nabla(\mathbf{B}^2/2) = (\mathbf{B} \cdot \nabla)\mathbf{B} + \mathbf{B} \times \nabla \times \mathbf{B} \tag{5}$$

Therefore, the Navier-Stokes equation (1.8) can be written as

$$\frac{\partial \mathbf{u}}{\partial t} + (\mathbf{u} \cdot \nabla)\mathbf{u} = -\frac{1}{\rho} \nabla P + \nu \nabla^2 \mathbf{u} + \frac{1}{\mu\rho}(\mathbf{B} \cdot \nabla)\mathbf{B} \tag{6}$$

where the gradient term ∇P includes $\nabla(\mathbf{B}^2/2\mu)$.

Now equation (3) can be substituted into the last term in equation (6) and the second-order term $(\mathbf{b} \cdot \nabla)\mathbf{b}$ can be neglected. When $\mathbf{B_0}$ is uniform and lies in the z direction, equation (6) becomes

$$\frac{\partial \mathbf{u}}{\partial t} + (\mathbf{u} \cdot \nabla)\mathbf{u} = -\frac{1}{\rho} \nabla P + \nu \nabla^2 \mathbf{u} + \frac{B_0}{\mu\rho} \frac{\partial \mathbf{b}}{\partial z} \tag{7}$$

where B_0 represents the magnetic induction of the imposed field.

On the other hand, if we take the curl of equation (1.3) and replace $\mathbf{J}$ and $\mathbf{E}$ using equations (1) and (2), there is

$$\nabla \times \nabla \times \mathbf{B} = \mu\sigma_e \left(-\frac{\partial \mathbf{B}}{\partial t} + \nabla \times (\mathbf{u} \times \mathbf{B}) \right) \tag{8}$$

which can be further written as

$$\frac{\partial \mathbf{B}}{\partial t} = (\mathbf{B} \cdot \nabla)\mathbf{u} - (\mathbf{u} \cdot \nabla)\mathbf{B} + \frac{1}{\mu\sigma_e}\nabla^2\mathbf{B} \tag{9}$$

Under the condition of $R_m \ll 1$, we adopt the quasi-static theory and equation (9) becomes

$$0 = (\mathbf{B} \cdot \nabla)\mathbf{u} - (\mathbf{u} \cdot \nabla)\mathbf{B} + \frac{1}{\mu\sigma_e}\nabla^2\mathbf{B} \tag{10}$$

Similarly, we substitute equation (3) into equation (10) and neglect the second-order term $\mathbf{u} \times \mathbf{b}$, there is

$$0 = (\mathbf{B_0} \cdot \nabla)\mathbf{u} - (\mathbf{u} \cdot \nabla)\mathbf{B_0} + \frac{1}{\mu\sigma_e}\nabla^2(\mathbf{B_0} + \mathbf{b}) \tag{11}$$

Namely

$$B_0 \frac{\partial \mathbf{u}}{\partial z} + \frac{1}{\mu\sigma_e}\nabla^2\mathbf{b} = 0 \tag{12}$$

The induced $\mathbf{b}$ can be written symbolically as

$$\mathbf{b} = -\mu\sigma_e B_0 \nabla^{-2} \frac{\partial \mathbf{u}}{\partial z} \tag{13}$$

Combining equations (13) and (7), we have

$$\frac{\partial \mathbf{u}}{\partial t} + (\mathbf{u} \cdot \nabla)\mathbf{u} = -\frac{1}{\rho}\nabla P + \nu\nabla^2\mathbf{u} - \frac{\sigma_e B_0^2}{\rho}\nabla^{-2}\frac{\partial^2 \mathbf{u}}{\partial z^2} \tag{14}$$

where the last term is the same as equation (1.13).

A.2 Doppler frequency

Consider a wave whose actual speed and frequency are c and f_e, respectively. The wave is perceived by a receiver with a frequency of f_r in the following form

$$f_r = f_e \left(\frac{c \pm u_r}{c \mp u_e} \right) \tag{15}$$

where u_r and u_e are the speed of the receiver and the emitter, respectively; in fact, they are the velocity components projected on the line which links the receiver and emitter. The signs of plus (+) and minus (−) are decided by the convention that the perceived frequency f_r is higher than the actual frequency f_e if the emitter and the receiver move toward each other.

When an ultrasound emitter is fixed at a location and a reflecting particle moves with a speed u towards the emitter, the frequency (f_{r1}) perceived by the particle takes the following form

$$f_{r1} = f_e \left(\frac{c+u}{c} \right) \tag{16}$$

Afterwards, the emitter receives the reflected wave from the particle with the frequency f_r (note that the wave is now emitted by the particle with a frequency of f_{r1}), which is

$$f_r = f_{r1} \left(\frac{c}{c-u} \right) = f_e \left(\frac{c+u}{c-u} \right) \tag{17}$$

As a result, the Doppler frequency f_d (or the Doppler shift) perceived by the emitter is given by

$$f_d = f_r - f_e = f_e \left(\frac{2u}{c-u} \right) \tag{18}$$

Under the condition of $c \gg u$, we have the simplified form

$$f_d = \frac{2u}{c} f_e \tag{19}$$

which is the same as equation (2.3).

A.3 The phase shift & Doppler shift

The conventional calculation of velocity from the Doppler frequency, shown as equation (2.3), can be derived from equation (2.8). This is discussed by Atkinson & Woodcock (1982) in the following way. If we differentiate both sides of equation (2.8), we have

$$\frac{d\delta}{dt} = 2\pi f_e \cdot \frac{d(\Delta t)}{dt} \tag{20}$$

Since the frequency is defined as the change rate of the phase φ with time, the change rate of the phase difference, δ, is the frequency difference between the received echo and the transmitted wave. The frequency difference actually is the Doppler shift frequency, f_d; namely, the left hand side of equation (20) is

$$\frac{d\delta}{dt} = 2\pi f_d \tag{21}$$

The right hand side of the equation (20) can be reformulated. If we denote the distance between the particle and the transducer as z, and take into account the fact that $\Delta P \ll z$, we have

$$\frac{d(\Delta t)}{dt} = \frac{d}{dt} \left(\frac{2z}{c} \right) = \frac{2}{c} \frac{dz}{dt} = \frac{2}{c} u \tag{22}$$

so equation (2.8) actually shows

$$2\pi f_d = 2\pi f_e \cdot \frac{2u}{c} \tag{23}$$

in fact, this is the same as equation (2.3).

In convention, the instruments using either of the methods are all called ultrasound Doppler devices in literature, see Jensen (1996).

Acknowledgements

The research work was conducted at Magnetohydrodynamic Department in Forschungszentrum Dresden-Rossendorf where I have been working as a PhD candidate since 2002. It would be impossible for me to finish this dissertation without the help from my colleagues.

Taking this opportunity, I sincerely thank Dr Gunter Gerbeth for kindly providing me an opportunity to study in the group, as well as his consistent guidance and support during the past years. Dr Gerbeth has encouraged me to pursue my studies in fluid mechanics and provided excellent experiment facilities for my work. I have benefited significantly from the pleasant research environment of our MHD group. I am also sincerely grateful to my supervisor in Rossendorf, Dr Sven Eckert, for his great help since I have been working here. I started as a freshman in the MHD Department. Dr Eckert has given me uncountable academic guidance from experimental skills to scientific writings. He is always happy to offer his help and provide his advices with great patience whenever I turn to him. He always reads the manuscripts of our paper carefully and goes to great effort to significantly improve them. I would also like to thank Dr Tom Weier, with whom I share the same office. Dr Weier has helped me to conduct measurements using Laser Doppler Anemometry during my first year in Rossendorf; since then I have had many beneficial discussions with him concerning fluid mechanics and experiment techniques, such as hot-wire and hot-film anemometry. My thanks are also given to Thomas Gundrum, from whom I have received consistent and highly efficient assistances concerning electromagnetic fields and other experimental facilities. His enthusiasm and fun in experiments have deeply impressed me. I have learned a lot from the discussions with Dr Victor Shatrov and Dr Gerd Mutschke concerning the flow problems of cylinders, spheres and bubbles, and I have also learned a lot from the discussions with Dr Josef Pal concerning electric potential probes and electric conductance probes. I would like to thank Dr Janis Priede for so many beneficial and pleasant discussions. Dr Priede is always able to give me helpful suggestions within an amazingly short time, whether my questions are concerning unexpected experimental phenomena or seemingly controversial discussions in the literature. Besides my dissertation, Dr Priede also helped me by reading critically our manuscripts of the bubble-plume-driven flow before it was submitted, and he

gave us many constructive comments. I would like to thank Dr Ilmars Grants. We have worked closely for more than one year and had many fruitful discussions and experiment results. I have learned a lot from Dr Grants concerning MHD flows driven by alternating magnetic fields as well as the fluid mechanics aspects of a tornado. I am also in debt to Dr Vladimir Galindo for his consistent help concerning computers and to Dr Jürgen Hüller for his professional performance concerning the preparation of the liquid metal GaInSn. Equally, I am very grateful to Ms Bombis Doris for her help all the time and to my colleagues Bernd Nowak, Steffen Borchardt, Heiko Kunadt and Stephan Erlebach for their assistances to my experiments.

I would like to sincerely thank Professor Stefan Odenbach for being my supervisor in Technical University of Dresden, as well as his guidance during the measuring techniques course. In addition, I would like to thank his help and comment on my dissertation. Equally, I would like thank Professor Frank-Peter Weiss for being a referee of my dissertation, as well as his suggestions on my work and future plan. I have also benefited a lot from the institute seminars organized by him.

The dissertation uses the LaTeX template provided by Dr Robbert Whittaker. The research work is financially supported by the Deutsche Forschungsgemeinschaft (DFG) in the form of the collaborative research center SFB609 “Electromagnetic Flow Control in Metallurgy, Crystal Growth and Electrochemistry”.

Bibliography

Albrecht, H. E., Borys. M., Damaschke, N. & Tropea, C. 2003 *Laser Doppler and Phase Doppler Measurement Techniques*. Springer-Verlag.

Aleksandrova, S. & Molokov, S. 2004 Three-dimensional buoyant convection in a rectangular cavity with differently heated walls in a strong magnetic field. *Fluid Dyn. Res.* **35**, 37–66.

Alemany, A., Moreau, R., Sulem, P. & Frisch, U. 1979 Influence of an external magnetic field on homogeneous MHD turbulence. *J. Méc.* **18**, 277–313.

Andreev, O., Kolesnikov, Y. & Thess, A. 2007 Experimental study of liquid metal channel flow under the influence of a non-uniform magnetic field. *Phys. Fluids* **18**, 039902.

Andreini, R. J., Foster, J. S. & Callen, R. W. 1977 Characteriztion of gas bubbles injected into molten metals under laminar flow conditions. *Met. Trans.* **8B**, 625–631.

Andruszkiewicz, A. & Sommerlatt, H. D. 2008 Ultrasonic measurements of two-phase liquid-gas systems: the method of measurements. *Chem. Proc. Engng* **29**, 113–128.

Atkinson, P. & Woodcock, J. P. 1982 *Doppler Ultrasound and its Use in Clinical Measurement*. Academic Press.

Authie, G., Tagawa, T. & Moreau, R. 2003 Buoyant flow in long vertical enclosures in the presence of a strong horizontal magnetic field. Part 2. Finite enclosures. *Euro. J. Mech.B/Fluids* **22**, 203–220.

Aybers, N. M. & Tapucu, A. 1969 The motion of gas bubbles rising through stagnant liquid. *Wärme- und Stoffübertragung* **2**, 118–128.

Aybers, N. M. & Tapucu, A. 1969 Studies on the drag and shape of gas bubbles rising through a stagnant liquid. *Wärme- und Stoffübertragung* **2**, 171–177.

Batchelor, G. K. 1967 *An Introduction to FluidDynamics*. Cambridge.

Becker, S., De Bie, H. & Sweeney, J. 1999 Dynamic flow behaviour in bubble columns. *Chem. Engng Sci.* **54**, 4929–4935.

Bhaga, D. & Weber, M. E. 1981 Bubbles in viscous liquids: shapes, wakes and velocities. *J. Fluid Mech.* **105**, 61–85.

Boden, S., Eckert, S., Willers, B. & Gerbeth, G. 2008 X-Ray Radioscopic Visualization of the Solutal Convection during Solidification of a Ga-30 Wt Pct In Alloy. *Metall. Mater. Trans. A* **39**, 613–623.

Borchers, O., Busch, C., Sokolichin, A. & Eigenberger, G. 1999 Applicability of the standard k-ϵ turbulence model to the dynamic simulation of bubble columns. Part II: Comparison of detailed experiments and flow simulations. *Chem. Engng Sci.* **54**, 5927–5935.

Bradshaw, P. 1971 *An introduction to turbulence and its measurements*. Pergamon Press.

Brennen, C. E. 1995 *Cavitation and Bubble Dynamics*. Oxford University Press.

Breuer, K. S. 2005 *Microscale Diagnostic Techniques*. Springer-Verlag.

Brito, D., Nataf, H. C., Cardin, P., Aubert, J. & Masson,J. P. 2001 Ultrasonic Doppler velocimetry in liquid gallium. *Exp. Fluids* **31**, 653–663.

Bröring, S., Fischer, J., Korte, T., Sollinger S. & Lübbert, A. 1991 Flow structure of the dispersed gasphase in real multiphase chemical reactors investigated by a new ultrasound-Doppler technique. *Can. J. Chem. Engng* **69**, 1247–1256.

Brunke, O. & Odenbach, S. 2006 In situ observation and numerical calculations of the evolution of metallic foams. *J. Phys.: Condens. Matter* **18**, 6493–6506.

Bruun, H. H. 1995 *Hot-Wire Anemometry: Principles and Signal Analysis*. Oxford University Press.

Brücker, C. 1999 Structure and dynamics of the wake of bubbles and its relevance for bubble interaction. *Phys. Fluids* **11**, 1781–1796.

Burr, U. & Müller, U. 2001 Rayleigh-Benard convection in liquid metal layers under the influence of a vertical magnetic field. *Phys. Fluids* **13**, 3247–3257.

Burr, U. & Müller, U. 2002 Rayleigh-Benard convection in liquid metal layers under the influence of a horizontal magnetic field. *J. Fluid Mech.* **453**, 345–369.

Burr, U., Barleon, P., Jochmann, P. & Tsinober, A. 2003 Magnetohydrodynamic convection in a vertical slot with horizontal magnetic field. *J. Fluid Mech.* **475**, 21–40.

Búhler, L, Horanyi, S. & Mistrangelo, C. 2008 Interpretation of LEVI velocity signals in 3D MHD flows. *Fusion Engng Design* **83**, 1822–1827.

Cioni, S., Chaumat, S. & Sommeria, J. 2000 Effect of a vertical magnetic field on turbulent Rayleigh-Bénard convection. *Phys. Rev. E* **62**, R4520.

Clift, R., Grace, J. & Weber, M. 1978 *Bubbles, Drops and Particles*. Academic Press.

Chandrasekhar, S. 1981 *Hydrodynamic and Hydromagnetic Stability*. Dover.

Comte-Bellot, G. 1976 Hot-Wire Anemometry. *Annu. Rev. Fluid Mech.* **8**, 209–231.

Cramer, A., Zhang, C. & Eckert, S. 2004 Local structures in liquid metals measured by ultrasonic Doppler velocimetry. *Flow Meas. Instrum.* **15**, 145–153.

Cramer, A., Varshney, K., Gundrum, T. & Gerbeth, G. 2006 Experimental study on the sensitivity and accuracy of electric potential local flow measurements. *Flow Meas. Instrum.* **17**, 1–11.

Cramer, A., Pal, J. & Gerbeth, G. 2007 Experimental investigation of a flow driven by a combination of a rotating and a traveling magnetic field. *Phys. Fluids* **19**, 118109.

Cukierski, K. & Thomas, B. G. 2008 Flow control with local electromagnetic braking in continuous casting of steel slabs. *Metall. Mater. Trans. B* **39**, 94–107.

D'Ans, J. & Lax, E. 1992 *Taschenbuch für Chemiker und Physiker*. Springer.

Davidson, P. A. 1995 Magnetic damping of jets and vortices. *J. Fluid Mech.* **299**, 153–186.

Davidson, P. A. 2001 *An Introduction to Magnetohydrodynamics*. Cambridge.

Davis, R. & Taylor, G. I. 1950 The mechanics of large bubbles rising through extended liquids and through liquids in tubes. *Proc. R. Soc. London* **200**, 375–390.

Davoust, L., Cowley, M. D., Moreau, R. & Bolcato, R. 1999 Buoyancy-driven convection with a uniform magnetic field. Part 2. Experimental investigation. *J. Fluid Mech.* **400**, 59–90.

Duineveld, P. C. 1995 The rise velocity and shape of bubbles in pure water at high Reynolds number. *J. Fluid Mech.* **292**, 325–332.

Durst, F., Melling, A. & Whitelaw, J. H. 1981 *Principles and practice of laser-Doppler anemomentry*. Academic Press.

Eckert, S. 1998 *Experimentelle Untersuchung turbulenter Flüssigmetall- und Flüssigmetall-Gas-Strömungen in einem äusseren Magnetfeld*. PhD thesis, Technical University of Dresden, Dresden.

Eckert, S., Gerbeth, G. & Lielausis, O. 2000 The behavior of gas bubbles in a turbulent liquid metal magnetohydrodynamic flow. Part I: Dispersion in quasi-two-dimensional magnetohydrodynamic turbulence. *Intl J. Multiphase Flow* **26**, 45–66.

Eckert, S., Gerbeth, G. & Lielausis, O. 2000 The behavior of gas bubbles in a turbulent liquid metal magnetohydrodynamic flow. Part I: Dispersion in quasi-two-dimensional magnetohydrodynamic turbulence. *Intl J. Multiphase Flow* **26**, 45–66.

Eckert, S., Gerbeth, G. & Lielausis, O. 2000 The behavior of gas bubbles in a turbulent liquid metal magnetohydrodynamic flow. Part II: Magnetic field influence on the slip ratio. *Intl J. Multiphase Flow* **26**, 67–82.

Eckert, S., Witke, W. & Gerbeth, G. 2000 A new mechano-optical technique to measure local velocities in opaque fluids. *Flow Meas. Instrum.* **11**, 71–78.

Eckert, S., Gerbeth, G., Witke, W. & Langenbrunner, H. 2001 MHD turbulence measurements in a sodium channel flow exposed to a transverse magnetic field. *Intl J. Heat Fluid Flow* **22**, 358–364.

Eckert, S. & Gerbeth, G. 2002 Velocity measurements in liquid sodium by means of ultrasound Doppler velocimetry. *Exp. Fluids* **32**, 542–546.

Eckert, S., Gerbeth, G. & Melnikov, V. I. 2003 Velocity measurements at high temperatures by ultrasound Doppler velocimetry using an acoustic wave guide. *Exp. Fluids* **35**, 381–388.

Eckert, S., Nikrityuk, Petr A., Räbiger, D., Eckert, K. & Gerbeth, G. 2007 Efficient melt stirring using pulse sequences of a rotating magnetic field: I - Flow field in a liquid metal column. *Metall. Mater. Trans. B* **39**, 374–386.

Eckert, S., Cramer, A. & Gerbeth, G. 2007 Velocity Measurement Techniques for Liquid Metal Flows. *Magnetohydrodynamics - Historical evolution and trends, S. Molokov, R. Moreau and H.K. Moffat (eds.)*. Springer.

Ellingsen, K. & Risso, F. 2001 On the rise of an ellipsoidal bubble in water: oscillatory paths and liquid-induced velocity. *J. Fluid Mech.* **440**, 235–268.

Ern, P. & Wesfreid, J. E. 1999 Flow between time-periodically co-rotating cylinders. *J. Fluid Mech.* **397**, 73–98.

Fan, L. S. & Tsuchiya, K. 1990 *Bubble Wake Dynamics in Liquids and Liquid-Solid Suspensions*. Butterworth-Heinemann.

Gad-El-Hak, M. 1989 *Advances in Fluid Mechanics Measurements*. Spinger-Verlag.

Garner, F.H. & Hammerton, D. 1954 Circulation inside gas bubbles. *Chem. Sci. Engng* **3**, 1–11.

Gelfgat, Y. M. & Gelfgat, A. Y. 2004 Experimental and numerical study of rotating magnetic field driven flow in cylindrical enclosures with different aspect ratios. *Magneto-hydrodynamics* **40**, 147–160.

Goldstein, R. J. 1996 *Fluid Mechanics Measurements*. Tayler & Trancis.

Grants, I., Zhang, C., Eckert, S. & Gerbeth, G. 2008 Experimental observation of swirl accumulation in a magnetically driven flow. *J. Fluid Mech.* **616**, 135–152.

Griffiths, R. T. & Nicol, A. A. 1965 A fibre flowmeter suitable for very low flow rates. *J. Sci. Instrum.* **42**, 797–799.

Guet, S. & Ooms, G. 2006 Fluid mechanical aspects of the gas-lift technique. *Annu. Rev. Fluid Mech.* **38**, 225–249.

Haberman, M. & Morton, R. 1953 An experimental investigation of the drag and shape of air bubbles rising in various liquids. *David W. Taylor Model Basin Report Navy Dept., Washington, DC.* **802**.

Haberman, M. & Morton, R. 1954 An experimental study of bubbles moving in liquids. *American Society of Civil Engineers - Proceedings Separates* **80** No.387

Hadid, H. B., Henry, D. & Kaddeche, S. 1997 Numerical study of convection in the horizontal Bridgman configuration under the action of a constant magnetic field. Part I. Two-dimensional flow. *J. Fluid Mech.* **333**, 23–56.

Hadid, H. B. & Henry, D. 1997 Numerical study of convection in the horizontal Bridgman configuration under the action of a constant magnetic field. Part I. Three-dimensional flow. *J. Fluid Mech.* **333**, 57–83.

Harper, J. F. 1972 The motion of bubbles and drops through liquids. *Adv. Appl. Mech.* **12**, 59–129.

Hartunian, R. A. & Sears, W. R. 1957 On the instability of small gas bubbles moving uniformly in various liquids. *J. Fluid Mech.* **3**, 27–47.

Hill, J. C. & Sleicher, C. A. 1971 Directional sensitivity of hot film sensors in liquid metals. *Rev. Sci. Instrum* **42**, 1461–1468.

Hof, B., Juel, A. & Mullin, T 2003 Magnetohydrodynamic damping of convective flows in molten gallium. *J. Fluid Mech.* **482**, 163–179.

Hof, B., Juel, A. & Mullin, T 2003 Magnetohydrodynamic damping of oscillations in low -Prandtl-number convection. *J. Fluid Mech.* **545**, 193–201.

Hunt, J. C. & Welty, J. R. 1973 Use of hot film anemometer to measure velocities below 5 cm-sec in mercury. *J. Heat Transfer* **95**, 548–549.

Hurle, D. T. J., Jakeman, E. & Johnson, C. P. 1974 Convective temperature oscillation in molten gallium. *J. Fluid Mech.* **64**, 565–576.

Hussein, E .M. 2003 *Handbook on Radiation Probing, Gauging, Imaging and Analysis: Volume II Applications and Design*. Springer.

Iguchi, M., Demoto, Y., Sugawara, N. & Morita, Z. 1992 Bubble behavior in Hg-air vertical bubbling jets in cylindrical vessel. *ISIJ Intl* **32**, 998–1005.

Iguchi, M., Tsuji, Y., Mizuno, T., Mashiko, T., Sano, M. Kawabata, H., Ito, Y., NakaJima, K. & Morita, Z. 1994 Continuous measurements of bubble characteristics in molten iron bath with Ar gas injection. *ISIJ Intl* **34**, 980–985.

Inoue, Y., Yamashita, S. & Kumada, M. 1999 An experimental study on a wake behind a torus using UVP monitor. *Exp. Fluids* **26**, 197–207.

Jensen, J. A. 1996 *Estimation of Blood Velocities Using Ultrasound: A Signal Processing Approach*. Cambridge.

Juel, A., Mullin, T. Hadid, H. B. & Henry, D. 1999 Magnetohydrodynamic convection in molton gallium. *J. Fluid Mech.* **378**, 97–118.

Kakimoto, K., Eguchi, M., Watanabe, H. & Hibiya, T. 1988 Direct observation by X-ray radiography of convection of molten silicon in the Czochralski growth method. *J. Cryst. Growth* **269**, 630–638.

Kenjereš, S. & Hanjalić, K. 1999 Numerical simulation of magnetic control of heat transfer in thermal convection. *Intl J. Heat Mass Transfer* **25**, 559–568.

Knaepen, B. & Moreau, R. 2008 Magnetohydrodynamic turbulence at low magnetic Reynolds number. *Annu. Rev. Fluid Mech.* **40**, 25-45.

Koster, J. N., Seidel, T. & Dereball, R. 1996 A radioscopic technique to study convective fluid dynamics in opaque liquid metals. *J. Fluid Mech.* **343**, 29–41.

Krautkrämer, J. & Krautkrämer, H. 1990 *Ultrasonic testing of materials*. Springer.

Kubo, N., Ishii, T., Kubota, J. & Ikagawa, T. 2004 Numerical simulation of molten steel flow under a magnetic field with Argon gas bubbling in a continuous casting mold. *ISIJ Intl* **44**, 556–564.

Kubota, M., Akehata, T. & Shirai, T. 1967 The rising velocity and shape of single air bubbles in highly viscous liquids. *Kagaku Kogaku* **31**, 1074–1080.

Kuttruff, H. 1991 *Ultrasonics: Fundamentals and applications*. Elsevier.

Lahjomri, J., Caperan, P. & Alemany, A. 1993 The cylinder wake in a magnetic field aligned with the velocity. *J. Fluid Mech.* **253**, 421–448.

Lantzsch, R., Galindo, V., Grants, I., Zhang, C., Pätzold, O., Gerbeth, G. & Stelter, M. 2007 Experimental and numerical results on the fluid flow driven by a traveling magnetic field. *J. Crystal Growth* **305**, 249–256.

Lavers, J. D., Tallbäck, G. R., Lavers, E. D., Beitelman, L. S. & Curran, C. P. 2006 Flow control in continuous casting mold with dual coil EMS: computational simulation study. *Proceeding of the 5th International Symposium on Electromagnetic Processing of Materials*. ISIJ, Sendai, Japan.

Levich, V. G. 1962 *Physicochemical Hydrodynamics*. Prentice Hall.

Lielausis 1975 Liquid metal magnetohydrodynamics. *Atomic Energy Rev.* **13**, 527–581.

Liger-Belair, G. & Jeandet, P. 2002 Effervescence in a glass of champagne: A bubble story. *Europhys. News* **33**, 1775–1781.

Lindt, L. T. 1972 On the periodic nature of the drag on a rising bubble. *Chem. Engng Sci.* **57**, 1775–1781.

Lohse, D. 2003 Bubble puzzles. *Phys. Today* **56**, 36–41.

Loth, E. 2008 *Computational Fluid Dynamics of Bubbles, Drops and Particles*. Cambridge.

Loth, E. 2008 Quasi-steady shape and drag of deformable bubbles and drops. *Intl J. Multiphase Flow* **34**, 523–546.

Lunde, K. & Perkins, R. J. 1997 Observation on wakes behind spheroidal bubbles and particles. *No.FEDSM97–3530*.

Lykoudis, P. & Dunn, P. F. 1973 Magneto-fluid-mechanic heat transfer from hot film probes. *Intl J. Heat Mass Transfer* **16**, 1439–1442.

Lykoudis, P. 1984 Local measurements in two-phase liquid-metal magneto-fluid-mechanic flow. *J. Fluid Mech.* **147**, 81–104.

Magnaudet, J. & Eames, I. 2000 The motion of high-Reynolds number bubbles in inhomogeneous flows. *Annu. Rev. Fluid Mech.* **32**, 659-708.

Magnaudet, J. & Mougin, G. 2007 Wake instability of a fixed spheroidal bubble. *J. Fluid Mech.* **572**, 311–337.

Malcolm, D. G. 1969 Some aspects of turbulence measurement in liquid mercury using cylindrical quartz-insulated hot-film sensors. *J. Fluid Mech.* **37**, 701–713.

Malcolm, D. G. & Verma, V. 1981 Dynamic response of forced convective heat transfer from hot-film sensors to mercury. Part 2. Experiment. *J. Fluid Mech.* **112**, 475–485.

Marco, P., Grassi, W. & Memoli, G. 2003 Experimental study on rising velocity of nitrogen bubbles in FC-72. *Intl J. Thermal Sci.* **42**, 435–446.

Mathiesen, R.H., Arnberg, L., Bleuet, P. & Somogyi, A. 2006 Crystal fragmentation and columnar-to-equiaxed transitions in Al-Cu studied by synchrotron X-ray video microscopy. *Metall. Mater. Trans. A* **37**, 2515–2524.

Maxworthy, T. 1962 Measurements of drag and wake structure in magneto-fluid dynamic flow about a sphere. *Proceedings of the 1962 heat transfer and fluid mechanics institute, 197–205.*

Maxworthy, T. 1958 Experimental studies in magneto-fluid dynamics: pressure distribution measurements around a sphere. *J. Fluid Mech.* **31**, 801–814.

Maxworthy, T., Gnann, C., Kürten, M. & Durst, F. 1996 Experiments on the rise of air bubbles in clean viscous liquids. *J. Fluid Mech.* **321**, 421–441.

Mazumdar, D. & Guthrie, R. I. L. 1995 The physical and mathematical modelling of gas stirred ladle systems. *ISIJ Intl* **35**, 1–20.

Mazumdar, D. & Evans, J. W. 2004 Macroscopic models fo gas stirred ladles. *ISIJ Intl* **44**, 447–461.

Mei, R., Klausner, J. F. & Lawrence, C. J. 1994 A note on the history force on a spherical bubble at finite Reynolds number *Phys. Fluids* **6**, 418–420.

Mendelson, H. D. 1967 The prediction of bubble terminal velocity from wave theory. *AIChE J.* **13**, 250–253.

Michiyoshi, I., Fanakawa, H., Kuramoto, C. Akita, Y. & Takahashi, O. 1977 Local properties of vertical mercury-argon two-phase flow in a circular tube under transverse magnetic field. *Intl J. Multiphase Flow* **3**, 445–457.

Moffatt, H.K. 1967 On the suppresion of turbulence by a uniform magnetic field. *J. Fluid Mech.* **28**, 571–592.

Moore, D. W. 1963 The boundary layer on a spherical gas bubble. *J. Fluid Mech.* **16**, 161–176.

Moore, D. W. 1965 The velocity of rise of distorted gas bubbles in a liquid of small viscosit*J. Fluid Mech.* **23**, 749–766.

Mordant, N. & Pinton, J. F. 2000 Velocity measurement of a settling sphere. *Eur. Phys. J. B* **18**, 343–352.

Mordant, N., Levque, E. & Pinton, J. F. 2004 Experimental and numerical study of the Lagrangian dynamics of high Reynolds number turbulence. *New J. Phys.* **6**, 116.

Mordant, N., Metz, P., Michel, O. & Pinton, J. F. 2005 An acoustic technique for Lagrangian velocity measurements. *Rev. Sci. Instrum.* **76**, 025105.

Moreau, R. 1990 *Magnetohydrodynamics*. Kluwer.

Moreau, R. 1978 Local and instantaneous measurements measurements in liquid metal MHD. *Proc. Dynamic Flow Conf., 65–79.*

Mori, Y., Hijikata, K. & Kuriyama, K. 1977 Experimental study of bubble motion in mercury with and without a magnetic field. *J. Heat Transfer* **99**, 404–410.

Mössner, R. & Müller 1999 A numerial investigation of three-dimensional magnetoconvection in rectangular cavities. *Intl J. Heat Mass Transfer* **42**, 1111–1121.

Mougin, G. & Magnaudet, J. 2002 Path instability of a rising bubble. *Phys. Rev. Lett.* **567**, 014502.

Mougin, G. & Magnaudet, J. 2006 Wake-induced forces and torques on a zigzag/spiralling bubble. *J. Fluid Mech.* **567**, 185–194.

Mudde, R.F., Groen, J.S. & Van Den Akker, H.E.A. 1998 Application of LDA to bubbly flows. *Nucl. Engng Design* **184**, 329–338.

Mudde, R.F. 2008 Gravity-driven bubbly flows. *Annu. Rev. Fluid Mech.* **37**, 393–423.

Müller, U. & Bühler, L. 2001 *Magnetofluiddynamics in Channels and Containers*. Springer.

Okada, K. & Ozoe, H. 1992 Experimental heat transfer rates of natural convection of molten gallium suppressed under an external magnetic field in either the X, Y, or Z direction. *J. Heat Transfer* **114**, 107–114.

Okaza, K., Toh, T., Fukuda, J., Kawase, T. & Toki, M. 2001 Fluid flow in a continuous casting mold driven by linear induction motors. *ISIJ Intl* **41**, 851-858.

Ozoe, H. & Okada, K. 1989 The effect of the direction of the external magnetic field on the three-dimensional natural convection in a cubical enclosure. *Intl J. Heat Mass Transfer* **32**, 1939–1954.

Perry, A. E. 1982 *Hot-Wire Anemometry*. Oxford University Press.

Preschard, I., Le Gal, P. & Takeda, Y. 1999 On the spatio-temporal structure of cylinder wakes. *Exp. Fluids* **26**, 188–196.

Prosperetti, A. 2004 Bubbles. *Phys. Fluids* **16**, 1852–1865.

Raffel, M., Willert, C. E., Wereley, S. T. & Kompenhaus, J. 2007 *Particle Image Velocimetry: A practical Guide*. Springer-Verlag.

Reed, C. B., Picologlow, B. F., Dauzvardis, P.V. & Bailey, J. L. 1986 Techniques for measurement of velocity in lquid-metal MHD flows. *Fusion Tech.* **10**, 813–821.

Ricou, R. & Vives, C. 1982 Local velocity and mass transfer measurements in molten metals using an incorporated probe. *Intl J. Heat Mass Transfer* **25**, 1579–1588.

Robbert, P. H. 1967 *An Introduction to Magnetohydrodynamics*. Langmans.

Robinson, T. & Larsson, K. 1973 An experimental investigation of a magnetically driven rotating liquid-metal flow. *J. Fluid Mech.* **60**, 641–664.

Saffman, P. G. 1956 On the rise of small air bubbles in water. *J. Fluid Mech.* **1**, 249–275.

Saito, M., Inoue, S. & Fujii, Y. 1978 Gas-liquid slip ratio and MHD pressure drop in two-phse liquid metal flow in strong magnetic field. *J. Nucl. Sci. Technol.* **15**, 476–489.

Saito, M., Nagae, H., Inoue, S. & Fujii, Y. 1978 Redistribution of gaseous phase of liquid metal two-phase flow in a strong magnetic field. *J. Nucl. Sci. Technol.* **15**, 729–735.

Sajben 1965 Hot wire anemometer in liquid mercury. *Rev. Sci. Instrum* **36**, 945–949.

Schwerdtfeger, K. 1968 Velocity of rise of argon bubbles in mercury. *Chem. Engng Sci.* **23**, 937–938.

Serizawa, A., Kataoka, I. & Michiyshi, I. 1975 Turbulence structure of air-water bubbly flow. I. Measuring techniques. *Intl J. Multiphase Flow* **2**, 221–233.

Serizawa, A., Ida, T. & Michiyshi, I. 1990 MHD effect on Nak-nitrogen two-phase flow and heat transfer in a vertical round tube. *Intl J. Multiphase Flow* **16**, 761–788.

Sheng, Y. Y., & Irons, G. A. 1991 A combined Laser Doppler anemometry and electrical probe diagostic for bubble two-phase flow. *Intl J. Multiphase Flow* **17**, 585–598.

Shercliff, J. A. 1962 *The Theory of Electromagnetic Flow Measurement*. Cambridge.

Shercliff, J. A. 1965 *A Textbook of Magnetohydrodynamics*. Pergamon Press.

Shew, W. & Pinton, J. F. 2006 Dynamical model of bubble path instability. *Phys. Rev Lett.* **97**, 144508.

Shew, W., Poncet, S. & Pinton, J. F. 2006 Force measurements on rising bubbles. *J. Fluid Mech.* **569**, 51–60.

Sneyd, A.D. 1993 Theory of electromagnetic stirring by AC fields. *IMA J. Appl. Math.* **5**, 83-113.

Sommeria, J. & Moreau, R. 1982 Why, how, and when, MHD turbulence becomes two-dimensional. *J. Fluid Mech.* **118**, 507–518.

Sreenivasan, B. & Alboussiere, T. 2002 Experimental study of a vortex in magnetic field. *J. Fluid Mech.* **464**, 287–309.

Stefani, F., Gundrum, T. & Gerbeth, G. 200 Contactless inductive flow tomography. *Phys. Rev. E* **70**, 056306.

Suzuki, Y., Nakagawa, M., Aritomi, M., Murakawa, H., Kikura, H. & Mori, M. 2002 Microstructure of the flow field around a bubble in counter-current bubbly flow. *Exp. Thermal Fluid Sci.* **26**, 221–227.

Szekely, J. Chang, C. W. & Ryan, R. E. 1977 The measurement and prediction of the melt velocities in a turbulent, electromagnetically driven recirculating low melting alloy system. *Metall. Trans. B* **8B**, 333–338.

Tagawa, T. & Ozoe, H. 1997 Enhancement of heat transfer rate by application of a static magnetic field during natrual convection of liquid metal in a cube. *J. Heat Transfer* **119**, 265–271.

Tagawa, T. & Ozoe, H. 1998 Enhanced heat transfer rate measured for natural convection in liquid gallium in a cubical enclosure under a static magnetic field. *J. Heat Transfer* **120**, 1027–1032.

Tagawa, T., Authie, G. & Moreau, R. 2002 Buoyant flow in long vertical enclosures in the presence of a strong horizontal magnetic field. Part 1. Fully-established flow. *Euro. J. Mech. B/Fluids* **21**, 383–398.

Takagi, S. & Matsumoto, Y. 1998 Numerical study of the forces acting on a bubble or a particle. *Proc. Intl Conf. Multiphase Flow, 3rd, Lyon, France.* paper 285.

Takatani, K. 2003 Effects of electromagnetic brake and meniscus electromagnetic stirrer on transient molten steel flow at meniscus in a continuous casting mold. *ISIJ Intl* textbf43, 915-922.

Takeda, Y. 1986 Velocity profile measurement by ultrasound Doppler shift method. *Intl J. Heat Fluid Flow* **7**, 313–318.

Takeda, Y. 1987 Measurement of velocity profile of mercury flow by ultrasound Doppler-shift method. *Nucl. Technol.* **79**, 120–124.

Takeda, Y. 1991 Development of an ultrasound velocity profile monitor. *Nucl. Engng Design* **126**, 277–284.

Takeda, Y. 1999 Quasi-periodic state and transition to turbulence in a rotating Couette system. *J. Fluid Mech.* **389**, 81–99.

Takeda, Y. & Kikura, H. 2002 Flow mapping of the mercury flow. *Exp. Fluids* **32**, 161–169.

Taniguchi, S. 2006 *Proceedings of the 5th International Symposium on Electromagnetic Processing of Materials*. Sendai, Japen.

Tavoularis, S. 2005 *Measurements in Fluid Mechanics*. Cambridge.

Thomas, B. G. 2003a Modeling of continuous casting. In *Chapter 5 in Making, Shaping and Treating of Steel* (ed. A. Cramb). Casting Volume, vol. **5**, 5.1–5.24. AISE Steel Foundation, Pittsburgh.

Thomas, B. G. 2003b Fluid flow in mold. In *Chapter 14 in Making, Shaping and Treating of Steel* (ed. A. Cramb). Casting Volume, vol. **5**, 14.1–14.41. AISE Steel Foundation, Pittsburgh.

Toh, T., Hasegawa, H. & Harada, H. 2001 Evaluation of multiphase phenomena in mold pool under in-mold electromagnetic stirring in steel continuous casting. *ISIJ Intl.* **41**, 1245-1251.

Toh, T., Takeuchi, E. & Matsumiya, T. 2006 Recent advances in MHD applications to steelmaking process. *Proceeding of the 5th International Symposium on Electromagnetic Processing of Materials*.

Tomiyama, A., Celata, G. P., Hosokawa, S. & Yoshida, S. 2002 Terminal velocity of single bubbles in surface tension force dominant regime. *Intl J. Multiphase Flow* **28**, 1497–1519.

Touihri, R., Hadid, H. B. & Henry, D. 1999 On the onset of convective instabilities in cylindrical cavities heated from below. II. Effect of a magnetic field. *Phys. Fluids* **11**, 2089–2100.

Trakas, C., Tabeling, P. & Chabrerie, J. P. 1983 Low-velocity calibration of hot-film sensors in mercury. *J. Phys. E: Sci. Instrum* **16**, 568–570.

Tropea, C., Yarin, A. L. & Foss, J. 2007 *Springer Handbook of Experimental Fluid Mechanics*. Springer-Verlag.

Tsinober, A., Kit, E. & Teitel, M. 1987 On the relevance of potential difference method for turbulence measurements. *J. Fluid Mech.* **175**, 199–218.

Tsuge, H. & Hibino, S. I. 1971 The motion of single gas bubbles rising in various liquids. *Kagaku Kogaku* **35**, 65–71.

Tsuge, H. & Hibino, S. I. 1977 The onset conditions of oscillatory motion of single gas bubbles rising in various liquids. *J. Chem. Engng Japan* **10**, 66–68.

Tsuge, H. 1982 The behavior of single bubbles. *Advances in chemical engineering 16: Dynamics of bubbles, drops and dispersions-fundamentals and applications (Soc. Chem. Engng Japan, eds.)* Chap. 1, 1-26.

Veldhuis, C. 2007 *Leonardo's paradox: path and shape instabilities of particles and bubbles.* PhD thesis, University of Twente, Twente.

Veldhuis, C., Biesheuvel, A. & van Wijngaarden, L. 2008 Shape oscillation on bubbles rising in clean and in tap water. *Phys. Fluids* **20**, 040705.

de Vries, A. W. G. 2001 *Path and wake of a rising bubble.* PhD thesis, University of Twente, Twente.

Wang, T., Wang, J., Ren, F. & Jin, Y. 2003 Application of Doppler ultrasound velocimetry in multiphase flow. *Chem. Engng J.* **92**, 111–122.

Weier, T. 1993 *Untersuchungen zum Zylindernachlauf im magnetodydrodynamischen Fall.* Diplomarbeit, Martin-Luther-Universität Halle-Wittenberg, Merseburg.

Wellek, R. M., Agrawal, A. K. & Skelland, A. H. P. 1966 Shapes of liquid drops in liquid media. *AIChE J.* **12**, 854–862.

Willers, G, Eckert, S., Nikrityuk, Petr A., Räbiger, D., Dong, J., Eckert, K. & Gerbeth, G. 2008 Efficient melt stirring using pulse sequences of a rotating magnetic field: II - Application during solidification of Al-Si alloys. *Metall. Mater. Trans. B* **39**, 304–316.

Xu, B., L, B.Q. & Stock, D.E. 2006 An experimental study of thermally induced convection of molten gallium in magnetic fields. *Intl J. Heat Mass Transfer* **49**, 2009–2019.

Yonas, G. 1967 Measurements on drag in a conducting fluid with an aligned field and large interaction number. *J. Fluid Mech.* **30**, 817–823.

Zenit, R. & Magnaudet, J. 2008 Path instability of rising spheroidal air bubbles: A shape-controlled process. *Phys. Fluids* **20**, 061702.

Zenit, R. & Magnaudet, J. 2009 Measurements of the streamwise vorticity in the wake of an oscillating bubble. *Intl J. Multiphase Flow* **35**, 195–203.

Zhang, C., Eckert, S. & Gerbeth, G. 2004 Gas and liquid velocity measurements in bubble chain driven two-phase flow by means of UDV and LDA. *Proc. 5th Intl Conf. Multiphase Flow*, Yokohama, ICMF04-260.

Zhang, C., Eckert, S. & Gerbeth, G. 2005 Experimental study of single bubble motion in a liquid metal column exposed to a DC magnetic field. *Intl J. Multiphase Flow* **31**, 824–842.

Zhang, C., Eckert, S. & Gerbeth, G. 2007 The flow structure of a bubble-driven liquid-metal jet in a horizontal magnetic field. *J. Fluid Mech.* **575**, 57–82.

Zhang, C., Eckert, S. & Gerbeth, G. 2007 Modification of bubble driven liquid metal flows under the influence of a DC magnetic field. *ISIJ Intl* **47**, 795–801.

Zhilin, V. G., Zvyagin, K. V., Ivochkin, A. A. & Oksman, A. A. 1989 Diagnostics of liquid metal flows using fibre-optic velocity sensor. *Liquid Metal Magnetohydrodynamics, Lielpeteris and Moreau (eds)* Kluwer Academic Publishers, 373–379.

Zun, I. & Groselj, J. 1996 The structure of bubble non-equilibrium movement in free-rise and agitated-rise conditions. *Nucl. Engng Design* **163**, 99–115.